arXiv:0704.3535v2 [quant-ph] 7 May 2007

LUDWIG-MAXIMILIANS-UNIVERSITÄT MÜNCHEN
MAX-PLANCK-INSTITUT FÜR QUANTENOPTIK GARCHING

Quantum Simulations in Ion Traps

Towards Simulating the Early Expanding Universe

Diploma thesis

by Lutz Petersen

December 2006

Abstract

This thesis provides an overview of an approach to quantum simulations using magnesium-25 ions stored in a linear Paul trap as the carriers of quantum information. Their quantum state is manipulated and read out using ultraviolet laser beams. Several important steps towards realising the first experiments have been undertaken, the most striking of which is cooling the ions to their motional ground state. We describe a first experiment simulating cosmological particle creation in the Early Universe and discuss the expected results.

Acknowledgements

I would like to thank all the people that have, in one way or the other, contributed to this thesis. First and foremost, I have to mention my dear colleagues Axel, Günther, Hector, and Steffen who did a great job not only in the laboratory but also by always making me feel in good hands. Special thanks goes to my advisor Tobi for the great support and perpetual encouragement, for the discussions about the freewill and for the numerous weird stories about dogs and the like. Thanks also to the quasi-group member and technician Arnold Steyer who time and again impressed not only me with his approach to everyday life.

A big "thank you" to Ralf Schützhold who developed the proposal for this thesis. We greatly profited from his collaboration and acknowledge that he never sniffed at the 101 questions of an experimentalist.

I gratefully acknowledge Paul Pham, his support and assistance in making the electronics do what it is supposed to do. Thanks to Markus Wewer of LOT Oriel and Axel Lucas of B. Halle for the good collaboration. Many more people have helped us in the lab, especially all the amiable colleagues at MPQ who tried to satisfy even the most exceptional desires. Although they are too numerous to be listed here in completion, I'd like to mention Helmut Brückner and Tom Wiesmeier for their excellent electronics support, Thomas Strobl and his crew for their commitment to providing the best manufacturing of required laboratory items, and Thomas Rieger as one representative of the Rempe group helping us out with laboratory equipment whenever necessary.

Finally, I'd like to thank my parents for their support and affection at all times. And last but not least thanks to my boyfriend Bastian for reminding me that there is a life besides doing physics in the lab.

Contents

I. Theoretical considerations 1

1. Optical properties of a two-level system 3
   1.1. Optical Bloch equations . . . 3
   1.2. Saturation effects . . . 5

2. Magnesium-25 as a qubit system 11
   2.1. Electronic structure of magnesium-25 . . . 11
   2.2. Motional states . . . 12
   2.3. Qubit state initialisation and detection . . . 13
   2.4. Qubit state manipulation . . . 15
   2.5. Coupling qubit and motional states . . . 18
   2.6. Cooling the ions' motion . . . 20

II. Assembly of the experimental apparatus 25

3. Trap apparatus 27
   3.1. Linear Paul trap . . . 27
   3.2. Vacuum chamber . . . 34
   3.3. Ion source . . . 35
   3.4. Magnetic field . . . 39

4. Laser apparatus 45
   4.1. Laser sources . . . 45
   4.2. Second harmonic generation . . . 47
   4.3. Beamlines . . . 49
   4.4. Doppler-free iodine spectroscopy . . . 56

5. Visualisation and data acquisition 63
5.1. Optics . . . 63
5.2. PMT . . . 66
5.3. CCD camera . . . 68
5.4. Auge software . . . 72

6. Experimental control 77
6.1. AOM control . . . 77
6.2. Paul box . . . 78
6.3. Jäger box . . . 82
6.4. Interplay . . . 82

III. Experimental issues 85

7. Simulating the Early Expanding Universe 87
7.1. Theoretical considerations . . . 87
7.2. Experimental implementation . . . 89

8. Compensation of micromotion 93
8.1. Theoretical background . . . 93
8.2. Methods for compensation of micromotion . . . 96
8.3. Experimental results . . . 102

9. Experiments on coherent transitions 105
9.1. Common steps of a flopping experiment . . . 106
9.2. “Hot” flopping using co-propagating Raman beams . . . 107
9.3. “Hot” flopping using perpendicular Raman beams . . . 111
9.4. Shelving . . . 114
9.5. Cooling to the motional ground state . . . 115

A. Auge visualisation and data acquisition software 121

B. Auge Transfer Protocol (ATP) 125

C. Paulbox C compiler 131

Introduction

The idea of quantum simulations was first formulated by Richard Feynman [1]. He recognised that a calculation to predict the behaviour of quantum systems can only be performed by utilising another quantum system. That way, quantum mechanical properties like superposition states or entanglement are inherently included in the simulation system.

One might be tempted to think that a state-of-the-art classical computer would be able to calculate the time evolution of a complex quantum system. A simple estimation elucidates that this is not the case even for comparably small quantum systems: The state of a system of multiple—not necessarily interacting—particles is described by the coefficients of the respective product Hilbert space. For $n = 200$ two-level particles there are $2^n = 1.61 \cdot 10^{60}$ coefficients, a number that corresponds to the estimated amount of *all protons in the universe*. Too many parameters for any classical computer even in the future.

The proposed quantum computer addresses this problem by consisting itself of interacting qubits. 200 qubits will suffice to describe the state of 200 two-level particles. With a universal set of quantum manipulation operations it can in principle cope with many unsolved quantum problem, e. g. the challenge of a prime factor in polynomial time [2] that would render most classical encryption algorithms vulnerable [3]. However, to realise a universal quantum computer, an appreciable amount of around 1000 logical qubits is required, each logical qubit requiring an overhead of about 100 ancilla qubits to allow for fault-tolerant operation [4]. Although controlling and manipulating 10^5 qubits with sufficient fidelities appears to be technically feasible [4], even the most optimistic estimations for the realisation of a universal quantum computer are of the order of 10 – 20 years.

In our group, we try to implement a "shortcut" on the way towards a quantum computer via the approach of quantum simulations in ion traps, which follows Feynman's original proposal even closer. Take a quantum system (denoted A) whose initial conditions and interaction terms, i. e. its Hamiltonian, can be manipulated in a controlled way. If this Hamiltonian matches the one of another system of interest (denoted B), the time evolution as well as all properties observed and deduced at system A can be analogously transferred to system B. This is why we call system A an *analogous quantum simulator*. It opens the possibilities to simulate specific systems beyond the scope of classical computation. Examples include quantum spin systems such as high-T_C superconductors whose physics is still far from being understood [5]. The simulations may also help to better understand effects such as quantum relativistic and gravitational issues [6, 7, 8].

Another motivation for the realisation of a quantum simulator is to actually "observe" phenomena in experiment that have so far only been predicted by quantum theory. The first experiment to be implemented in our quantum simulator addresses the particle creation process in the Early Universe according to a proposal by Schützhold et al. [9] in collaboration with our group: Matter as we observe it nowadays shows aggregations (planets, stars, galaxies) rather than being distributed evenly over space. According to the standard model of cosmology the seeds for the required structure formation are provided by quantum fluctuations during the very early moments of the universe. One possible process is cosmological particle creation during a non-adiabatic expansion of space-time [10]. We can identify the expansion of space-time with a non-adiabatic change of the ions' trapping potential in our laboratory. This will "create" pairs of phononic excitations corresponding to particle pairs in the universe, see for example [11, 12, 13]. Thus, the system to be simulated is the universe itself (!), whereas even a single ion can serve as a simulation system allowing for the investigation of some of the most interesting properties.

Various systems can be exploited in terms of quantum simulators; examples include neutral atoms, molecules, quantum dots and many more [4]. In our laboratory, we implement a technique first proposed by Cirac and Zoller [14]: Laser-cooled ions stored in a linear Paul trap under ultra-high vacuum serve as the carriers of quantum information. By shining onto the ions with laser beams we can initialise, manipulate, and determine their internal electronic quantum state in a controlled way and with high fidelities. In addition, the ions may conditionally interact among each other by coupling their electronic state to a collective vibrational mode of motion in the trap. As coupling to the environment is very weak for such system, observed coherence times are long compared to the duration of the required operations [15].

We use two distinct hyperfine states of magnesium-25 ions to implement a qubit where the coupling between the two levels is provided via a two-photon stimulated

Raman transition. Readout occurs by fluorescently scattering photons in a *cycling transition* allowing for high-accuracy state-sensitive detection by means of a photomultiplier or a CCD camera. The NIST group in Boulder, Colorado, are currently implementing a similar system and we are grateful to profit from their former experience with beryllium-9 ions.

Several important steps towards our first experiment have been realised during a year's work on this thesis. As the initial theoretical proposal [11] posed severe problems to an experimental realisation, we started a collaboration with the quantum theory group of Ralf Schützhold* at the Technical University of Dresden. For the author it was most interesting to contribute to a theoretical proposal and to develop an experimental technique for its realisation [9]. Progress achieved with the apparatus in the laboratory includes the ability to trap ions, to drive coherent transitions between their internal electronic states (Rabi flopping), to couple their electronic state to vibrational modes, to measure their vibrational state, and to efficiently initialise their quantum state by cooling them close to the vibrational ground-state.

The group had to develop strong laser sources [16] at ultraviolet wavelengths to access the transitions of magnesium-25 ions. They are stored within a specially designed trapping apparatus driven at parameters that have not been well investigated before. Starting from the successful loading of the first ion, a lot of work has been spent on the assembly and optimisation of the related laboratory components and their operation. Let me focus on my significant contributions: Theoretical considerations on disturbing micromotion of ions in the trap as well as their experimental realisation (chapter 8) allowed for a better understanding of the trap apparatus, whose parameters lie in an intermediate regime between the resolved-sideband and the non-resolved-sideband case (natural linewidth of the observed transition is comparable to the trapping frequency). Compensation of micromotion turned out to be particularly important for a change of the trapping potential by more than one order of magnitude needed to realise [9]. Further activities concerning the trap included the design and fabrication of magnetic field coils intended for providing a quantisation axis and required highly stable Zeeman shifts of the involved qubit levels (section 3.4). External magnetic field noise has to be minimised using an active compensation system, which was home-built and tested. As for the laser apparatus, works included the modification and optimisation of Doppler-free saturation spectroscopy units (section 4.4) as well as the setup and optimisation of the laser beamline (infrared, visible, and ultraviolet wavelengths) including 15 single- and double-pass acousto-optical modulators (section 4.3). Electronics for locking our laser systems to an iodine signal were developed and thoroughly tested for maximum reliability. The system containing our single photon detection instruments (photomultiplier and CCD camera) had to be optimised for maximum sensitiveness thus improving the signal-to-noise ratio by up to two orders of magnitude (chapter 5). Tedious debugging and resoldering sessions allowed to eventually put our home-built experimental control system into operation. Digital electronics with a programmable processor clocked at 100 MHz renders this system a real-time tool controlling all the laser operation cycles during the proposed and future quantum simulation experiments (section 6.2).

---

*schuetz@theory.phy.tu-dresden.de

Apart from the hands-on activities appreciable amount of time has been dedicated to software development, debugging, and documentation, which should keep the system adaptable to new requirements. Greater software projects encompassed the development of a compiler for fast control of our experimental control system, the development of visualisation and data acquisition software for our CCD camera (section 5.4), and a respective network protocol for communication with our experimentation software system.

This thesis is divided into three parts: The first part gives an overview of the theoretical models used within the field of quantum simulations. We will discuss the two-level system as a description of qubit dynamics and fluorescence phenomena (chapter 1) and review our implementation of quantum simulations using magnesium-25 ions (chapter 2). The second part contains a tour through our lab where we introduce the ion trap apparatus (chapter 3), the laser apparatus (chapter 4) as well as our detection / data acquisition (chapter 5) and experimental control systems (chapter 6). In the third part we present experimental data. Among the results are: a proposal of the implementation and measurement of [9] (chapter 7), a review of methods for the compensation of micromotion from an experimentalists' view (chapter 8), and the worldwide first data on coherent interactions using $^{25}\mathrm{Mg}^{+}$ ions like Rabi flopping and ground-state cooling experiments (chapter 9).

Part I.

Theoretical considerations

1. Optical properties of a two-level system

In the context of quantum simulations we will be dealing with couplings between electronic states that can be described by the model of an effective two-level system. In particular, the two phenomena of resonance fluorescence and Rabi oscillations can be understood using the same set of equations.

We will denote the lower state with $|a\rangle$ and the upper state with $|b\rangle$. We further assume the following conditions:

1. The two states are separated by an energy difference of $\hbar\omega_0$.
2. The system interacts with an externally applied classical electromagnetic field $E(t) = E_0 \cos(\omega t + \delta)$.
3. The population in the upper state has a limited lifetime τ and can decay into the lower state by spontaneous emission characterised by the natural linewidth $\Gamma = 1/\tau$.

1.1. Optical Bloch equations

The time evolution of the two-level system is described by the time evolution of its density matrix $\hat{\rho}$—or more precisely: by the time evolution of the four density matrix elements ρ_{ij}, where i and j encode either state $|a\rangle$ or state $|b\rangle$. These equations are known as the *optical Bloch equations* (see for example [17, 18]):

$$\begin{aligned}
\dot{\rho}_{bb} &= -\frac{i\Omega}{2}\left(\rho_{ab}e^{i\Delta t} - \text{c. c.}\right) - \Gamma\rho_{bb}, \\
\dot{\rho}_{ab} &= \frac{i\Omega}{2}e^{-i\Delta t}\left(1 - 2\rho_{bb}\right) + (i\Delta - \frac{\Gamma}{2})\rho_{ab}, \\
\dot{\rho}_{ba} &= \dot{\rho}^{*}_{ab}, \\
\dot{\rho}_{aa} &= -\dot{\rho}_{bb},
\end{aligned} \tag{1.1}$$

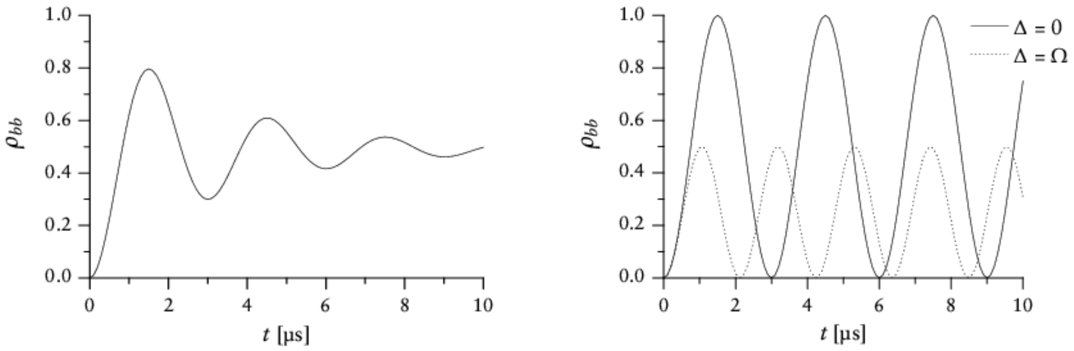

(a) $\Gamma = \Omega/5$ (b) $\Gamma = 0$

Figure 1.1.: Example Rabi flopping curves of the upper state population ρ_{bb} for $\Omega = 2\pi/3\,\mathrm{MHz}$ and different parameters for the decay rates Γ. Unless noted otherwise, a detuning of $\Delta = 0$ has been chosen.

where

$$\Omega = \frac{|\langle a|\hat{x}|b\rangle|\, E_0}{\hbar} \tag{1.2}$$

is the Rabi frequency and

$$\Delta = \omega_0 - \omega \tag{1.3}$$

is the detuning of the radiation field frequency ω with respect to the system's transition frequency ω_0. In principle, we can distinguish between two different parameter regions:

1. *Strong coupling* where the lifetime of the upper state is much larger than the typical duration of a Rabi oscillation period, $\Gamma \ll \Omega$, and
2. *Weak field limit* where the upper state decays much faster compared to the Rabi frequency, $\Gamma \gg \Omega$.

1.1.1. Rabi oscillations

In the Rabi oscillation region the upper state is long-lived enough for Rabi oscillations to occur: The radiation field will transfer the population from $|a\rangle$ to $|b\rangle$ and vice versa. Because of the limited lifetime of the upper state we will observe a damped oscillation, see fig. 1.1a. The equilibrium population is close to 1/2, which is due to the saturation of the transition, see section 1.2.1 below.

In the case that decay of the upper state can be neglected, the optical Bloch equations (1.1) give a perfect sinusoidal oscillation, see fig. 1.1b. Both the oscillation frequency and the oscillation amplitude depend on the detuning Δ; the former which we will call the effective Rabi frequency is given by

$$\Omega_{\text{eff}} = \sqrt{\Omega^2 + \Delta^2}, \tag{1.4}$$

whereas the peak-to-peak amplitude $\rho_{bb,0}$ of the oscillation is determined by the ratio

$$\rho_{bb,0} = \frac{\Omega^2}{\Omega_{\text{eff}}^2}. \tag{1.5}$$

The duration $\tau_\pi = \pi/\Omega$ it takes to transfer all the population from one state to the other is called the π flopping duration. The reason for this naming is clear: During the π flopping duration the phase of a Rabi oscillation is shifted by π. Analogously, a π pulse is an electric field pulse that has the length of the π flopping duration. Another important pulse duration is the $\pi/2$ flopping duration. Starting from an eigenstate, i. e. $|a\rangle$ or $|b\rangle$, it distributes the probabilities like evenly among the two states.

1.1.2. Weak field limit

The weak field limit is characterised by a very small Rabi frequency compared to the linewidth of the transition. As such a small Rabi frequency is determined by a weak incident electric field, we call this region the weak field limit. Here, the population of the upper state reaches its equilibrium before any significant Rabi oscillations can occur, see fig. 1.2. Resonance fluorescence phenomena can often be described in the weak field limit.

1.2. Saturation effects

1.2.1. Power broadening

For intense incoming radiation fields, the effective linewidth of the system's transition broadens, i. e. resolution of the transition decreases with larger field intensities. To understand this, we have a closer look at the steady-state solution of the optical Bloch equations (1.1). We can deduce the population in the upper state $|b\rangle$ after Rabi oscillations have damped out:

$$\rho_{bb}(t \to \infty) = \frac{\Omega^2}{4} \frac{1}{\Delta^2 + (\Gamma/2)^2 + \Omega^2/2}. \tag{1.6}$$

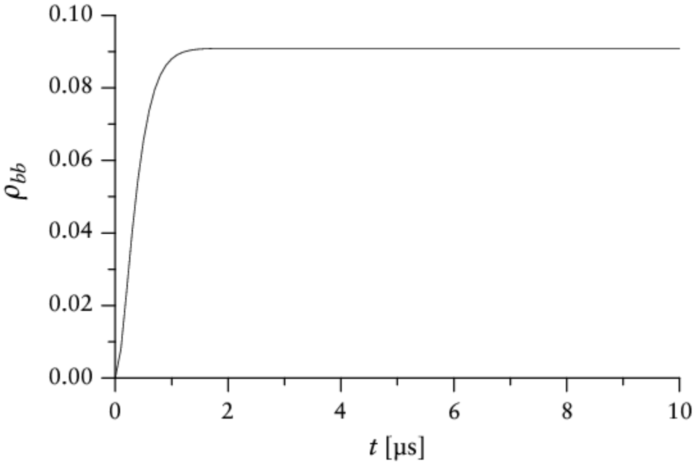

Figure 1.2.: Development of the upper-state population ρ_{bb} over time for $\Omega = 2\pi/3\,\mathrm{MHz}$, $\Gamma = 3\Omega$, and $\Delta = 0$.

Thus, the upper state population $\rho_{bb}(\infty)$ is Lorentzian-shaped in dependence of the detuning Δ. The effective linewidth of this distribution is given by

$$\Gamma_{\mathrm{eff}} = \sqrt{\Gamma^2 + 2\Omega^2}. \tag{1.7}$$

We see that the effective linewidth increases as the Rabi frequency Ω increases. As the Rabi frequency is proportional to the electric field amplitude E_0, eq. (1.2), we observe an increasing full width at half maximum (FWHM) with increasing field intensities $I = \epsilon c E_0^2$ (where ϵ characterises the absolute permittivity of the optical medium).

In order to better characterise the power broadening effect we introduce the saturation intensity I_{sat}. It is defined as the intensity of a resonant incident electromagnetic field causing the steady-state upper state population (1.6) to reach the value of 1/4, i. e.

$$\Omega^2 = \frac{\Gamma^2}{2}, \tag{1.8}$$

which can also be written as [19]

$$I_{\mathrm{sat}} = \frac{\hbar \Gamma \omega_0^3}{12\pi c^2}. \tag{1.9}$$

In the limit of infinite intensities the upper-state population ρ_{bb} takes the value of 1/2. This result is independent of Γ or Δ.

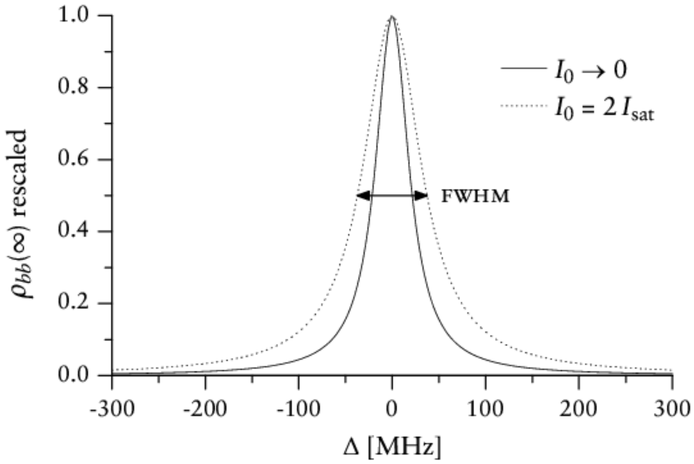

Figure 1.3.: Steady-state upper-state population ρ_{bb} as a function of the detuning Δ. The transition lines have been rescaled to 1.0 at their respective maximum for better comparability.

As an example, we investigate a fluorescent transition with a natural linewidth of $\Gamma = 2\pi \cdot 43\,\mathrm{MHz}$ and plot ρ_{bb} in dependence of Δ, fig. 1.3. The linewidth, i. e. the FWHM, broadens to $\Gamma' = 74.5\,\mathrm{MHz}$ as the incident intensity is increased from virtual zero to twice the saturation intensity.

1.2.2. Attenuation

The effect of attenuation of a laser beam in a saturated optical medium plays an important role in e. g. saturation spectroscopy. To understand the relevant processes consider the very simple model of a two-level system with its associated Einstein equations [17]

$$\begin{aligned} \frac{\mathrm{d}N_1}{\mathrm{d}t} &= AN_2 - B\rho N_1 + B\rho N_2, \\ \frac{\mathrm{d}N_2}{\mathrm{d}t} &= -\frac{\mathrm{d}N_1}{\mathrm{d}t}, \end{aligned} \tag{1.10}$$

where N_1 and N_2 denote the population in the lower and upper levels respectively, A and B are the Einstein coefficients related to spontaneous emission and absorption / stimulated emission, and ρ is the average energy density of the radiation field.

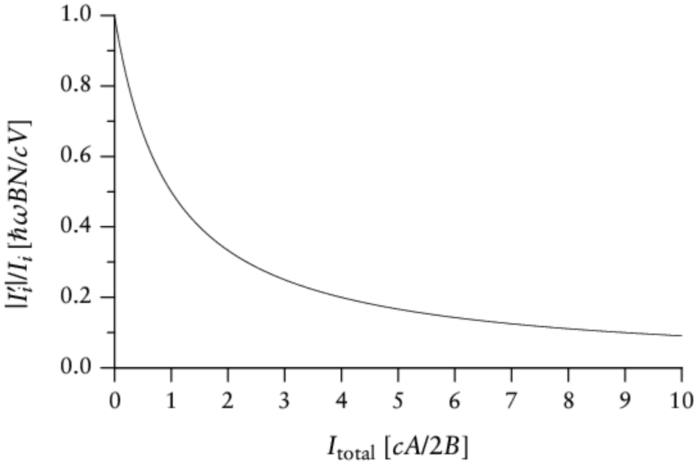

Figure 1.4.: Relative optical attenuation $|\mathrm{d}I_i/\mathrm{d}z|/I_i$ of a beam travelling through a region with overall intensity I_total.

In the steady state, neither N_1 nor N_2 change, that is

$$N_2 = N\frac{1}{2+\frac{A}{B\rho}}. \tag{1.11}$$

We can estimate the optical attenuation, i. e. the change in energy density ρ over time or, equivalently, the change in intensity I over the propagation distance z. It is proportional to the number of photons absorbed minus the number of photons emitted by stimulated emission:

$$\begin{aligned} \frac{\mathrm{d}I}{\mathrm{d}z} &= -\frac{\hbar\omega}{cV}\left(BIN_1 - BIN_2\right) \\ &= -\frac{\hbar\omega BIN}{cV}\left(1-\frac{2BI}{cA+2BI}\right) \end{aligned} \tag{1.12}$$

where V denotes some normalisation volume, c is the speed of light and the last equality has been derived using eq. (1.11).

We may also derive an expression for the optical attenuation in the case where there are several optical sources, i. e. overall intensity is equal to the sum of the individual intensities. As the underlying process of optical attenuation is a single particle process (absorption and emission of photons), attenuation will be proportional to the respective intensity

$$\frac{\mathrm{d}I_i}{\mathrm{d}z} = \frac{\mathrm{d}I}{\mathrm{d}z} \cdot \frac{I_i}{I}, \tag{1.13}$$

which means that the relative optical attenuation is the same for each contributing source:

$$\frac{\mathrm{d}I_i/\mathrm{d}z}{I_i} = -\frac{\hbar\omega BN}{cV}\left(1 - \frac{2BI_{\text{total}}}{cA + 2BI_{\text{total}}}\right). \tag{1.14}$$

Fig. 1.4 illustrates the meaning of eq. (1.14): The relative optical attenuation decreases when overall intensity is increased, that is when the transition becomes more and more saturated. In the limit of infinite overall intensities, the system does not attenuate at all—it becomes transparent, which is also known as optical bleaching.

2. Magnesium-25 as a qubit system

2.1. Electronic structure of magnesium-25

We use trapped magnesium-25 ions ($^{25}\mathrm{Mg}^+$) as the carriers of quantum information. These ions have one valence electron which can populate distinct energy levels, see fig. 2.1. The nuclear spin of $I = 5/2$ is responsible for energy splittings due to the hyperfine interaction: For a total electronic spin of $J = 1/2$ there are two hyperfine sublevels $F \in 2, 3$, fine structure levels with $J = 3/2$ split into four sublevels $F \in 1, 2, 3, 4$.

The two hyperfine levels of the $3S_{1/2}$ manifold are used to store quantum information in a qubit where the lower qubit state is $|{\downarrow}\rangle = 3S_{1/2}\,|F = 3, m_F = 3\rangle$ and the upper state is $|{\uparrow}\rangle = 3S_{1/2}\,|F = 2, m_F = 2\rangle$. Any manipulation or state discrimination occurs by laser interaction that couples these qubit levels to states of the P manifold.

The $3S_{1/2} \leftrightarrow 3P_{3/2}$ transition lies at 279.635 nm whereas the $3S_{1/2} \leftrightarrow 3P_{1/2}$ transition, separated from the former by the fine structure splitting of $2\pi \cdot 2.746\,\mathrm{THz}$, lies at 280.353 nm. Both transitions are dipole-allowed and have radiative linewidths of $2\pi \cdot 43\,\mathrm{MHz}$ each. In contrast, transitions between hyperfine states of the $3S_{1/2}$ manifold are not dipole-allowed. Moreover, these states are separated by a hyperfine splitting of merely 1.789 GHz, which is why direct radiative decay processes can be neglected throughout.

Degeneracy of the hyperfine levels of the same F manifold is broken by applying a magnetic quantisation field B leading to Zeeman energy shifts between different m_F levels

$$\Delta E = g_F m_F \mu_B B \tag{2.1}$$

where g_F is the Landé factor and μ_B is the Bohr magneton. The Zeeman splitting of the $3S_{1/2}$ hyperfine levels is of particular importance for quantum simulation experiments as these hyperfine levels will be used to store quantum information in a qubit. Their Landé factors are $-1/3$ and $1/3$ respectively [20]. We would usually apply a magnetic

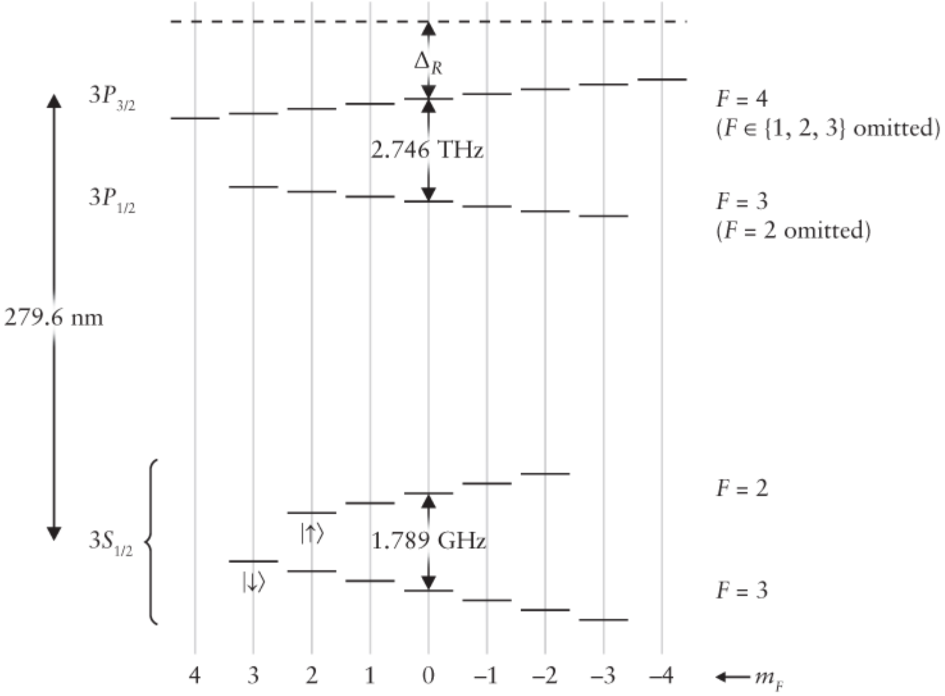

Figure 2.1.: Energy levels of $^{25}\mathrm{Mg}^{+}$ (not to scale). Note that we have omitted hyperfine levels of the P manifold which are not relevant to our quantum simulation experiments. $|{\downarrow}\rangle$ and $|{\uparrow}\rangle$ denote the two states of our qubit system, Δ_R is the detuning of the virtual Raman level with respect to the $3P_{3/2}$ level.

field of about $B = 5.6\,\mathrm{G} = 560\,\mu\mathrm{T}$ introducing energy splittings of $\Delta E/\hbar = m_F \cdot 2\pi \cdot 2.6\,\mathrm{MHz}$.

2.2. Motional states

In our setup the magnesium ions are confined in a three-dimensional harmonic potential using a combination of AC and DC electric fields, see chapter 3. The motion of a single ion in the storage potential can be described by the model of the quantum mechanical oscillator. It is characterised by equidistant energy levels separated by $\hbar\omega$ where ω is the resonance frequency of the potential. We will denote its energy eigenstates—the Fock states—by numbers ranging from zero to infinity. Throughout this thesis, we will characterise the state of an ion by its qubit (electronic) state (which is a linear combination of $|{\downarrow}\rangle$ and $|{\uparrow}\rangle$) as well as by its motional state (which is a linear combination of $|0\rangle$, $|1\rangle$, $|2\rangle$, etc.).

2.3. Qubit state initialisation and detection

All our quantum simulation experiments begin by optically pumping the electronic population into the $|{\downarrow}\rangle$ state. This is achieved by shining onto an ion with two near-resonant laser beams, the Blue Doppler (BD) laser driving a closed cycling transition $3S_{1/2}\,|F=3\rangle \leftrightarrow 3P_{3/2}\,|F=4\rangle$ and the Red Doppler laser tuned to the $3S_{1/2}\,|F=2\rangle \leftrightarrow 3P_{1/2}\,|F=3\rangle$ transition. (The names of the two laser beams are due to the fact that they can be used to Doppler cool [21] the ions, see below.) Both laser beams are polarised σ^+ with respect to the magnetic quantisation field. They thus transfer electronic population to one of the $3P$ states illustrated in fig. 2.1 increasing the m_F value at the same time. Subsequently, the population will decay into one of the lower states by resonance fluorescence where the probability of decay into $3S_{1/2}\,|F=3\rangle$ is about

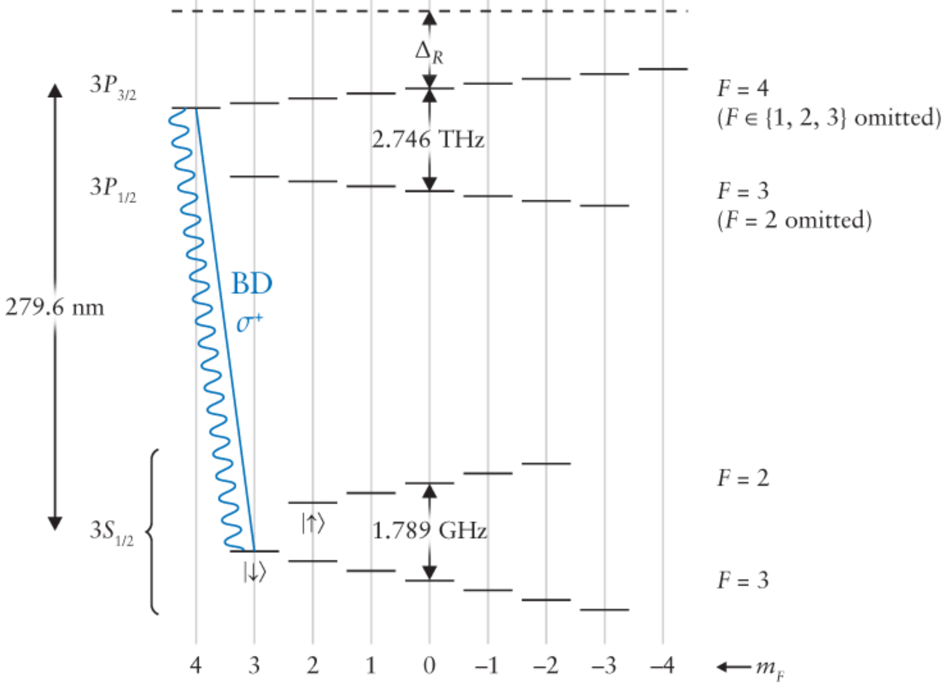

Figure 2.2.: Cycling resonance fluorescence transition used to detect electronic population in the $|{\downarrow}\rangle$ state of our qubit system (lengths not to scale).

transition frequency $\omega_{0,\mathrm{BD}}$	$2\pi \cdot 1.0720841(12) \cdot 10^{15}\,\mathrm{Hz}$
natural transition linewidth Γ	$2\pi \cdot 43\,\mathrm{MHz}$
saturation intensity I_{sat}	$250\,\mathrm{mW} \cdot \mathrm{cm}^{-2}$

Table 2.1.: BD cycling transition properties.

twice as high as the probability of decay into $3S_{1/2}\,|F=2\rangle$. During resonance fluorescence m_F may change according to the dipole rule $\Delta m_F = 0, \pm 1$. This way, all electronic population is eventually pumped into the $|{\downarrow}\rangle$ state.

In order to discriminate ions in the $|{\downarrow}\rangle$ state from ions in the $|{\uparrow}\rangle$ state we use the transition $|{\downarrow}\rangle \leftrightarrow 3P_{3/2}\,|F=4, m_F=4\rangle$, see fig. 2.2. The alert reader will have noticed that this transition is driven by the BD laser. After electronic population has been shifted from $|{\downarrow}\rangle$ to $3P_{3/2}\,|F=4, m_F=4\rangle$ it can only decay back into $|{\downarrow}\rangle$ (due to dipole rules) at the same time emitting resonance fluorescent light. The BD transition can thus be excited over and over again, scattering many photons if the ion is actually in the $|{\downarrow}\rangle$ state. This is called a *cycling transition*. Its properties are listed in tab. 2.1. In contrast, if the ion is in the $|{\uparrow}\rangle$ state, the BD laser cannot drive a resonant transition to the $3P_{3/2}$ level. Off-resonant excitation is however possible (although improbable: the transition linewidth of 43 MHz makes up for only 2.4% of the hyperfine splitting between $|{\downarrow}\rangle$ and $|{\uparrow}\rangle$) and effectively limits the detection time: Once an off-resonant excitation has occurred, there is a finite probability of decay into $|{\downarrow}\rangle$ thereby entering the cycling transition. Thus even an initially dark ion will eventually fluoresce. In practice, we use detection durations of 20 µs – 50 µs to minimise the influence of these effects (causing a loss of contrast).

Using the optical Bloch equations (1.1) and the parameters listed in tab. 2.1 we may calculate the population in the upper $3P_{3/2}\,|F=4, m_F=4\rangle$ state for a system initially in the ground state $|{\downarrow}\rangle$. As we can see from fig. 2.3 the weak field limit is a very good approximation to our situation. With a steady-state upper state population of 0.125 we expect a fluorescence signal of $0.125 \cdot 2\pi\Gamma = 2\pi \cdot 34\,\mathrm{MHz}$, i. e. $3.4 \cdot 10^7$ scattered photons per second.

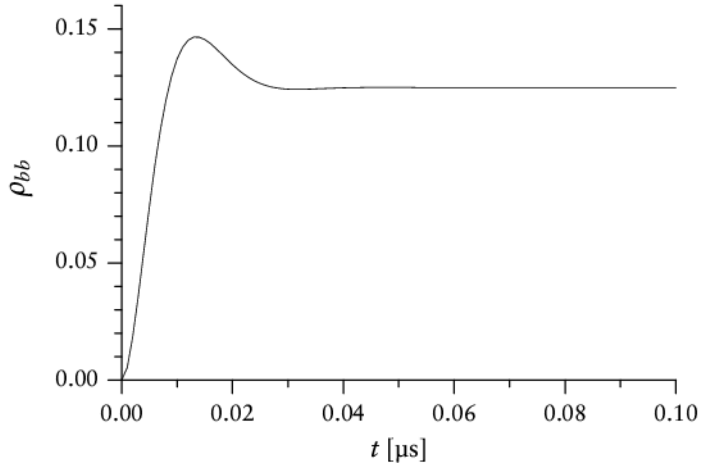

Figure 2.3.: Population in the detection state $3P_{3/2}\,|F=4, m_F=4\rangle$ for the BD fluorescent detection transition in magnesium (not to scale). Typical experimentation values were used for this plot—intensity is $I=(2/3)I_{\text{sat}}=167\,\text{mW}\cdot\text{cm}^{-2}$ and the laser is red-detuned with respect to the resonance frequency by $\Gamma/2=2\pi\cdot 21.5\,\text{MHz}$.

2.4. Qubit state manipulation

2.4.1. Two-photon stimulated Raman transitions

In magnesium-25, the two qubit levels are energetically separated by $\hbar\cdot 2\pi\cdot 1789\,\text{MHz}$, lying in the radio frequency (RF) range. In order to transfer electronic population between the two qubit levels, we use a two-photon stimulated Raman transition: Two laser beams shining onto an ion at the same time drive the transition from $|\downarrow\rangle$ to $|\uparrow\rangle$ and vice versa via a shared virtual Raman level $|\text{ram}\rangle$, which is blue-detuned with respect to the $P_{3/2}$ level by $\Delta_R=$ several tens of GHz, see fig. 2.4. In a simple picture we may consider the two-photon stimulated Raman process as the absorption of a photon from one beam followed by a stimulated emission into the other. During the two-photon stimulated Raman process we alter the m_F value by one, yet shine onto the ion with two lasers. Therefore only one of the lasers is polarised σ^+ while the other must be polarised π with respect to the magnetic quantisation field axis.

The scheme of two-photon stimulated Raman transitions has several advantages compared to driving the transition directly:

- The Rabi frequency can be adjusted by altering the intensity of the two Raman lasers as well as by detuning the virtual Raman level, see below.

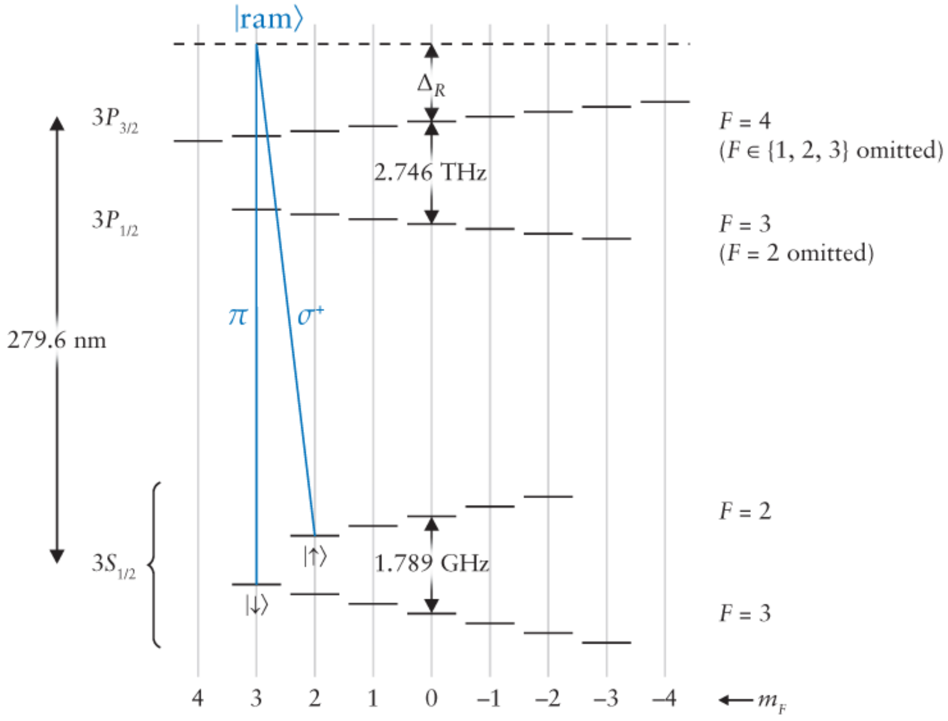

Figure 2.4.: Two-photon stimulated Raman transition used to transfer electronic population between the $|\downarrow\rangle$ and $|\uparrow\rangle$ states (lengths not to scale). Note that one of the Raman beams has to be polarised σ^+ while the other has to be polarised π with respect to the magnetic quantisation field axis.

- The frequency difference between the two lasers, i. e. the actual driving frequency, as well as their relative phase, can be adjusted in a very accurate manner ($\Delta\omega \approx 2\pi \cdot 1\,\mathrm{Hz}$) using acousto-optic modulators in one or both of the laser beams.
- Small drifts of the Raman laser frequencies do not affect the strength of the driven transition as their difference frequency remains unchanged.
- Although the effective driving frequency is in the RF range, the ion still experiences the strong electric field gradients imposed by the UV laser fields. These field gradients are necessary to couple the electronic and motional states of the ion, see section 2.5.

In reality, the two Raman beams will of course couple to all the states of the $3P$ manifold. These states may noncoherently decay into $3S$ by spontaneous emission, which is a disadvantage of the two-photon stimulated Raman scheme. The probability for spontaneous emission may however be significantly reduced by choosing a large detuning Δ_R. In return, we need correspondingly large laser intensities of the order of $10^5\,\mathrm{mW}\cdot\mathrm{cm}^{-2}$ for the Raman beams. We use fibre lasers to provide these powers, see chapter 4.

The coupling of both Raman lasers to the $3P$ manifold can be adiabatically eliminated [22, 15, 23, 24] and we may describe the coupling by an effective two-level system as we did in chapter 1. The Raman Rabi frequency for a two-photon stimulated Raman transition is given by [15]

$$\Omega_R = \frac{2\Omega_\downarrow \Omega_\uparrow}{\Delta_R} \tag{2.2}$$

where $\Omega_\downarrow$ and $\Omega_\uparrow$ are the Rabi frequencies for the coupling of $|\downarrow\rangle \leftrightarrow 3P$ and $|\uparrow\rangle \leftrightarrow 3P$ transitions respectively. They can be calculated from eq. (1.2) taking into account that all states of the $3P$ manifold have to be considered for the transition matrix element $\langle a|\hat{x}|b\rangle$. Using the Raman laser beam intensities $I_\downarrow$ and $I_\uparrow$ we may also conclude

$$\Omega_R \propto \frac{\sqrt{I_\downarrow I_\uparrow}}{\Delta_R}. \tag{2.3}$$

Note that these equations for the Rabi frequency are only strictly valid for co-propagating (= parallel) Raman beams. Other beam configurations introduce a coupling between the electronic and motional states, which changes the Rabi frequency (see below).

2.4.2. AC Stark shifts

Each Raman laser (coupling one of the qubit levels to the $3P$ manifold) causes an energy shift of the respective qubit level. This effect can be attributed to the intense applied laser field—or more precisely: to the strong alternating electric field, which is why it is called an AC Stark shift. The energy shifts can be determined by [23]

$$\Delta E_i = \hbar \frac{\Omega_i^2}{\Delta_R} \tag{2.4}$$

where $i = \downarrow, \uparrow$.

The AC Stark shifts are not exactly equal for the two qubit states of $^{25}\mathrm{Mg}^+$. This introduces problems as the energy gap between the $|\downarrow\rangle$ and $|\uparrow\rangle$ states then becomes dependent on the applied Raman laser intensity. This means we would have to adapt the frequency difference of the Raman beams to their intensity. Fortunately, we can reduce the influence of AC Stark shifts by sufficiently large detunings Δ_R.

2.5. Coupling qubit and motional states

In the dipole approximation we may describe the coupling between an ion and a laser beam by the interaction Hamiltonian

$$\hat{H}_{\text{int}} = -\hat{\mathbf{p}} \cdot \mathbf{E}(\hat{\mathbf{x}}, t) \tag{2.5}$$

where $\hat{\mathbf{p}}$ is the electric dipole moment operator of the ion and $\mathbf{E}$ is the electric field vector at position $\hat{\mathbf{x}}$. The coupling between $\hat{\mathbf{p}}$ and $\hat{\mathbf{x}}$ can be approximated by expanding the electric field in a power series:

$$\hat{H}_{\text{int}} = -\hat{\mathbf{p}} \cdot \left[\mathbf{E}(0,t) + (\hat{\mathbf{x}} \cdot \nabla)\mathbf{E}|_{\mathbf{x}=0} + \mathcal{O}(\mathbf{x}^2)\right] \tag{2.6}$$

The essential term is the gradient term. It introduces the coupling between the electronic (qubit) and the motional states.

The direction of motion in which coupling occurs is determined by the difference of the wavevectors of the two Raman beams $\Delta\mathbf{k}$ [23]. In principle, we may choose any direction by appropriately adjusting the angles between the two beams. Throughout this thesis however we will restrict ourselves to coupling in the trap's axial direction $\hat{z}$ (also see fig. 3.1): Both beams propagate perpendicular to each other where the difference of their wavevectors points in the axial direction so that $k_{\text{eff}} = |\Delta\mathbf{k}| = \sqrt{2}k_1 = \sqrt{2}k_2$ as the moduli of their wavevectors are virtually equal.

When these two laser beams shine onto the ion, they drive Rabi oscillations between the states $|\downarrow, n\rangle$ and $|\uparrow, n'\rangle$ where n and n' are not necessarily equal motional states (in contrast to the co-propagating case of section 2.4.1). The Raman Rabi frequency is now given by [15]

$$\Omega_{n',n} = \Omega_R e^{-\eta^2/2} \sqrt{\frac{n_<!}{n_>!}} \eta^{|n'-n|} L_{n_<}^{|n'-n|}(\eta^2) \tag{2.7}$$

where Ω_R is the co-propagating Raman Rabi frequency from eq. (2.2), $n_<$ ($n_>$) is the smaller (greater) of n and n', L_n^α is the generalised Laguerre polynomial, η is the so-called Lamb-Dicke parameter defined by

$$\eta = k_{\text{eff}} z_0 \tag{2.8}$$

and z_0 is the zero-point wavepacket spread of the ion in the axial direction $\hat{z}$. For our trap $\eta \approx 0.3$. Note that $\Omega_{n',n} = \Omega_{n,n'}$.

Three cases are of special interest:

- $n' = n$. In this case $\Omega_{n,n} = \Omega_R e^{-\eta^2/2} L_n(\eta^2)$ where L_n is the (usual) Laguerre polynomial. As the motional state is unchanged by this transition it is called the *carrier*.
- $n' = n - 1$. The motional state is reduced by one, which is why this transition is called the first *red sideband* transition. If $n = 0$ there is no lower motional state that could be reached, so the red sideband cannot be driven anymore.
- $n' = n + 1$. The motional state is increased by one. We call such a transition the first *blue sideband* transition.

Mathematically, things become a lot easier in the Lamb-Dicke limit which is characterised by a wavepacket spread in the axial direction that is much less than the effective laser wavelength, i. e.

$$\langle \psi_{\text{motion}} \mid k_{\text{eff}}^2 z^2 \mid \psi_{\text{motion}} \rangle \ll 1. \tag{2.9}$$

(This criterion is not strictly met for ions in our trap.) In this limit the Laguerre polynomials L_n^α converge rather quickly and thus yield simpler expressions for eq. (2.7). Interestingly, the Hamiltonian for a red sideband transition in the Lamb-Dicke limit can be written as a Jaynes-Cummings Hamiltonian. This type of Hamiltonian [25] actually describes the time evolution of a two-level atom coupled to a single mode of the quantised radiation field*.

The rather large Lamb-Dicke factor $\eta \approx 0.3$ of our trap makes it possible to drive not only first sideband transitions $n \leftrightarrow n \pm 1$ but also second sideband transitions $n \leftrightarrow n \pm 2$. The Rabi frequencies for these transitions are smaller than their first sideband counterparts ($\Omega_{2,0} = 0.21\Omega_{1,0}$) which requires longer π pulses, but this is still in the feasible range of our experimental setup. Smaller η would further increase the π time of second sideband transitions, eventually rendering this type of transitions inaccessible (due to decoherence occuring at similar timescales).

---

*Several cavity-QED experiments implement this Hamiltonian directly.

2.6. Cooling the ions' motion

Our quantum simulation experiments will rely on an efficient initialisation of the ions' motional state. As an example consider the simulation of cosmological particle creation [9]. The crucial measurement will be to detect a change in the population of the motional state $n = 2$, ideally from zero to some finite value. This is only possible if the better part of the population has previously been transferred to the motional ground-state $n = 0$.

As the ions usually carry a considerable amount of kinetic energy after having been loaded into the trap, they have to be cooled. In our setup we use two methods for cooling both driven by laser transitions to eventually reach the motional ground-state.

2.6.1. Doppler cooling

Consider a magnesium ion travelling towards our slightly red-detuned BD laser source (frequency ω) with velocity v. Due to the first-order relativistic Doppler shift it will experience a shifted frequency

$$\omega' \doteq \omega \left(1 + \frac{v}{c}\right) \tag{2.10}$$

where c is the speed of light. If ω' matches the actual BD transition frequency, one photon is absorbed thereby transferring negative momentum

$$p_1 = -\frac{\hbar\omega}{c} \tag{2.11}$$

onto the ion. The subsequent fluorescent emission can either occur by stimulated emission (in which case the ion re-gains a momentum of $p_2 = -p_1$; the net momentum transferred vanishes) or spontaneously. For isotropic spontaneous emission the mean transferred net momentum is thus determined by eq. (2.11). As long as the ion can absorb counterpropagating photons from the BD laser, it will thus slow down, losing energy.

The optimum conditions for this process of Doppler cooling obviously depend on the velocity of the ion. For faster ions we will have to red-detune the BD laser by greater amounts than for ions that have already been cooled. The minimum temperature T_D

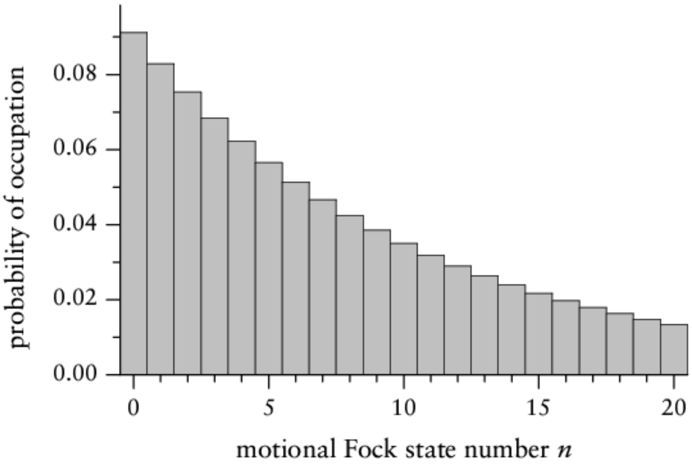

Figure 2.5.: Occupation probabilities of the motional Fock states characterised by their number n for a Doppler-cooled ion at a temperature of $T_D = 1\,\mathrm{mK}$. We assumed a harmonic potential characterised by $\omega_z = 2\pi \cdot 2\,\mathrm{MHz}$. The mean motional quantum number for this distribution is $\overline{n} = 10$.

that can be reached using Doppler cooling is the *Doppler cooling limit* determined by [21]

$$T_D = \frac{\hbar\Gamma}{2k_B} \approx 1\,\mathrm{mK} \tag{2.12}$$

where $\Gamma = 2\pi \cdot 43\,\mathrm{MHz}$ is the radiative linewidth of the BD transition and k_B is the Boltzmann constant. It represents a lower limit on the temperature, which is reached for a red-detuning with respect to the resonance frequency of $\Delta = \Gamma/2$ [26]. Laser intensity is kept below the saturation intensity at about $(2/3)I_{\text{sat}}$ in order to avoid power broadening effects, see section 1.2.1.

The occupation of motional states after Doppler-cooling follows a Maxwell-Boltzmann distribution. The stronger the confinement of the ions, the more population will reside in the lower motional states, see fig. 2.5.

2.6.2. Resolved-sideband cooling

It is desirable to initialise our qubit in a way that most of the population resides in one particular motional state. The Rabi frequency will then be well-defined even for an orthogonal Raman beam geometry, see section 2.5. The method of choice is to cool as much population as possible into the motional ground state $|\downarrow, n = 0\rangle$. If we calculate the motional occupation numbers for an ion that has been pre-cooled to the

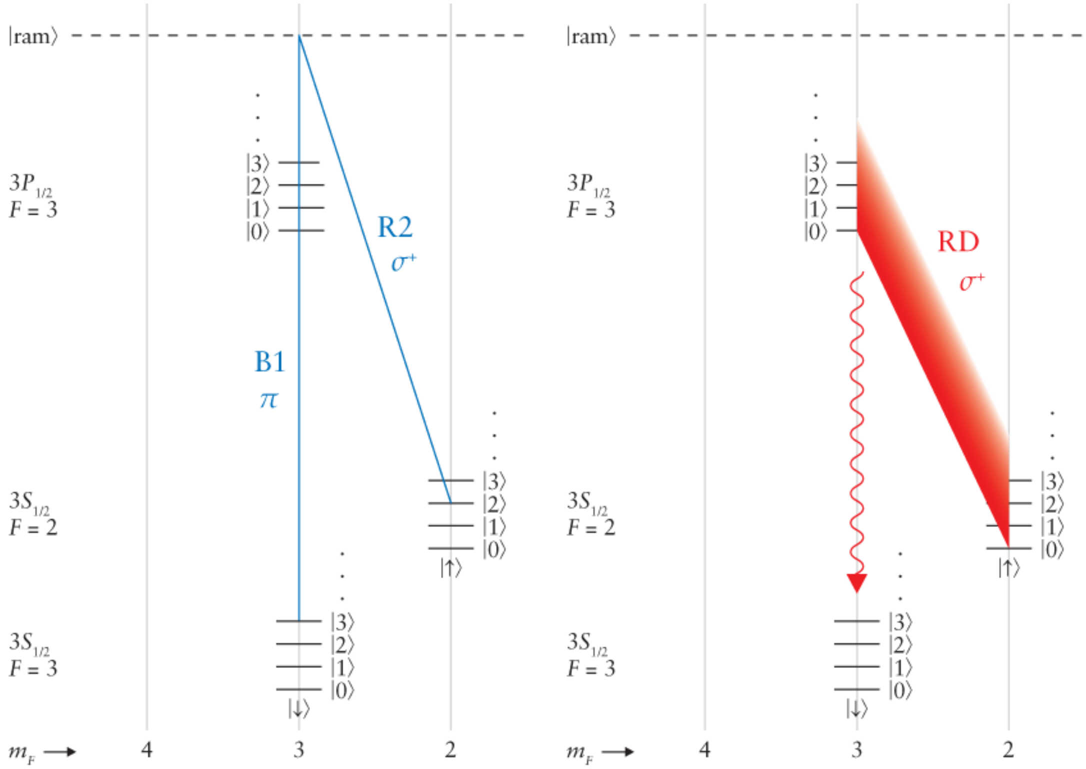

(a) First step: Red sideband π-pulse using a two-photon stimulated Raman transition.

(b) Second step: Optical pumping into the ground state $|{\downarrow}\rangle$ using the Red Doppler beam.

Figure 2.6.: Resolved-sideband cooling of $^{25}\mathrm{Mg}^{+}$. The figures illustrate the cooling process from $n = 3$ to $n' = 2$.

Doppler limit $T_D = 1\,\mathrm{mK}$ we however find that the probability for an ion to be in the motional ground state is only about 9%, see fig. 2.5. For proper state initialisation we however require probabilities of $> 90\%$. This means that we have to transfer at least the occupation of the motional states $|1\rangle$ thru $|24\rangle$ into the ground state $|0\rangle$.

We use the method of resolved-sideband cooling for this purpose [26, 27, 28]. Starting with a red sideband π-pulse optimised for $n = 24$ we first drive the transition $|{\downarrow}, 24\rangle \rightarrow |{\uparrow}, 23\rangle$ and then optically pump the population into $|{\downarrow}, 23\rangle$, not changing the motional state of the ion, see fig. 2.6.

The optical pumping process uses the Red Doppler (RD) beam to transfers the population into the $P_{1/2}\,|F = 3, m_F = 3, n = 23\rangle$ state which then decays into $|{\downarrow}, 23\rangle$ by spontaneous emission. As some part of the $P_{1/2}$ population might however decay into the $S_{1/2}\,|F = 3, m_F = 2\rangle$ state (see fig. 2.1), we subsequently shine onto the ion with the repumper beam that resonantly couples $S_{1/2}\,|F = 3, m_F = 2\rangle \leftrightarrow P_{1/2}\,|F = 3, m_F = 3\rangle$. It clears the population in $|F = 3, m_F = 2\rangle$ state by optically pumping it into $|{\downarrow}\rangle$. Both the optical pumping beams are enabled for a duration allowing for several scattering events to occur. This ensures that even population which is scattered back into its initial state is eventually transferred into $|{\downarrow}\rangle$. In the end, most of the population initially in $|{\downarrow}, 24\rangle$ will have been transferred to $|{\downarrow}, 23\rangle$.

In the Lamb-Dicke limit (2.9) the recoil energy due to the spontaneous emission processes is small compared to the energy of the motional quanta. As mentioned above, we may thus neglect excitations of the motional spectrum in first order.

The two-photon stimulated Raman pulses applied to transfer $n = 24$ into $n' = 23$ will also affect the other motional states $n < 24$. As their Rabi frequencies $\Omega_{n-1,n}$ will be different from $\Omega_{23,24}$, we cannot concurrently drive these transitions with high efficiencies. Instead, population in these other motional states will somehow distribute over n and $n-1$. Anyhow, the important thing about this iteration $n = 24 \rightarrow n' = 23$ of sideband cooling is the fact that the motional state $n = 24$ will be depleted afterwards. It will thus not be populated by subsequent sideband cooling iterations. Iterating the sideband cooling processes over the lower motional states ($n = 23 \rightarrow n' = 22$, $n = 22 \rightarrow n' = 21$, etc.) we will eventually transfer most of the population initially occupying the motional states $0 \leq n \leq 24$ into $n' = 0$.

As shown in chapter 9 we obtain mean motional quantum numbers of $\overline{n} = 0.6$ after resolved-sideband cooling. For even lower values we would have to increase the ions' confinements as described in [28].

Part II.

Assembly of the experimental apparatus

3. Trap apparatus

The magnesium ions used for experimentation throughout are stored inside a quadrupole trap operated in the radio frequency (RF) range. The trap itself is kept inside an ultra-high vacuum ($p < 10^{-10}$ mbar) so as to isolate the ions from noise, collisions, or other perturbing signals of the surrounding environment thus allowing for rather long quantum state lifetimes and precise quantum state manipulation.

3.1. Linear Paul trap

For our experiments we use a segmented linear Paul trap, fig. 3.1. In a rough view the trap consists of four electrodes where two opposing ones (2 and 4) are grounded and the other two (1 and 3) are connected to an RF voltage. The associated RF quadrupole potential radially confines the positively charged ions to the trap axis $\hat{z}$, which lies parallel to the electrode surfaces.

If we take a closer look on the RF-grounded electrodes we can see that they are each segmented into six independent sub-electrodes, fig. 3.2. Any three opposing pairs of the 2x6 sub-electrodes are able to provide a confining potential along the trap axis by keeping them at suitable static (DC) voltages. As long as the outer sub-electrode pairs are kept at a higher voltage than the middle one, the ions will align nearby the middle electrode. In conjunction with the radial RF potential, ions can be confined or shuttled to arbitrary positions along the trap axis.

The trap can be divided into two regions characterised by the distance R of the electrodes from the trap centre: The loading region ($R = 800\,\mu\text{m}$) and the storage or experimentation region ($R = 400\,\mu\text{m}$). We use the loading region solely to ionise atoms from a thermal atomic beam and load them into the trap. That way we can avoid the contamination of the electrodes in the experimentation region with magnesium atoms. The bigger size of the loading regions allows for a good penetration by the atomic beams whereas the smaller size of the experimentation region is able to provide a stronger confinement. By appropriately altering the DC voltages we can shuttle the ions along

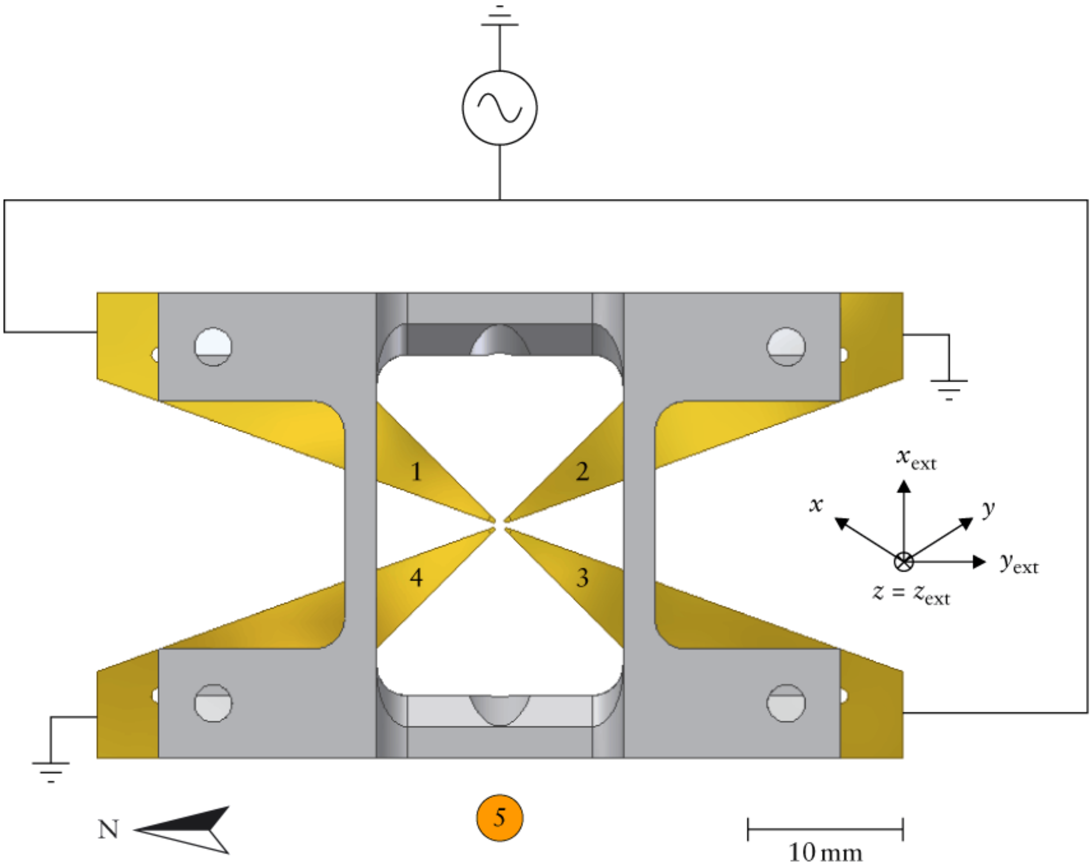

Figure 3.1.: Western view of the employed ion trap. x, y, and z denote the non-orthogonal trap-inherent directions, while x_{ext}, y_{ext}, and z_{ext} represent an external orthogonal coordinate system. Part no. 1–4: electrodes. Part no. 5: compensation electrode.

the axis and transfer them from the loading region into the experimentation region with near 100% efficiency. All experiments will be carried out in the experimentation region.

3.1.1. Radial confinement

Radial confinement to the trap axis is provided by an RF potential. This method of confining positively charged particles using alternating electric fields [29] has first been described by Wolfgang Paul (Nobel prize in 1989).

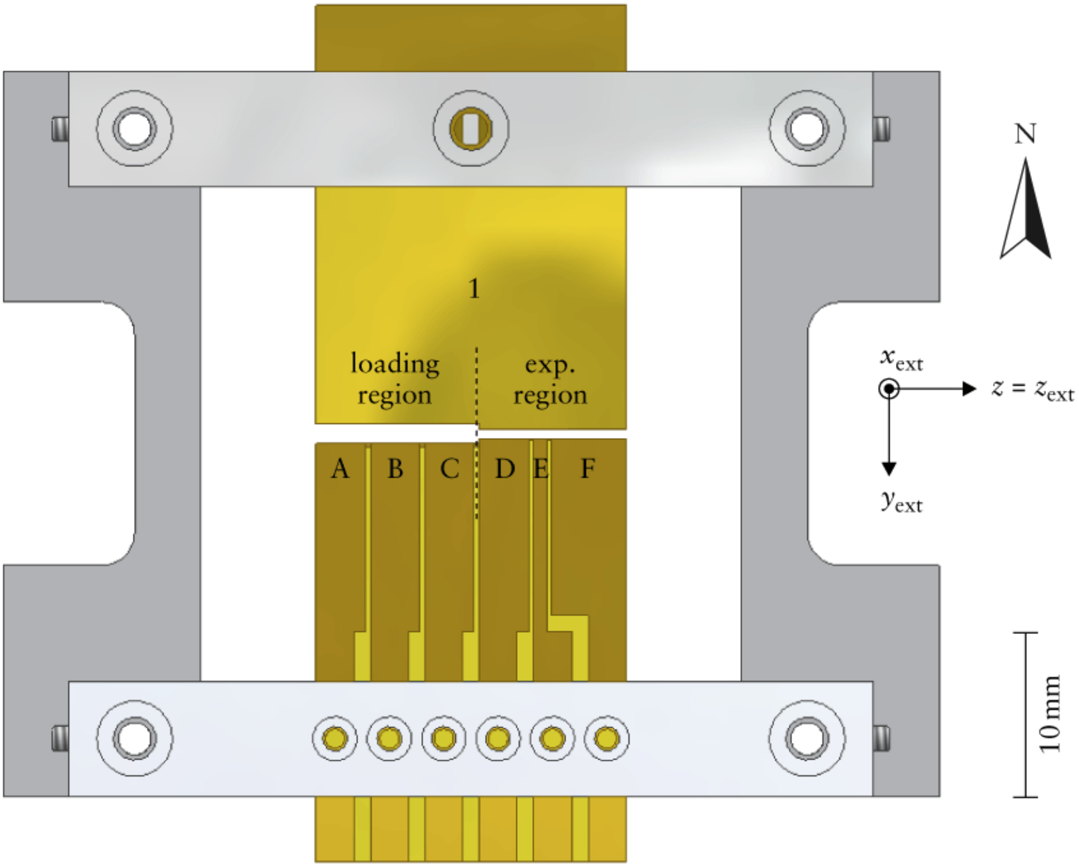

Figure 3.2.: Top view of the employed ion trap. x_{ext}, y_{ext}, and z_{ext} represent the external orthogonal coordinate system.

We will be storing ions of mass m. For this purpose, we apply a trapping voltage $V_0 \cos \Omega_{\text{RF}} t$ to electrodes 1 and 3 of our trap. The two remaining electrodes 2 and 4 (more precisely: the respective DC subelectrodes) are kept at a constant DC voltage U_0. As mentioned before, the minimum distance from the electrode surface to the trap centre is denoted by R. The equations of motion for such a system each have the type of a Mathieu differential equation which can be solved analytically for the radial directions $\hat{x}$ and $\hat{y}$ [30]. The first order solution is

$$\begin{aligned} x(t) &= x_0 \cos(\omega_x t + \phi_x) \left(1 + \frac{q}{2} \cos \Omega_{\text{RF}} t\right), \\ y(t) &= y_0 \cos(\omega_y t + \phi_y) \left(1 - \frac{q}{2} \cos \Omega_{\text{RF}} t\right), \end{aligned} \tag{3.1}$$

where x_0, y_0, ϕ_x, and ϕ_y are determined by the initial conditions. We introduced the dimensionless parameters

$$\begin{aligned} a &= \frac{4eU_0}{m\Omega_{\mathrm{RF}}^2 R^2}, \\ q &= \frac{2eV_0}{m\Omega_{\mathrm{RF}}^2 R^2}. \end{aligned} \tag{3.2}$$

ω_i are the so-called secular frequencies defined by

$$\begin{aligned} \omega_x &= \frac{\Omega_{\mathrm{RF}}}{2}\sqrt{\frac{q^2}{2}+a}, \\ \omega_y &= \frac{\Omega_{\mathrm{RF}}}{2}\sqrt{\frac{q^2}{2}-a}. \end{aligned} \tag{3.3}$$

As we can see, the ions' motion in each of the two radial directions can be divided into two parts (see fig. 3.3):

- Secular motion with angular frequency ω_i, also called macromotion. The associated frequencies determine the effective depth of our radial potentials

$$\begin{aligned} \Phi_x &= \frac{1}{2}m\omega_x^2 x^2, \\ \Phi_y &= \frac{1}{2}m\omega_y^2 y^2. \end{aligned}$$

- Micromotion with the driving frequency Ω_{RF}. As the ion is displaced from the trap axis, the distances to the opposing trap electrodes are not any more equal. Therefore the ion's motion is driven with the RF frequency.

We use a common frequency generator (Hewlett-Packard HP8640B) connected to an RF amplifier (Amplifier Research 10W1000) to generate the trapping RF voltages. They deliver a maximum output power of 44 dBm or 27 W. We further amplify the voltage via a high-Q helical resonator transformator connected to the chamber ($Q_{\mathrm{total}} = 90$) with a fixed driving frequency of $\Omega_{\mathrm{RF}} = 56\,\mathrm{MHz}$. This setup allows for RF voltages up to 1100 V. Associated secular frequencies range up to 8.2 MHz.

During the first two hours of operation, the electrodes will heat up due to resistive losses. As a result, the trap geometry changes slightly and a portion of the applied RF power is backreflected into the RF amplifier. We manually optimise the injection

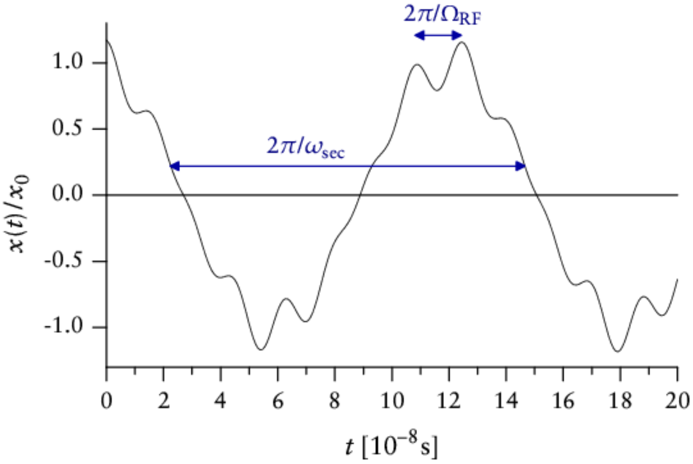

Figure 3.3.: First order solution for the radial $\hat{x}$ motion of a single $^{25}\mathrm{Mg}^+$ ion in the experimentation region of our trap. The following parameters were used to produce this figure: $U_0 = -10\,\mathrm{V}$, $V_0 = 1000\,\mathrm{V}$, $\Omega_{\mathrm{RF}} = 56\,\mathrm{MHz}$. This yields $a = 7.78 \cdot 10^{-3}$, $q = 0.389$. Once an ion has been cooled, the oscillation amplitude is very small: $x_0 < 0.1\,\mu\mathrm{m}$.

efficiency by adjusting the position of the coil inside the helical resonator. Special care must be taken not to exaggerate the injected RF power as highly temperated electrodes will decrease the lifetime of stored ions. The micromotion compensation settings (see chapter 8) are also highly sensitive to a thermal deformation of the trap.

3.1.2. Axial confinement

Axial confinement of the ions is provided by applying DC voltages to the sub-electrode segments. The depth of this potential well and thereby its resonance frequency was estimated using the commercially available software package SIMION. For the experimentation region (see fig. 3.2) where sub-electrodes D and F are connected to a voltage of magnitude U_{axial} and sub-electrode E is kept at ground we can calculate

$$\omega_z = \sqrt{\frac{2eU_{\mathrm{axial}}}{mz_0^2}} \tag{3.4}$$

where z_0 is the “width” of the harmonic potential. SIMION determined a value of $z_0 = 4.1\,\mathrm{mm}$. We applied a low-amplitude RF voltage to the central sub-electrode

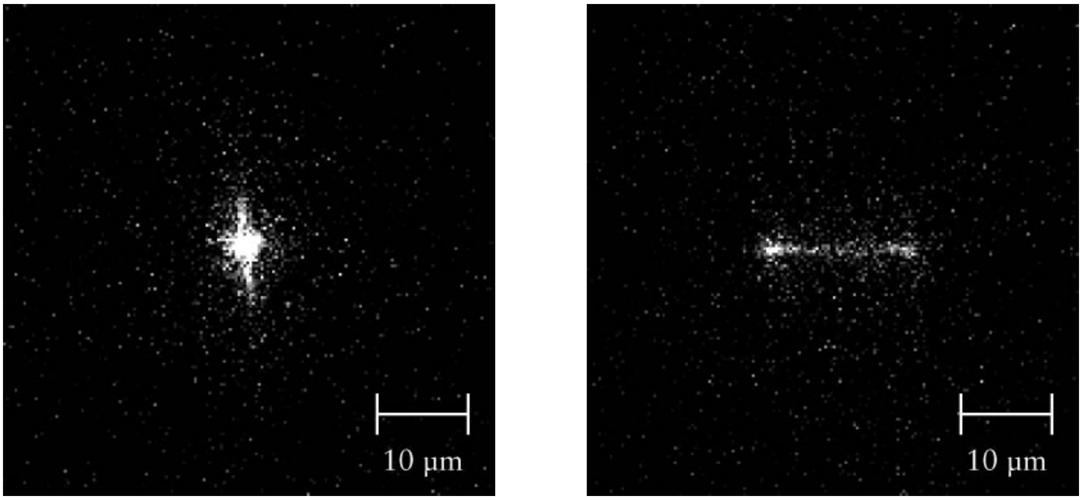

(a) Focused image of an ion. (b) Ion excited in the axial direction.

Figure 3.4.: CCD camera images of an ion at a BD intensity of $I = (2/3)I_{\mathrm{sat}}$. Exposure time was 100 ms.

E and thereby resonantly excited the ion motion, which can be observed using our camera, fig. 3.4. That way we rather estimate $z_0 = (1.40 \pm 0.05)\,\mathrm{mm}$.

It is desirable to make the axial confinement as strong as possible. This will improve the efficiency of Doppler pre-cooling (see section 2.6.1) and reduce the probability of motional excitation by thermal effects. Normally, we would operate at an axial confinement of $2\pi \cdot 2\,\mathrm{MHz}$.

Due to the lack of damping, ions in the trap can be excited very efficiently. In order to reduce unwanted excitation by injection of external noise all of the DC sub-electrodes have been equipped with low-pass filters. The cutoff frequencies are $2\pi \cdot 5\,\mathrm{MHz}$ each, with the exception of the filter for the central sub-electrode which has a cutoff frequency of $2\pi \cdot 2\,\mathrm{MHz}$. That way higher frequency noise is banned from entering the trap, ramping the axial potential as required for simulating cosmological particle creation is however still possible at slew rates of $40\,\mathrm{V/\mu s}$.

3.1.3. Mutual interference of confinements

From an experimentator's point of view it is desirable to have completely decoupled confinements in the radial and axial directions. This is however not true for the design of our trap.

Without any additional radial confinement (RF supply switched off), DC voltages applied to subelectrodes D and F will cause a focusing effect in the $\hat{z}$ direction *and* in the $\hat{y}$ direction (see fig. 3.1 for the coordinate axes). Both confinements can be associated positive frequencies ω_x and ω_y. Due to Poisson's equation $\Delta\Phi = 0$ for the potential Φ there must however be a net defocusing effect in the $\hat{x}$ direction, equivalent to an imaginary frequency $i\omega_x$. The stronger the radial confinement ω_z, the greater will be the frequency splitting of the radial frequencies $\Delta\omega_r = \omega_x - \omega_y$.

The defocusing effect in the $\hat{x}$ direction is compensated by a sufficiently strong RF radial confinement. As we have seen in section 3.1.1, the axial confinement may give rise to two different secular frequencies whose splitting

$$\omega_x - \omega_y \approx \Omega_{\mathrm{RF}} \frac{a}{\sqrt{2}q} \text{for } a \ll q^2 \tag{3.5}$$

depends on the voltage U_0 applied to the central DC subelectrode, e. g. subelectrode E for the experimentation region.

If an ion's z position is not centred in the region between two opposing DC subelectrodes, it will oscillate with the RF frequency. This effect can be attributed to the asymmetric geometry of our trap: The DC subelectrodes are separated by slits whereas the RF electrodes aren't. An axial off-position will thus induce a net oscillating force on the ion. See chapter 8 for further micromotion effects.

The optimum z position (where the ion is not oscillating) is furthermore dependent on the strength of the applied RF potential. This effect is probably caused by slight changes in trap geometry due to RF dependent heating of the electrodes.

3.1.4. A word on trap geometries

Several research groups have demonstrated the fabrication and operation of ion traps featuring electrode – ion distances of 100 µm and below [31]. Obviously, these designs are suitable for incorporation into larger arrays of ion traps. They however usually suffer from relatively high motional heating rates $\propto R^{-4}$. Motional coherence times for the stored ions thus diminish for shrinking trap sizes. For our single trap setup we chose a rather large trap geometry of $R = 400\,\mu\mathrm{m}$ in order to minimise these heating effects. We expect γ to be smaller than 0.01 excited quanta per millisecond at an axial confinement of $\omega_z = 2\pi \cdot 2\,\mathrm{MHz}$. As the durations of typical experiments are of the order of 1 ms, heating should not be an issue.

3.1.5. Compensation electrode

The trap apparatus is completed by one compensation electrode consisting of a piece of copper wire (3 mm in diameter) which is located beneath the trap axis, see fig. 3.1. This electrode can be used to compensate for imperfect external DC fields in the up-down direction, see chapter 8. By appropriately tuning the DC voltages applied to the sub-electrodes we can as well create compensation fields in the horizontal directions—radially by differential voltages applied to an opposing subelectrode pair and axially by appropriate voltages of neighbouring subelectrode pairs.

3.2. Vacuum chamber

To minimise ion loss due to collisions with residual gas particles, we have to provide a vacuum of better than 10^{-10} mbar. Evacuation to the ultra-high vacuum level was attained as follows:

1. Evacuation using an oilfree molecular turbopump system (Pfeiffer Vacuum) in combination with an oilfree scrollpump for forepumping for about 24 hours. According to an electronic full-range gauge (rangeability: atmospheric pressure down to 10^{-9} mbar) we obtained pressures of 10^{-7} mbar.
2. Baking out the vacuum chamber. Using a home-built brick oven, the vacuum chamber was baked out at 150 ℃ for a duration of approximately seven days, all the time being connected to the turbopump system. Pressure inside the chamber eventually decreased back to 10^{-7} mbar.
3. Running the ion getter pump in conjunction with the titanium sublimation pump while the chamber cooled down. At room temperature, a pressure level of some 10^{-10} mbar was obtained. These measurements were carried out using an ion gauge system (Granville-Phillips model 350).
4. Titanium sublimation. The titanium sublimation pump was run several times, which again lowered the pressure to several 10^{-11} mbar.
5. Installation of the vacuum chamber on an optical table.

We secured the ion getter pump against power failure using an uninterruptible power supply (UPS). Power interruptions of up to two hours can be bypassed that way. The titanium sublimation pump is run about once a month for a few minutes. Every run precipitates titanium over the inner surface of a double-walled cylinder which is connected to the getter pump housing and can be cooled using liquid nitrogen.

Our ion gauge system is calibrated for a nitrogenic atmosphere, which certainly differs from the composition of the residual gas inside the chamber. Furthermore, at pressures of 10^{-10} mbar and below, we operate the gauge close to its sensitivity limit. The indication of the gauge will thus probably differ from the actual pressure inside the chamber. In practice, we use the ion lifetime inside our trap to judge pressure. While this may not provide a quantitative measure of the pressure itself, it is the quantity of interest that matters with quantum simulations. Depending on the temperature of the electrodes we attained ion lifetimes between two hours (at maximum RF power on the electrodes) and ten hours and above (at moderate RF settings).

The vacuum chamber is equipped with a total of twelve ports, see fig. 3.5. Port C is the connector for the helical resonator, port D acts as a feedthrough for the DC voltages applied to the trap subelectrodes. Two windows serve as observation ports where the upper port A is designated for electronic observation systems (camera, photomultiplier) and port B can be used to have a look inside the chamber. All other eight ports have considerably smaller 1-inch windows coated for maximum transmission at 280 nm. They are used exclusively to shine into the trapping volume using UV laser beams from different directions:

- Four windows serve beams from the north-eastern (E), south-eastern (F), south-western (G), and north-western (H) directions. All of these beams propagate parallel to the optical table layer.
- Another four windows serve beams from the eastern (J, K) and western (L, M) directions. The propagate at angles of 20° relative to the optical table layer.

All windows are made from fused silica which is transparent to UV radiation and does not exhibit any birefringence. An exception is port A which has a sapphire crystal window. It is part of the diffraction limited optics for the CCD camera and as such required by the objective attached to port A for optimum image quality, see section 5.3.

3.3. Ion source

To store ions inside a Paul trap, they have to be ionised inside the active trapping region near the centre of the trap. Our trap apparatus features three independent

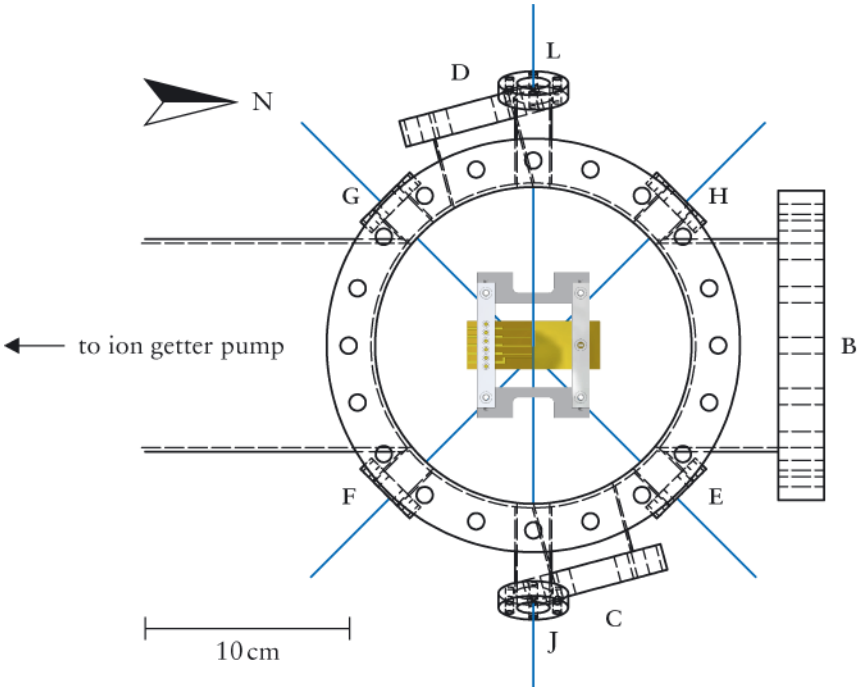
N
L
D
G
H
to ion getter pump
B
F
E
C
J
10 cm

(a) Plan view.

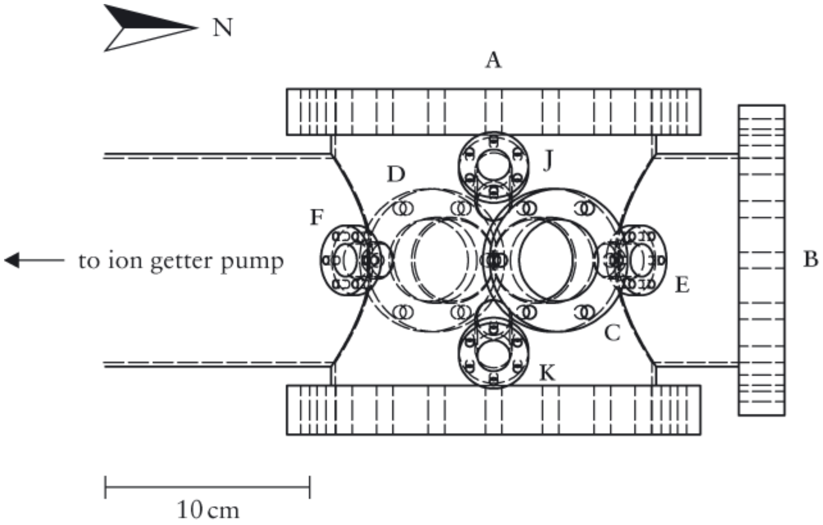
N
A
J
D
F
to ion getter pump
B
E
C
K
10 cm

(b) Eastern view.

Figure 3.5.: Sketches of the vacuum chamber. Laser beams entering the chamber are drawn in blue colour.

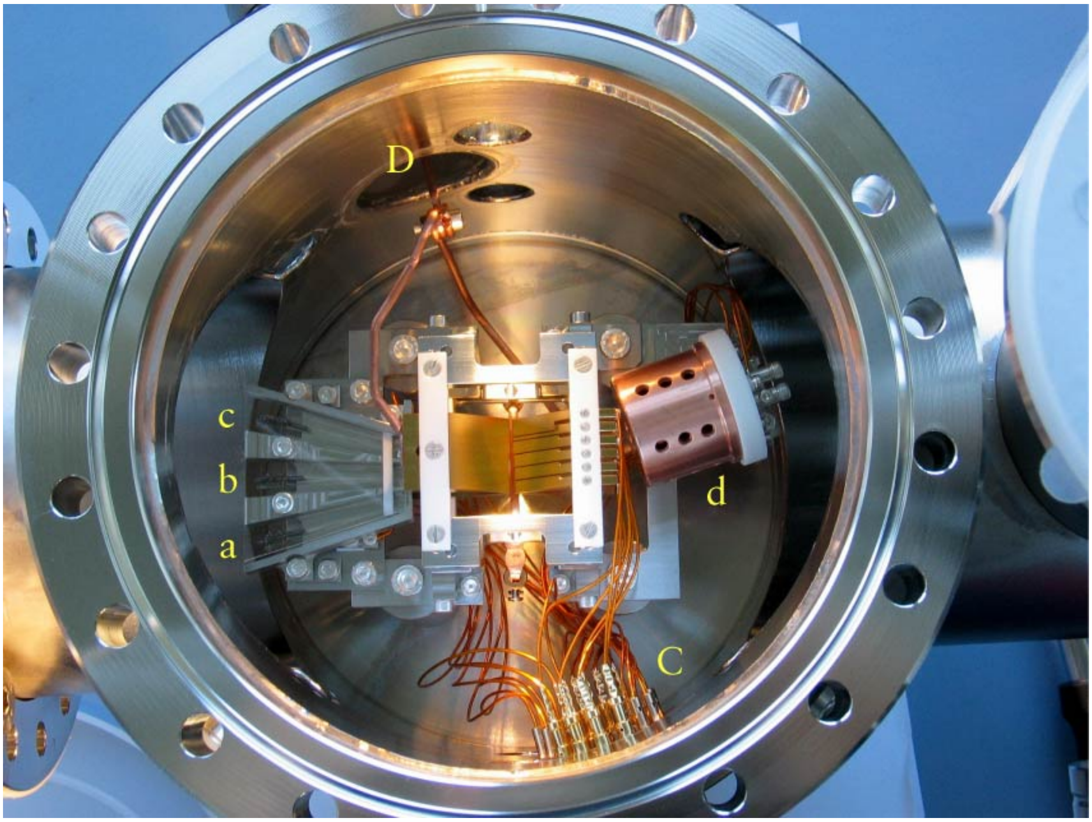

Figure 3.6.: Top view of the whole trap apparatus. Ports are denoted with uppercase letters. Legend: a, b, c = atomic ovens; d = electron gun.

atomic ovens emitting their atoms into the centre of the loading region where we photo-ionise them (laser beam through port L), see fig. 3.6. In addition, we have an electron gun for backup / emergency purposes. All ovens consist of tantalum tubes (length $l \approx 10\,\mathrm{mm}$, diameter $d \approx 1\,\mathrm{mm}$) whose rear halves are filled with a granulate of magnesium. We fixed the ovens in their respective positions using two tantalum wires soldered to the tubes. These also serve as current entries, actually heating the ovens. Oven A contains a natural composition of magnesium isotopes, i. e. 79% ^{24}Mg, 10% ^{25}Mg, and 11% ^{26}Mg, while the other two ovens B and C emit isotopically enriched ^{25}Mg atoms. The ovens are arranged such that oven B emits its atoms perpendicular to the direction of the ionising beam and ovens A and C share an angle of 15° relative to oven B. This setup allows us to selectively load ^{24}Mg$^+$, ^{25}Mg$^+$ or even ^{26}Mg$^+$.

oven	Mg isotope	typical oven current [A]	$3s^2 \rightarrow 3s3p^1P_1$ frequency [$2\pi \cdot 10^{15}$ Hz]
A	^{24}Mg	2.1	1.050811538
B	^{25}Mg	*not yet measured*	*not yet measured*
C	^{25}Mg	2.2	1.050811834

Table 3.1.: Resonant $3s^2 \rightarrow 3s3p^1P_1$ transitions for photo-ionising magnesium as determined from the Doppler-free spectroscopy setup. With the oven currents indicated we are able to load a single ion into the trap on a 60 s timescale.

We supply currents between 2.1 A and 2.4 A to load ions into the trap with a rate of between one and fifty ions per minute.

Photo-ionisation of the magnesium atoms is implemented by a two-photon absorption process [32]: First, one electron of the $3s$ level is shifted to the $3p$ level ($3s^2 \rightarrow 3s3p^1P_1$) by resonant excitation at 285 nm. The same wavelength can be used to eventually ionise the magnesium atom by transferring the excited electron into the continuum [33]. We use a frequency-doubled dye laser to accomplish this task. The absolute photo-ionisation frequencies can be determined using Doppler-free iodine saturation spectroscopy (see section 4.4) in front of the frequency doubling stage, i. e. at 570 nm and are summarised in tab. 3.1. Doppler shifts have to be taken into consideration for ovens A and C. For the oven currents used in our setup, we can estimate temperatures of $T \approx 600$ K.

The process of photo-ionisation has several advantages over the electron gun method:

- In contrast to an electron beam a photo-ionising laser beam is bundled and will usually not hit the electrode surfaces. Thus, vacuum is affected less.
- A photo-ionising laser beam will not charge the electrode surfaces, which makes micromotion compensation (chapter 8) more stable.
- We may selectively load particular isotopes of magnesium by properly adjusting the ionisation frequency.
- The two-photon ionisation process of magnesium also scatters some fluorescent light, which is why the atomic magnesium beam can be visualised using the photo-ionising laser beam. Therefore, we can easily detect whether the atomic ovens are working and whether the other laser beams are correctly positioned.

One drawback of using photo-ionisation for magnesium is the unavailability of diode or fibre lasers at the required wavelength of 285 nm. We thus use a frequency-doubled dye laser for this purpose.

3.4. Magnetic field

As described in chapter 2 controlled manipulation of the electronic population of $^{25}\mathrm{Mg}^{+}$ requires discrimination of different m_F levels of the states involved. We have to apply a magnetic field to introduce an appropriate Zeeman splitting between the otherwise degenerate m_F levels. For $^{25}\mathrm{Mg}^{+}$ the Zeeman splitting of the qubit shelves ($S_{1/2}$, $|F=2\rangle$ and $|F=3\rangle$) is about 0.5 MHz/G.

3.4.1. Field-generating coils

Due to the geometry of our vacuum chamber it is not advantageous to create a spatially homogeneous magnetic field using Helmholtz's configuration. We have to employ coils whose mutual distance $d = 479\,\mathrm{mm}$ is greater than their mean radius $\overline{r} = 100\,\mathrm{mm}$, see fig. 3.8. This configuration leads to the required field strengths in the centre (see tab. 3.2), but shows a quadratic field dependence on the position between the coils, see fig. 3.7. In the 10 mm vicinity around the centre, relative deviations of the magnetic field still remain below 10^{-4}. Tab. 3.2 summarises the relevant parameters.

inner coil radius	60 mm
outer coil radius	100 mm
distance between coils	479 mm
number of windings per coil	336
resistance per coil	1.1 Ω
inductance per coil	7 mH (estimated)
calculated field at trap centre	1.68 G/A
actual field at trap centre	0.932 G/A
operating current	6.000 A

Table 3.2.: Characteristics of the two field-generating coils. The actual field at the trap centre was determined via Rabi flopping, see section 9.4.

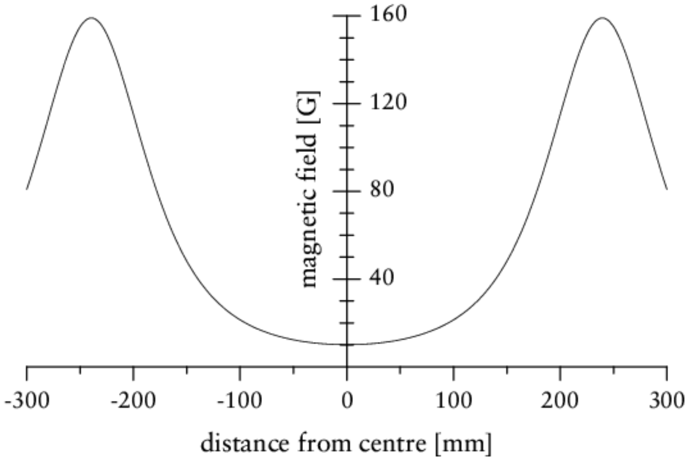

Figure 3.7.: Calculated magnetic field strength induced by the two coils of tab. 3.2 at a current of $I = 6\,\mathrm{A}$.

The great discrepancy between the calculated and actual field strengths at the centre of our trap (44%) could be attributed to ferromagnetic parts in the vacuum chamber or the trap itself. Most probably, the material of the vacuum chamber (non-magnetic stainless steel) contains some ferromagnetic inclusions. The conversion of non-magnetic stainless steel into its ferromagnetic variant is well-known and can occur during cold deformation and welding processes. Our vacuum chamber had to be re-welded several times to eventually seal it. That might have caused ferromagnetic inclusions which effectively weaken the magnetic field in their vicinity.

Normally, we operate the coils at a current of $I = 6\,\mathrm{A}$ which is generated by two low-noise Hewlett-Packard HP6264B power supplies in constant-current mode (ripple and noise $< 5\,\mathrm{mA}$, drift $< 8\,\mathrm{mA}$). The coils' windings are attached on a copper mount to improve heat flow to the outside. After about three hours, the coils will have reached their steady-state temperature of 60 ℃. For higher currents, the coils' temperature rises quickly and adversely affects optical components in the vicinity. Water-cooling the coils would probably improve this situation.

3.4.2. Spatial compensation coils

Being our quantisation axis the magnetic field has to point exactly into the same direction as the wavevector of the beams entering the trap along this axis. Otherwise, it would be impossible to polarise these beams purely $\sigma^{\pm}$ with respect to the field

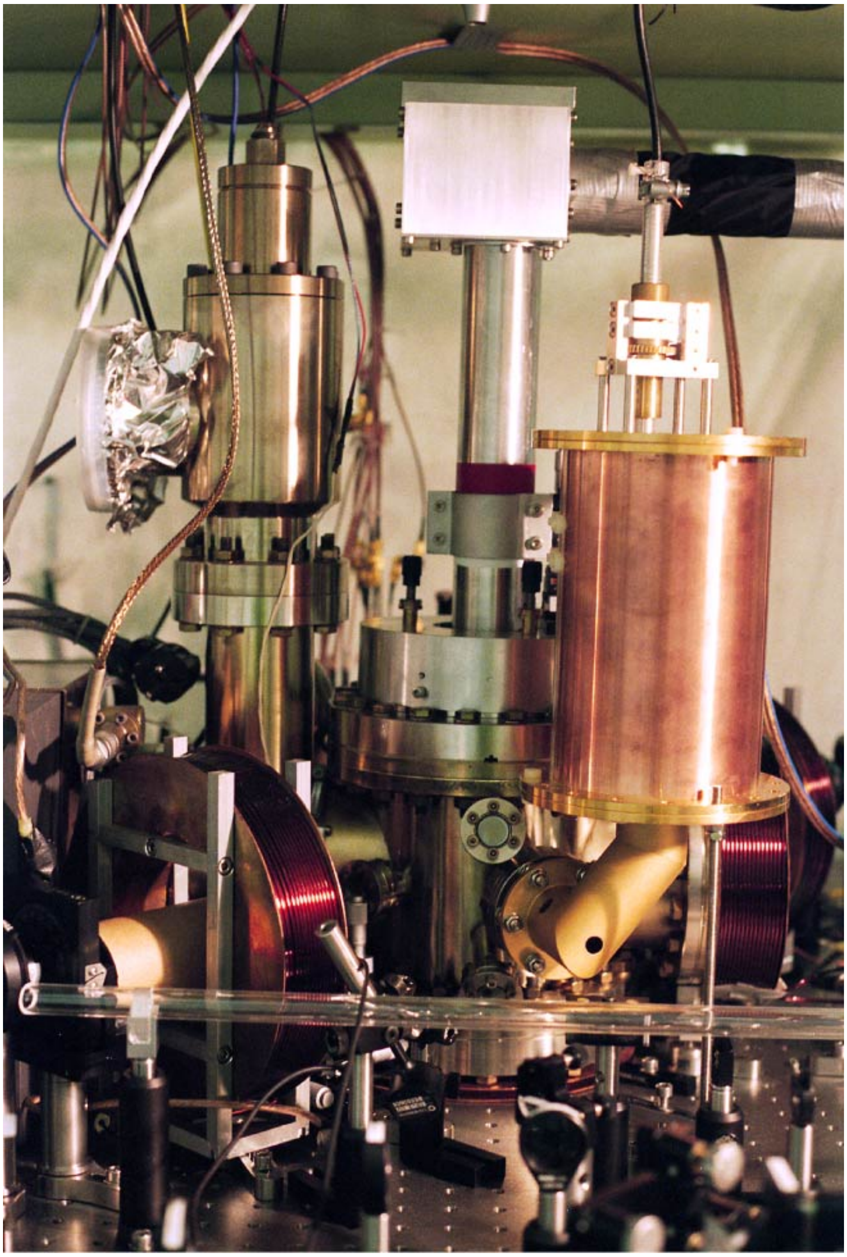

Figure 3.8.: Eastern view of the vacuum chamber. The southeastern field-generating coil is clearly visible at the bottom-left part of the image. The northwestern field-generating coil appears blurred while the spatial compensation coils below and north of the chamber are easy to spot.

Parameter	northern coil	lower coil
mean radius [mm]	81.3	90.7
distance from trap centre [mm]	160.2	119.0
number of windings	60	20
resistance [Ω]	0.3	0.2
inductance (estimated) [mH]	0.2	0.02
calculated field at trap centre [G/A]	0.430	0.309
operating current [A]	3.20	2.95

Table 3.3.: Characteristics of the spatial compensation coils.

axis. This is however important for efficiently driving the cycling detection transition, see section 2.3. Two spatial compensation coils will tilt the magnetic field axis as needed. They are located north and below the vacuum chamber respectively. Their characteristics are summarised in tab. 3.3.

3.4.3. Temporal compensation coil

Temporal changes of the magnetic field strength will cause fluctuating Zeeman shifts and thus reduce the fidelity of operations on quantum states relying on fixed energy levels. Therefore, it is desirable not to have variations in the magnetic field greater than 10^{-4}. We stabilise the magnetic field against external noise and fluctuations of our power supplies using a feedback-regulated system: The signal of a miniature high-precision fluxgate sensor (Stefan Mayer Instruments FLC 100) is processed by a band-pass filter ($3\,\mathrm{Hz} < f < 3\,\mathrm{kHz}$) and a high-current operational amplifier ($I_{\mathrm{max}} = 5\,\mathrm{A}$) supplying the compensation coil. This coil consists of only a few additional windings so as to minimise its inductivity and thus maximise its regulation bandwidth. It is wound directly on one of the field-generating coils. Characteristics are listed in tab. 3.4.

radius	100 mm
distance from trap centre	239.5 mm
number of windings	5
resistance	0.4 Ω
inductance	1.5 µH (estimated)
calculated field at trap centre	18.0 mG/A
regulation bandwidth	DC – 150 kHz

Table 3.4.: Characteristics of the temporal compensation coil.

4. Laser apparatus

All laser beams used throughout experimentation have frequencies lying in the ultraviolet (UV) range. We can identify four main laser sources serving different purposes in a simulation experiment:

1. Photo-ionisation, see section 3.3.
2. Qubit manipulation. In order to drive the transition between the two qubit states, we use a two photon stimulated Raman transition. It involves a virtual level blue-detuned by several tens of GHz with respect to the $3P_{3/2}$ level in order to reduce spontaneous emission effects, see section 2.4.1. Therefore, the respective laser source must be able to provide intensities of the order of $10^5\,\mathrm{mW}\cdot\mathrm{cm}^{-2}$.
3. State detection and Doppler cooling. The state-detecting laser drives a closed cycling transition which is also used for Doppler-cooling the ions. We will refer to this laser source as the Blue Doppler (BD) laser.
4. State correction and sideband cooling. Erroneous state manipulations can partly be corrected using an additional resonant transition which is also used for sideband cooling. Providing similar properties as the BD laser, we will analogously call this laser source the Red Doppler (RD) laser.

Laser frequencies of the resonant transitions have to match the respective transition frequencies within a range of $\pm 1\,\mathrm{MHz}$. We use Doppler-free iodine saturation spectroscopy to adjust and/or lock the lasers to the required frequencies.

4.1. Laser sources

4.1.1. Dye laser

We generate 285 nm light required for the photo-ionisation process by second harmonic generation (SHG) of a dye laser (Coherent model 899) operated at 570 nm. The required frequency is determined roughly using a wavemeter (±500 MHz) and fine-adjusted using a Doppler-free iodine spectroscopy signal.

We use rhodamine-19 dissolved in ethylene glycol as a dye solution. For proper jet formation, the solution is cooled down to 9 ℃. Under normal conditions, i. e. when the dye has already bleached out and lost its initially high gain (this is the case after about one week), we pump the dye laser with 4 W of frequency-doubled solid state laser light (Coherent Verdi V10) at 532 nm. We are able to operate the laser using these parameters for about two months.

4.1.2. Fibre lasers

All three remaining laser systems consist of specially designed fibre laser systems (Koheras Boostik models) near 1120 nm (IR) which are frequency-doubled twice to generate wavelengths near 280 nm (UV). These fibre lasers feature very narrow linewidths of $2\pi \cdot 200$ kHz essential for coupling light into the SHG resonators (see below). As an active gain medium they use an optical waveguide doped with ytterbium. In our systems, the fibres are attached to a metal plate and have a piezoelectric transducer (PZT) at one end. The output frequency can be precisely adjusted by either tuning the metal plate temperature (on the timescale of a minute) or tuning the PZT voltage (bandwidth of 20 kHz); both mechanisms alter the fibre length. Technical specifications are summarised in tab. 4.1.

Reliable "turn-key" operation of the fibre lasers is estimated at three years, which is the lifetime of the employed pumping diodes. Whereas we would observe very stable and reliable operation during the first year, two of our three fibre laser systems failed afterwards and had to be shipped to the manufacturer for minor repair works. The BD system, which had been in use most heavily, first failed after one and a half years. It had

laser source	frequency range [THz]	max. output power [W]	temperature tuning [$\mathrm{GHz_{IR}}$/℃]	PZT tuning [$\mathrm{MHz_{IR}}$/V]
Raman	267.98 – 268.10	1.90	2.3	+670
BD	267.97 – 268.08	0.90	2.7	−17
RD	267.28 – 267.39	1.27	2.8	+17

Table 4.1.: Technical specifications of the used fibre laser sources.

to be repaired twice which decreased stable output power from 1.44 W to 0.90 W. In one case, a wavelength division multiplexer (WDM) broke, in the other case a pumping diode failed. However, this system is supposed to regain the initial performance after an upgrade of its pre-amplifier section. The RD system broke after two years, the reason was a bleached beamsplitter. We stress that we did not run the fibre lasers continuously but rather for a maximum of twelve hours per day.

The fibre laser driven UV sources will drive coherent transitions between different energy levels of magnesium. As fluctuations in phase or amplitude will diminish the fidelity of these transitions, they should be kept at a minimum. Concerning the stability of the intensity after the two SHG stages (see below) we observe 4% drops in amplitude on a microsecond timescale, and 7% drops less than once a minute [16], which could hardly be achieved using conventional dye laser setups.

4.2. Second harmonic generation

For second harmonic generation (SHG) we use resonators designed as bow-tie cavities with sputtered mirrors featuring reflectivities of 99.98% [16]. The length of these resonators is actively stabilised using a mirror mounted onto a piezoelectric crystal (PZT) in combination with the locking technique of Hänsch and Couillaud [34]. We will distinguish two different types of second harmonic generation:

1. *SHG of visible green light from infrared (IR) light.* IR light from one of our fibre laser systems first passes an optical isolator (transmittivity ≈ 90%, isolation ≈ 30 dB) which prevents damage of the fibre lasers by back reflection. Subsequently, it is coupled into the SHG resonator using a modematching telescope. The IR light is frequency-doubled with the help of a lithium triborate (LBO) crystal cut at 90° angles and antireflectance coated for both the fundamental and harmonic wavelengths. Non-critical type I phase matching is achieved using a crystal oven temperature of 94 °C. The folding angle of the resonator is kept small (10°) to minimise astigmatism of the fundamental wave. In the end this system yields a maximum conversion efficiency of 52.7%.

   For about two hours after the fibre laser systems have been powered up, their IR polarisation will drift, which causes the frequency-doubled output power to vary. After two hours, we can still observe polarisation drifts, but these are caused by changes in the ambient temperature (power alterations of 5% per 1 K *behind* the

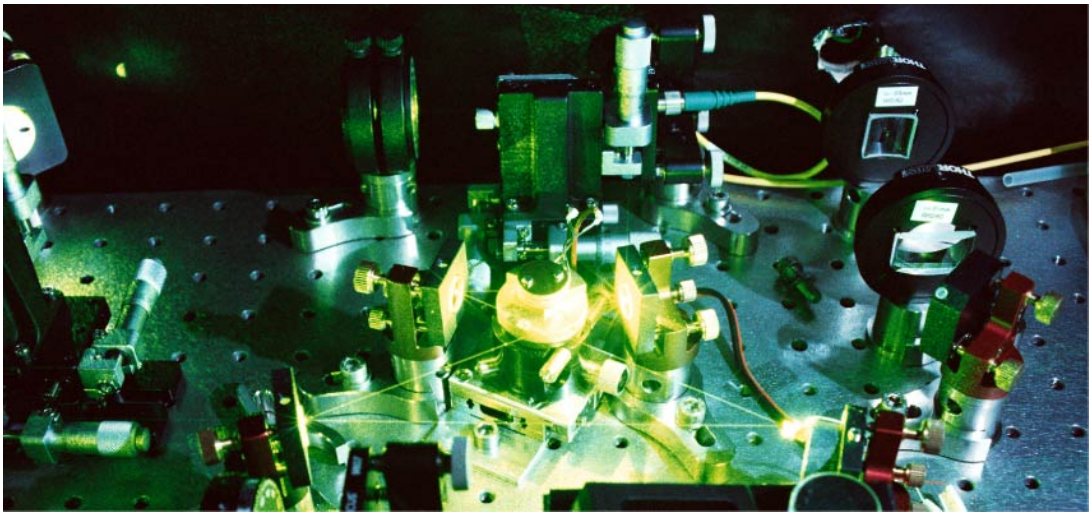

Figure 4.1.: BBO resonator for frequency-doubling our dye laser source. The input coupler and the attached optical fibre can be seen in the background. At the bottom left part of the resonator a small mirror mounted on a PZT element keeps the resonator's optical length constant. On the right hand side one can see the cylindrical telescope used for correcting the astigmatism of the output beam.

resonator). We reduce these effects by stabilising the temperature of the fibre lasers' Peltier elements.

2. *SHG of ultraviolet (UV) light from visible green light.* UV light is eventually generated using a second SHG resonator with a beta barium borate (BBO) crystal using critical type I phase matching. Due to reported problems with the adhesion of antireflectance coatings on BBO at high intensities we have had the front and back sides of our crystals cut at Brewster's angles instead. The thereby induced astigmatism of the fundamental wave after one "run" through the resonator is compensated by choosing an appropriate folding angle of the resonator (27.4°). In order to prevent water from condensing on the hygroscopic surface we permanently heat the crystal to 50 °C and expose it to a flow of oxygen. Walkoff of the harmonic wave inside the crystal results in an astigmatic output beam which is corrected, i. e. projected into a proper TEM_{00} mode, using a cylindrical telescope. We obtained conversion efficiencies of up to 28.9% (mostly due to losses of the s-polarised harmonic wave exiting the Brewster-cut crystal).

In the Raman and BD systems, we directly couple light emitted from the first SHG stage into the second one. Both stages reside on a common breadboard enhancing portability. The RD system is spatially split: Output of the LBO resonator is fed into the BBO resonator using a single-mode optical waveguide. Whereas the first scheme provides high effective conversion efficiencies, it can be quite subtle to re-adjust both SHG resonators without touching alignment of the output UV beam. The second scheme does not feature maximum conversion efficiencies due to losses at the waveguide's incoupler (we achieve incoupling efficiencies about 85%), but it can more easily be re-adjusted. In addition, it is more flexible as we can couple light from other laser sources at 560 nm (such as a dye laser) into the BBO cavity without many efforts—which is very handy should one fibre laser system fail. We actually do use such a system for generating the beam required for photo-ionisation, see section 4.3.1.

4.3. Beamlines

An overview of the beamline setup is given in fig. 4.2. All initial beams (upper part of the figure) leave their respective SHG resonators with s-polarisation, i. e. their electric field vector is perpendicular to the optical table surface. For our first experiments we will consider the following beams:

- Photo-ionising beam at 285 nm. It enters the chamber exclusively via port L (the upper port, M is the lower port).
- BD and BD detuned beams. Using the $\lambda/2$ waveplate in combination with the polarising beam splitter PBS_2 their power can be directed either towards port L (p-polarised) or towards port H (σ^+-polarised due to the $\lambda/4$ waveplate in front of port H) or a combination of both.
- RD and repumper beams. They are superposed on the BD and BD detuned beams at the non-polarising beam splitter NPBS which retains the s-polarisation of all beams. Therefore, they also enter the chamber σ^+-polarised via port H.
- Raman beam B1. It is p-polarised using a $\lambda/2$ waveplate and enters the chamber via port G. Therefore, it is π-polarised with respect to the magnetic field axis.
- Raman beam R1. R1 is superposed on B1 at the polarising beam splitter PBS_1, thus also directed towards port G.

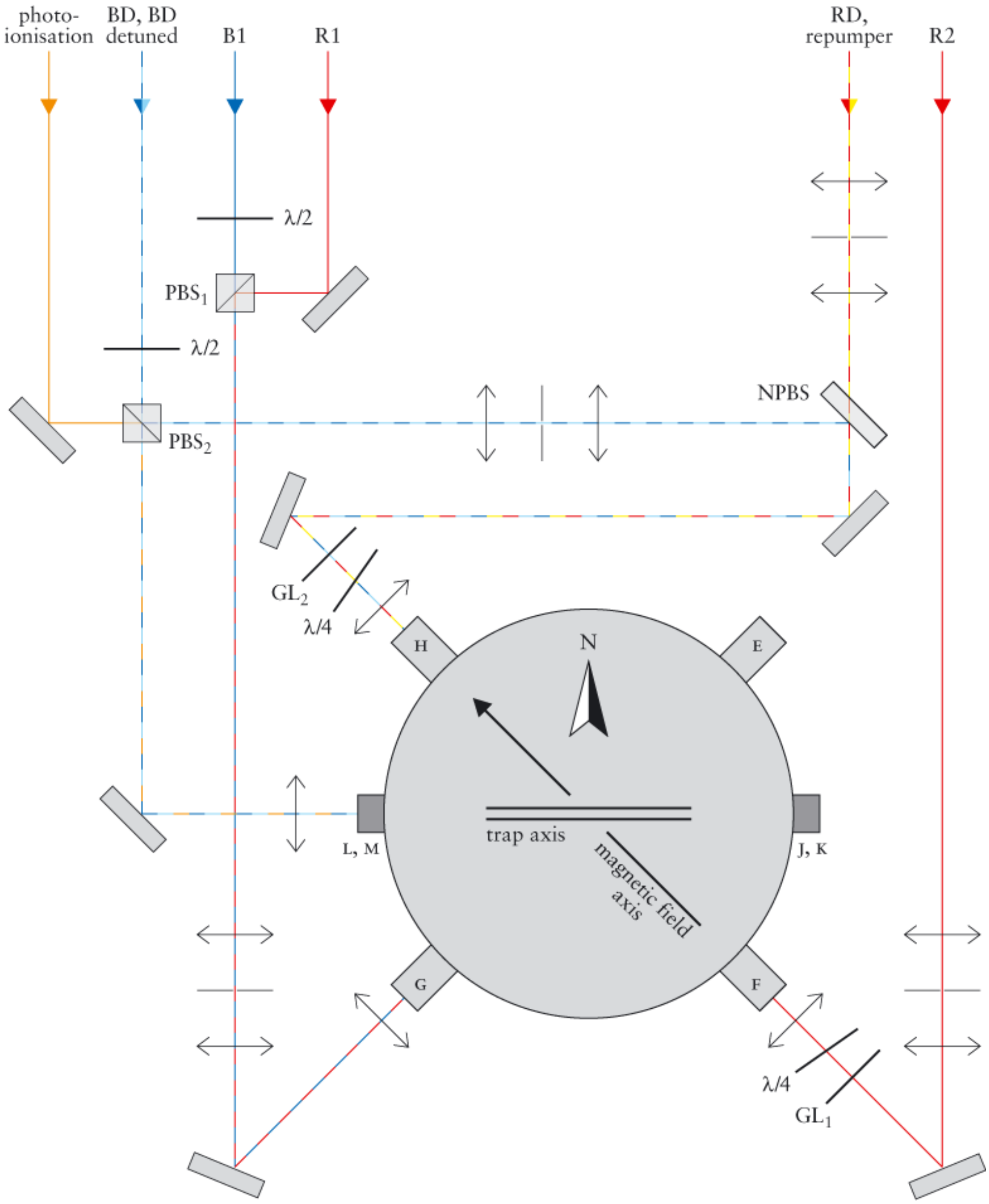
photo-
ionisation
BD, BD
detuned
B1
R1
RD,
repumper
R2
λ/2
PBS$_1$
λ/2
NPBS
PBS$_2$
GL$_2$
λ/4
H
N
E
L, M
trap axis
magnetic field
axis
J, K
G
F
λ/4
GL$_1$

Figure 4.2.: Beamline setup used for experimentation. All input beams (upper part of the figure) are s-polarised. Legend: PBS = polarising beam splitter, NPBS =non-polarising beam splitter, GL_i = Glan Laser polariser.

- Raman beam R2. It is σ^--polarised by the $\lambda/4$ waveplate in front of port F. However, in the framework of the magnetic field axis, it is σ^+-polarised.

Note the deviation from the perfect 90° angle for the $\lambda/4$ waveplates. Although specified for 280 nm—the wavelength used for all the beams passing through—these waveplates have to be inclined in order to maximise their efficiency*.

The combination of beams entering the chamber via port L is used for photo-ionising magnesium atoms and loading the respective ions into the trap. It thus points to the centre of the loading region. All other beams are focused into the centre of the experimentation region.

All beams entering the chamber are focused by a "final" lens (focal length $f = 200\,\text{mm}$) so that the focal point lies in the middle of the trap volume. That way intensity as well as spatial resolution is increased while scattered light causing an increased background signal is reduced at the same time. Furthermore, we use these lenses to position the respective beams inside the trap volume with an accuracy of $\pm 3\,\mu\text{m}$.

Wherever possible, we "housed" the beams with transparent tubes so as to minimise beam steering and phase fluctuation effects caused by fluctuations (either temporal or spatial) of the air's refractive index. Such fluctuations are normally omnipresent in the lab: Various thermal sources will heat the air in their vicinity thus causing air turbulences. The same is true for people passing by close to the optical tables: They will generate wake vortices of the air behind them. The transparent housings protect the air inside from these fluctuations introduced from the outside.

In order to further still the air on the optical tables, we house the complete optical apparatus with flow boxes on the top and transparent windows at the sides. The flow boxes will provide a laminar flow of dust-filtered air as well as a slight overpressure inside the housing. Dust particles still inside the housing should be swept outside that way.

4.3.1. Photo-ionising beam

570 nm light from our dye laser system is coupled into the respective resonator by means of an optical waveguide. We attain waveguide coupling efficiencies, i. e. optical power after the waveguide in relation to the power before the waveguide, of around

---

[*] Tolerances of 5° lie within the specifications of the manufacturer (B. Halle, Berlin)

operating power	0.5 mW – 2.0 mW
waist at trap centre	$\sim$ 70 µm
frequency ($^{24}\mathrm{Mg} \rightarrow {}^{24}\mathrm{Mg}^+$)	$1.050810699 \cdot 10^{15}$ Hz
frequency ($^{25}\mathrm{Mg} \rightarrow {}^{25}\mathrm{Mg}^+$)	$1.050811443 \cdot 10^{15}$ Hz

Table 4.2.: Characteristics of the photo-ionising laser beam.

85%. There are no switching elements in the beamline—we simply block the photo-ionising beam by means of a beamdump once enough ions have been loaded. Tab. 4.2 lists the relevant beam parameters.

4.3.2. Raman beams

The Raman beam setup is shown in fig. 4.3. From an initial 325 mW UV beam, we generate three individual beams that can be switched on and off and controlled with respect to their frequency, phase and amplitude using acousto-optical modulators (AOMs): A blueshifted B1 beam, and two redshifted beams named R1 and R2. The frequency difference between the blueshifted and redshifted beams can be precisely adjusted using the driver frequency of the Raman blueshifter. This is actually not an acousto-optical modulator (AOM) but an acousto-optical *deflector* featuring constant deflection efficiencies (±5%) over a wide range of driving frequencies (200 MHz – 240 MHz). With the other AOMs operating at 220 MHz we can thus tune the frequency difference between 1720 MHz and 1800 MHz. The driving powers for the B1, R1 and R2 AOMs determine their diffraction efficiencies and thus optical powers of the respective beams which can be varied from 0% to about 85% of the initial optical power. The $\lambda/2$ plate

Raman beam	max. power [mW]	waist at trap centre [µm]
B1	1.2	33
R1	48	35
R2	48	35

Table 4.3.: Raman beam parameters.

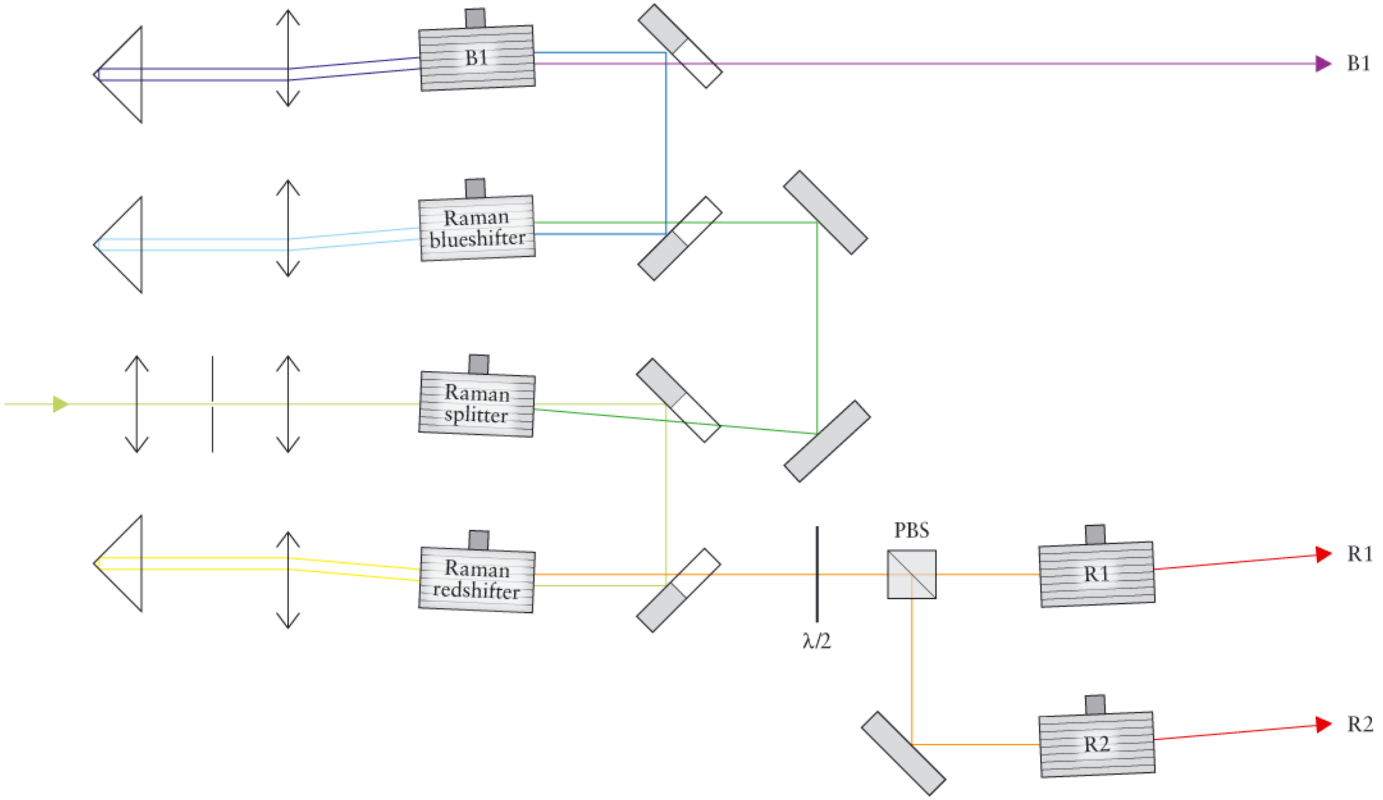

B1
Raman
blueshifter
Raman
splitter
Raman
redshifter
B1
R1
R2
PBS
λ/2
R1
R2

Figure 4.3.: Setup used to generate the three Raman beams. Legend: PBS = polarising beam splitter. Note that the beam offsets induced by the double-pass prisms actually occur in the vertical direction (perpendicular to the drawing plane). This avoids a parallel offset when an AOM's frequency is altered.

is used to additionally adjust the relative intensities of the R1 and R2 before starting experimentation.

Tab. 4.3 contains a summary of the utilised beam parameters. For our experiments, only the frequency difference of B1 and R1 / R2 matters. As in addition all Raman beams couple to a virtual level, which is blue-detuned by at least 80 GHz with respect to the $3P_{3/2}$ level, frequency drifts of ±20 MHz induced by changes of the ambient temperature (±2 ℃) remain negligible.

Although the beam waists are small compared to the dimensions of our ion trap, we do observe a considerable amount of stray light when the beams shine into the trap volume with many milliwatts of power. However, these beams will not be enabled during detection; thus contrast of our measurements is not affected.

4.3.3. Blue Doppler beams

The BD beam is detuned by half the linewidth ($\Delta = \Gamma/2$) of the BD transition and attenuated to an intensity of $I = (2/3)I_{\text{sat}}$ in order to maximise the Doppler cooling efficiency. As such, it would actually suffice in order to Doppler cool the ions and conduct detection in quantum simulation experiments. However, due to collision processes with the residual gas in the vacuum chamber ions stored in the trap will from time to time gain so much velocity that the BD beam alone will not be able to re-cool them on a millisecond timescale before the start of each experiment. This is where the detuned Blue Doppler beam (BD detuned) comes into play. With a frequency that is redshifted 660 MHz with respect to the BD frequency and an intensity of $I \approx 6I_{\text{sat}}$, it will even cool hotter ions (see tab. 4.4).

Fig. 4.4 shows the setup for the two Blue Doppler beams. They are created from an initial 90 mW of UV beam power. Note that lens L_2 is necessary to re-collimate the

BD beam	max. power [mW]	operating power [µW]	waist at trap centre [µm]	frequency [10^{15} Hz]
BD	2.0	5.5	47	1.072085218
BD detuned	2.0	100	47	1.072084558

Table 4.4.: BD beam parameters calibrated for $^{25}\text{Mg}^{+}$.

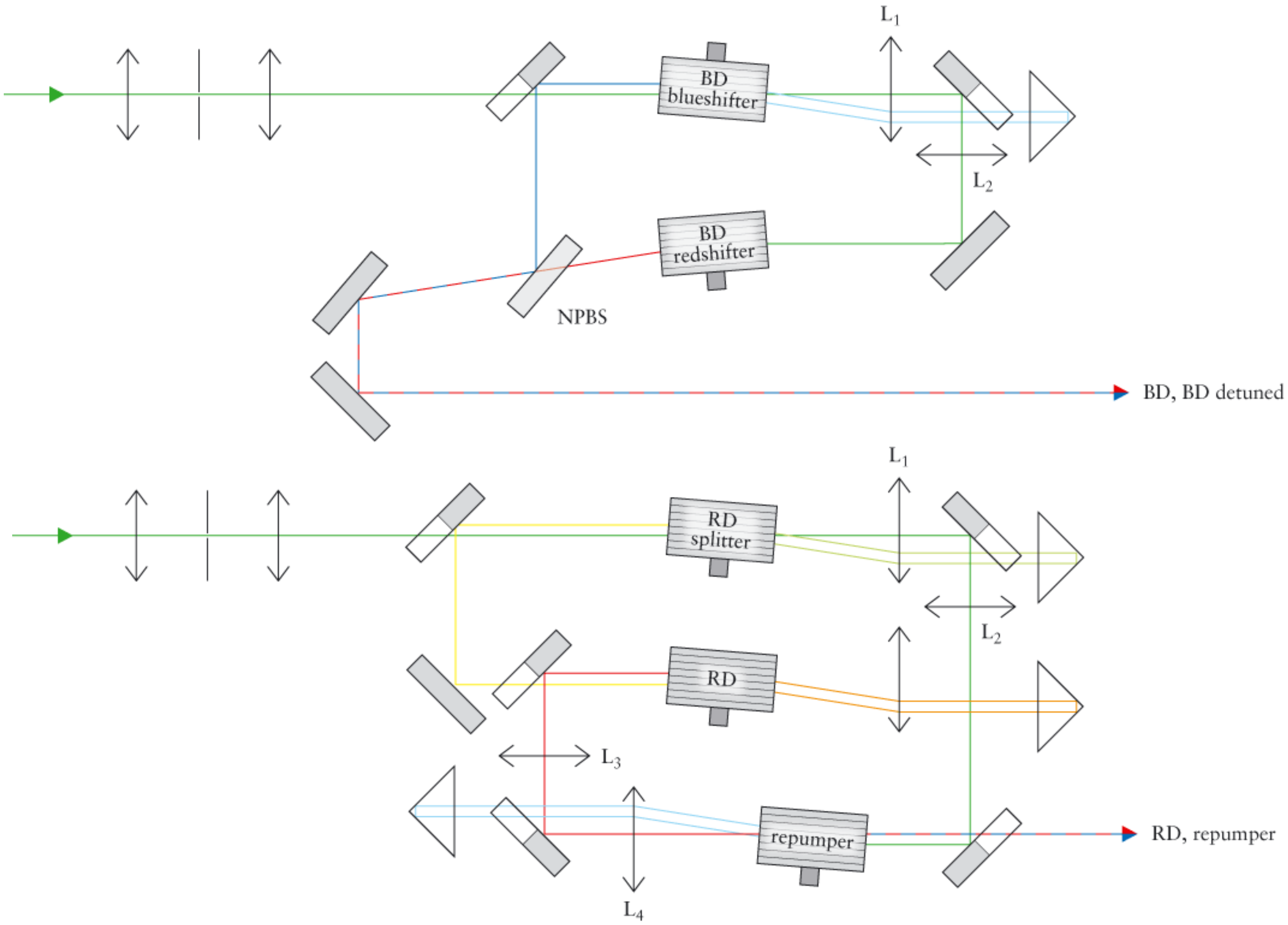
L$_1$
BD blueshifter
L$_2$
BD redshifter
NPBS
BD, BD detuned
L$_1$
RD splitter
L$_2$
RD
L$_3$
repumper
RD, repumper
L$_4$

Figure 4.4.: Setups used to generate the two Blue Doppler and the two Red Doppler beams. Legend: NPBS = non-polarising beam splitter. Note that the beam offsets induced by the double-pass prisms actually occur in the vertical direction (perpendicular to the drawing plane). This avoids a parallel offset when an AOM's frequency is altered.

RD beam	max. power [mW]	operating power [µW]	waist at trap centre [µm]	frequency [10^{15} Hz]
RD	1.2	5	45	1.069338736
repumper	1.2	5	78	1.069340525

Table 4.5.: RD beam parameters calibrated for ^{25}Mg^{+}.

undeflected beam, as it passes through lens L_1 only once. In practice, the undeflected beam's waist can be adjusted by altering the focal length ratio of L_1 and L_2.

The AOMs introduce a frequency difference of 660 MHz between the two generated beams. We also use the BD and BD detuned AOMs to switch the respective beams on and off during experimentation. By manually tuning variable RF attenuators in the AOM driving circuits we can adjust the optical powers of the two beams. It is sufficient to conduct these adjustments once before experimentation starts.

4.3.4. Red Doppler beams

The Red Doppler beam generation setup is shown in fig. 4.4. We generate a redshifted Red Doppler (RD) and a blueshifted repumper beam, separated by a frequency difference of 1789 MHz. Note that the repumper AOM is operated at 454 MHz to achieve this. Initial UV beam power is 90 mW. In analogy to the BD setup, we use two re-collimating lenses L_2 and L_3 to correct for the non-doublepassed beams.

Both the RD and repumper beams can be switched on and off using the respective AOMs. As in the case of the BD setup, we adjust their optical powers once before starting an experiment using manual variable attenuators.

4.4. Doppler-free iodine spectroscopy

Whereas we can measure a laser's wavelength using a wavemeter (accuracies of 10^{-7} – 10^{-8}) we still have to determine—and in some cases lock—the frequency of our laser systems with a resolution of ±1 MHz. This is achieved using Doppler-free iodine spectroscopy. Transition lines of iodine are well-known [35] and can be calculated to a high

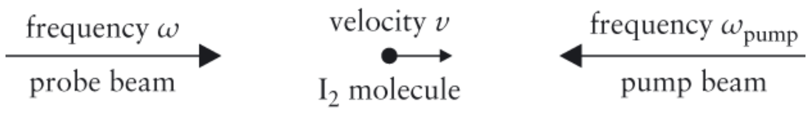

Figure 4.5.: Schematic of Doppler-free iodine spectroscopy.

precision using additional data on hyperfine splittings, which makes them ideal for use as a frequency standard. We use Toptica's IodineSpec[†] for this purpose.

We use saturation spectroscopy in conjunction with a signal-enhancing lock-in amplifier whose modulation signal drives an AOM [36]. Other spectroscopic techniques are available, e. g. polarisation spectroscopy [37, 38] which may reduce the experimental effort for some purposes. In our setup however, an AOM is necessary anyway to provide the required frequency shifts, which is why we stick with saturation spectroscopy.

4.4.1. Principles of Doppler-free saturation spectroscopy

The simplest method of saturation spectroscopy uses two beams, one reference beam that freely propagates (through vacuum or air) and a probe beam which passes through the material and is attenuated on its way according to eq. (1.14) where $i = 1$ and $I_{\text{total}} = I_1$. Subtraction of the respective intensities will yield a measure of the transition strength, i. e. of how efficiently the transition could be driven. As a function of the beams' frequency this will give a spectroscopic signal.

If the optical medium used for spectroscopic measurements is a gas (as is the case with iodine), linewidths of the optical transitions will be considerably Doppler-broadened ($\sim 1\,\text{GHz}$) at room temperatures decreasing the frequency resolution. Doppler-free spectroscopy overcomes this limitation by employing three beams in total:

1. the reference beam (frequency ω, intensity I) which freely propagates through the iodine cell,
2. the probe beam (frequency ω, intensity I as well) which also propagates through the iodine cell, most commonly parallel to the reference beam, but is superimposed by
3. the couterpropagating pump beam (frequency ω_{pump}, intensity I_{pump}). This one features a very strong intensity suited to optically bleach the medium.

[†] http://www.toptica.com/

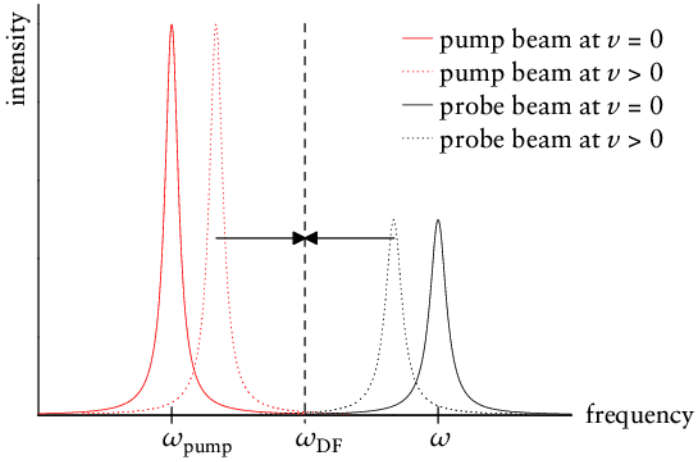

Figure 4.6.: Intensity profiles as seen by an iodine molecule. Solid curves: $v = 0$. Dotted curves: $v > 0$.

This setup is illustrated in figs. 4.5 and 4.6. An iodine molecule moving with velocity v is hit by the probe beam and the pump beam from opposite directions. If the molecule were at rest, it would "see" a probe beam frequency of ω and a pump beam frequency of ω_{pump}. Now that the molecule is moving at velocity v, the probe beam frequency is redshifted in the frame of the molecule (dotted curve in fig. 4.6). Analogously, the pump beam frequency appears blueshifted. At some particular velocity v_{DF}, associated with the frequency ω_{DF}, the intensity profiles of probe and pump beams overlap. Only then will the pump beam "talk" to the same velocity class of molecules as the probe beam. If in addition ω_{DF} happens to be the frequency of an iodine transition, attenuation of the probe beam will be decreased according to eq. (1.14). In other words: A decrease in the attenuation of the probe beam will only occur for a special velocity class of molecules; thus Doppler broadening is circumvented. As attenuation of the (unpumped) reference beam is never decreased, we will observe a non-zero difference in the intensities of the probe and reference beams if ω_{DF} matches the frequency of an iodine transition.

As indicated in fig. 4.6 ω_{DF} lies in the middle between ω and ω_{pump}:

$$\omega_{\text{DF}} = \frac{\omega + \omega_{\text{pump}}}{2}. \tag{4.1}$$

This is because as a first approximation the blue Doppler shift of the probe beam equals the red Doppler shift of the pump beam.

4.4.2. Experimental setup

The experimental setup for iodine spectroscopising the once frequency-doubled BD laser (at 560 nm) is shown in fig. 4.7. We operate AOM_1 at a frequency of 210.5 MHz and AOM_2 at 80 MHz. Probe and reference beams are coloured green, the pump beam is painted red. In the end, both the probe and the reference beam hit a differential photodetector (Newport Nirvana) which subtracts the individually measured powers from each other. This type of photodetector has one additional feature that greatly facilitates operation: Low-frequency differences in the two signals are automatically evened out. So even if powers in the two beams differ by some DC offset, the detector output signal is still zero.

The output signal of the photodetector is in general too weak to be used directly. Furthermore, it has to be differentiated so as to provide a zero-crossing which we use for locking (see below). We achieve both these aims by phase-sensitive lock-in techniques. For this purpose, we wobble the driving frequency of AOM_2—and thus the pump beam frequency—with 10 kHz. The lock-in amplifier will phase-sensitively filter the amplitude of a 10 kHz modulation in the photodetected signal thereby enhancing the signal-to-noise ratio by several magnitudes.

Wobbling the pump beam frequency and thus ω_{DF} corresponds to a wiggle on the horizontal axis of fig. 4.6. As long as the centre frequency $\langle\omega_{\mathrm{DF}}\rangle$ lies at the rising edge of an iodine transition line, the Nirvana photodetector will accordingly measure a 10 kHz modulation of the incoming probe intensity, which causes the lock-in amplifier to output a negative voltage. If the centre frequency lies at the falling edge, the intensity modulation of the probe beam is phase-shifted by π, which causes the lock-in amplifier to output a positive voltage. In between, when $\langle\omega_{\mathrm{DF}}\rangle$ exactly matches the transition frequency, the lock-in amplifier will output a voltage of zero. An image of the curves obtained that way is shown in fig. 4.8.

The iodine spectroscopy setups attached to the dye laser and the RD laser are in principle equal to that of the BD laser. They differ in their particular setup of AOMs: Firstly, they both lack an initial frequency shifter AOM_1. Secondly, AOM_2 in the dye laser iodine setup modulates both the pump and probe beams thereby causing a Doppler free spectroscopic frequency that is shifted by 160 GHz instead of only 80 GHz. In the RD setup AOM_2 shifts to bluer frequencies by 91 MHz.

The dispersive spectroscopic signal can be used to comfortably lock the laser to one of the signal's zero-crossings, i. e. one of the iodine transition frequencies. The

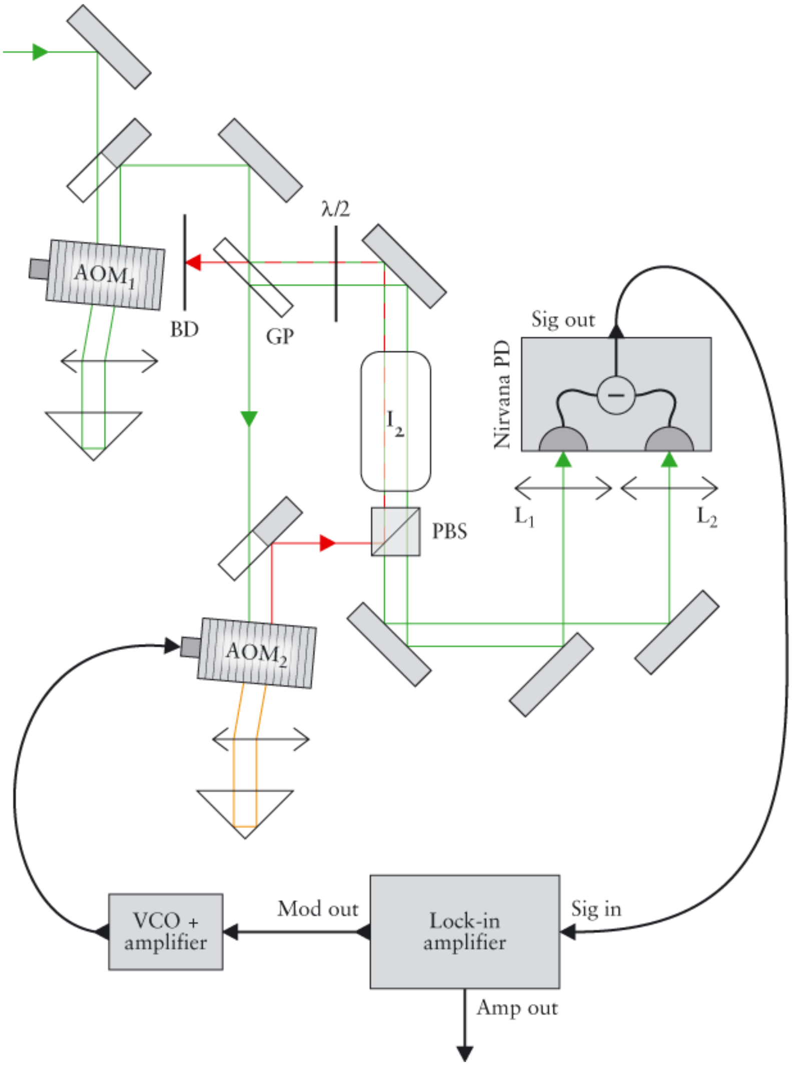
λ/2
AOM$_1$
BD
GP
I_2
Sig out
Nirvana PD
PBS
L_1
L_2
AOM$_2$
VCO + amplifier
Mod out
Lock-in amplifier
Sig in
Amp out

Figure 4.7.: Doppler-free iodine saturation spectroscopy setup. Legend: AOM$_i$ = acousto-optic modulator, GP = glass plate, PBS = polarising beam splitter, BD = beam dump, VCO = voltage-controlled oscillator. Note that the beam offsets induced by the double-pass prisms actually occur in the vertical direction (perpendicular to the drawing plane). This avoids a parallel offset when an AOM's frequency is altered.

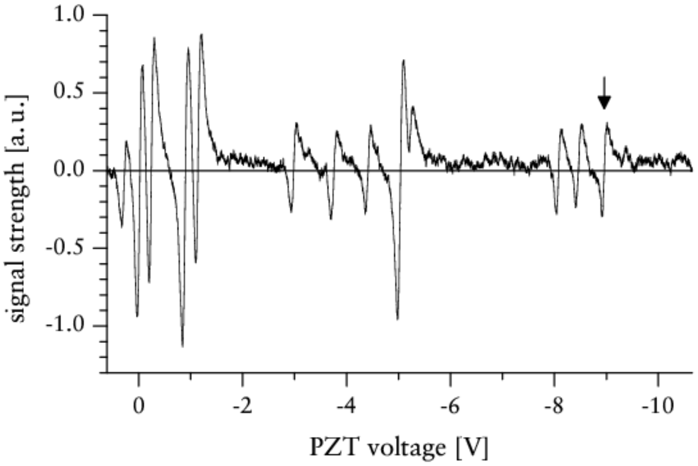

Figure 4.8.: Doppler-free iodine spectroscopic signal obtained from the BD laser after the first SHG stage. The signal has been averaged over four acquisitions with an initial beam power of 5.2 mW. The arrow indicates the line that the laser is locked to. Note that the small overall positive offset ensures that the laser will run to redder frequencies in case the lock is lost. That way, heating the ions is prevented.

feedback loop of such a regulation simply consists of an op-amp adder circuit (to be able to roughly adjust the frequency) combined with an op-amp integrator circuit (to adjust the regulation feedback speed). If the signal is below zero (left handside of a zero-crossing), the laser's frequency is increased and vice versa, thus locking the laser to the specific iodine transition.

During experimentation we iodine-lock the BD and RD lasers. The dye laser feeding the photo-ionisation SHG stage also has an iodine apparatus attached which we use to adjust its frequency. We do however not lock to this signal as frequency requirements for the photo-ionisation process are not as strict as for the BD or RD beams. Tab. 4.6 gives an overview over the parameters used.

Using the iodine multiplet between 536.041859 THz and 536.041888 THz we can lock the BD laser to frequencies between 536.042299 THz and 536.042408 THz by appropriately adjusting the AOM_1 shift. As can be seen in fig. 4.7, only the pump beam is frequency-shifted twice. Eq. (4.1) shows that we could span a greater frequency range for the laser lock if the probe/reference beams were frequency-shifted as well, i. e. if the they also passed through AOM_2. We however observed a *permanent* 10 kHz signature of the probe beam for this setup, leading to an overall offset in the lock-in amplifier output which prevented locking due to the lack of proper zero-crossings. We assume

laser source	initial beam power [mW]	iodine frequency [THz]	signal/noise ratio
BD	5.2	536.041888	1.75 : 1
RD	12.0	534.669899	100 : 1
dye laser adjusted for ^{24}Mg^{+}	7.9	525.405609	10 : 1
dye laser adjusted for ^{25}Mg^{+}	7.9	525.405757	10 : 1

Table 4.6.: Parameters used for the iodine spectroscopy setups throughout experimentation. Unless noted otherwise, frequencies are calibrated for ^{25}Mg^{+}. Iodine frequencies were extracted from Toptica's IodineSpec. The discrepancy between the dye laser's iodine frequencies listed here and the frequencies listed in tab. 4.2 is due to the Doppler-shift of the not yet ionised magnesium atoms, see section 3.3.

that wobbling the frequency of AOM$_2$ introduced some steering between the probe and the pump beams. The frequency range spanned by the setup illustrated in fig. 4.7 will however suffice for our applications.

5. Visualisation and data acquisition

The last step of every quantum simulation experiment is reading out the final qubit state. We have to determine whether the ion in question is bright (fluoresces) or dark when we shine onto it using the BD laser beam.

5.1. Optics

All detection equipment uses the vacuum chamber's port A, which is closed by a coated sapphire crystal window. It is required by the attached objective for optimum imaging quality. At 280 nm it transmits about 99% of the incident intensity.

We use a specially designed high-quality F/1 objective (aperture angle 55.6°, focal length 19.3 mm) with a magnification factor of 50 (B. Halle, Berlin). That way, we should be able to resolve ion-to-ion distances of down to 0.35 µm (see fig. 5.1). Actually resolvable ion-to-ion distances depend on the focal setting of the objective, we achieved a minimum of 2 µm, see fig. 5.2.

Fluorescing magnesium ions will emit $\sigma^{\pm}$ polarised light in the cycling BD transition, see section 2.3. The emission characteristics is determined by

$$P(\theta, \phi) = 1 + \cos^2(\theta) \tag{5.1}$$

where θ and ϕ are the angles of spherical coordinates. $\theta = 0$ equals the direction of the applied magnetic quantisation axis so that the direction towards the detection port A of our chamber is given by $\theta = \pi/2$ (see fig. 4.2). Our objective thus catches 4.7% of the photons scattered. From this point of view it would have been advantageous to observe the ions at an angle θ close to zero. However, such a setup would block the horizontal laser beams intersecting the trap axis under 45°.

After having passed through the objective the beams are reflected on a 45° mirror with a reflectivity of 99% and enter a box with our detection instruments—a CCD camera and a photomultiplier (PMT). By means of a motor-driven flip mirror

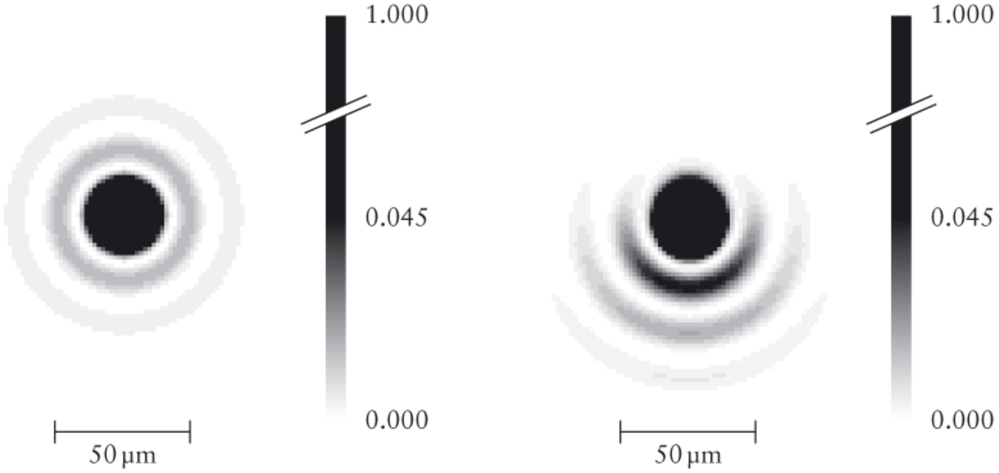

(a) Ion centred below objective.

(b) Ion off by 50 µm from central position.

Figure 5.1.: Image of a point-like fluorescing ion as it appears at the magnifying end of the objective. What is actually drawn here are the point spread functions (PSF) of the objective calculated using the software package ZEMAX. The image contrast has been greatly increased—all values above 0.045 are represented by black colour.

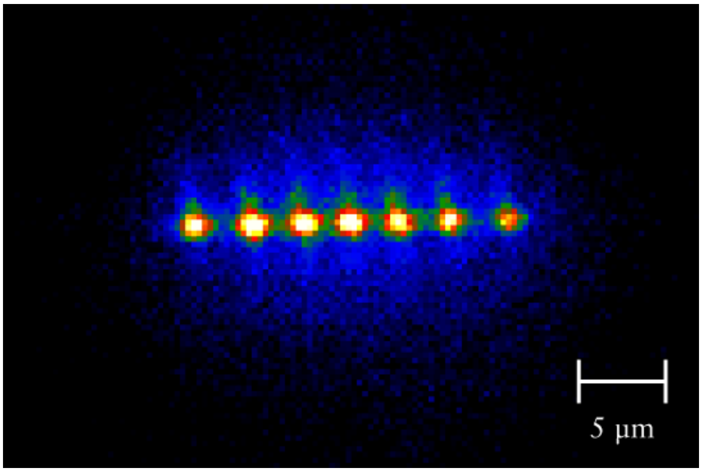

Figure 5.2.: Image of a chain of seven ions at an axial confinement of $\approx 2\pi \cdot 2\,\mathrm{MHz}$. The spatial resolution for one ion can be estimated at 2 µm.

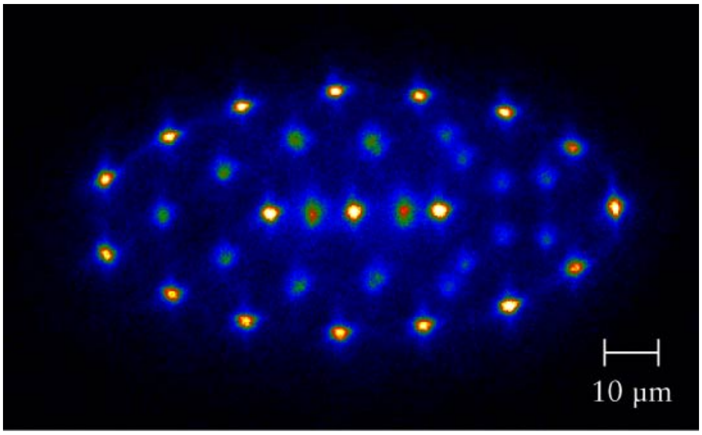

Figure 5.3.: Cigar-shaped Coulomb crystal of approx. 40 ions. The great ion-to-ion distances are due to a relatively weak radial confinements ($\omega_{\text{radial}} \approx 2\pi \cdot 1\,\text{MHz}$, $\omega_{\text{axial}} \approx 2\pi \cdot 100\,\text{kHz}$.

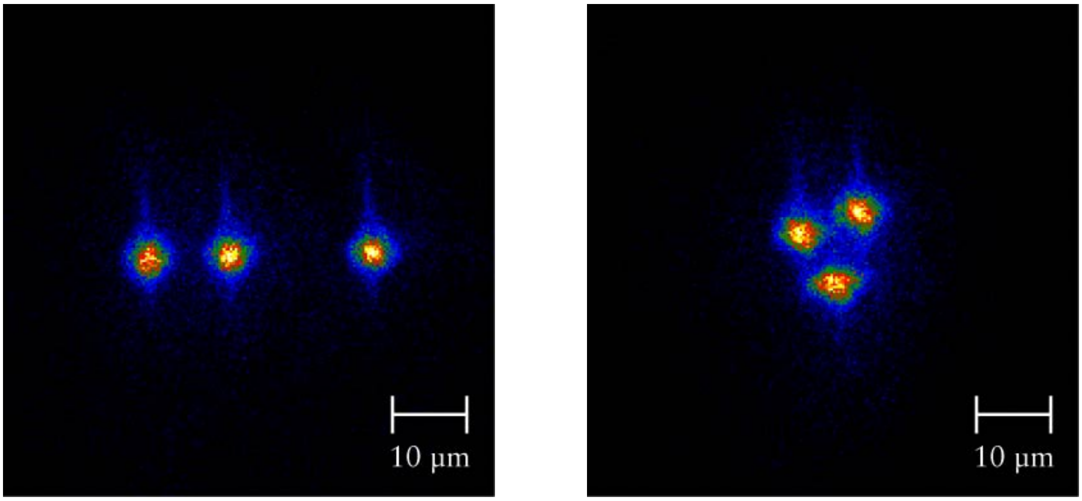

(a) $\omega_{\text{axial}} < \omega_{\text{radial}}$.

(b) $\omega_{\text{axial}} > \omega_{\text{radial}}$.

Figure 5.4.: Coulomb crystal of four ions including one "dark" ion, which is most probably magnesium hydride MgH^+ (resulting from a collision of the magnesium ion with hydrogen from the residual gas).

fluorescent scattering rate	33.8 MHz
objective captures 4.7%	$\rightsquigarrow$ 1.59 MHz
14% of optical losses	$\rightsquigarrow$ 1.37 MHz

Table 5.1.: Calculation of the expected count rate behind all optics. The fluorescent scattering rate was calculated using eq. (1.6) for a detuning of $\Delta = \Gamma/2 = 21.5\,\mathrm{MHz}$ and an intensity of $I = (2/3)I_{\mathrm{sat}} = 167\,\mathrm{mW} \cdot \mathrm{cm}^{-2}$ which equals a Rabi frequency of $\Omega = \Gamma/\sqrt{3}$. These parameters for the BD detection laser are used throughout during experimentation.

(reflectivity > 99%) we can direct the light either onto the camera or onto the photomultiplier. See fig. 5.5 for the assembly of the detection box. The whole beamline between the objective and our detection instruments is shielded against ambient light sources by either non-transparent metal housings or—in the case of the detection box—by laser safety curtain wrappings.

Both the camera and the PMT are equipped with glass filters (Schott UG5, thickness 2 mm) opaque at visible wavelengths but transparent (transmission 88%) at 280 nm. Altogether we must consider photon losses of the order of 14% on the way from the ions to our detection instruments. Tab. 5.1 estimates the expected photon count rate.

5.2. PMT

The most straightforward way of precisely measuring weak light sources is to use a photomultiplier PMT. We use a Hamamatsu H8259 with a quantum efficiency of about 14% at 280 nm and a pulse-pair resolution of 35 ns. Its photoactive window has a size of $4 \times 20\,\mathrm{mm}$. As we want to make sure that only a minimal amount of stray light hits the PMT, we have placed a manual variable slit aperture in front of it. In order to prevent saturation of particular regions on the photoactive window, we defocus the ions' image thus distributing the intensity over a greater region. Using standard operating intensities for the BD detection beam (see tab. 4.4) we get count rates of 210 kHz at a signal / background ratio of about 1000 : 1. Taking into account the PMT's quantum efficiency this result fits the expected count rates (tab. 5.1). Normally we would use an “exposure time”, i. e. the timespan that we count the PMT clicks, of 20 µs to 50 µs, acquiring between 4 and 10 photons on average.

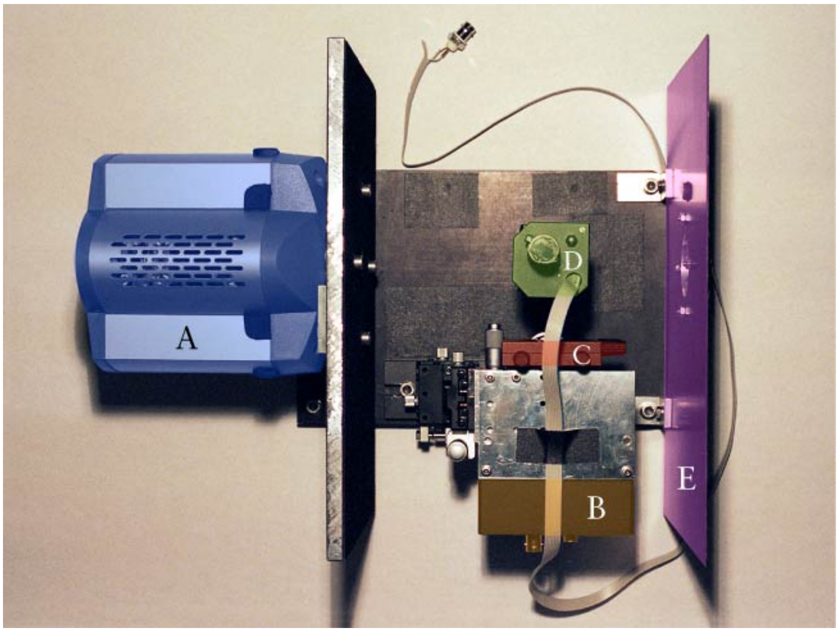

(a) Top view.

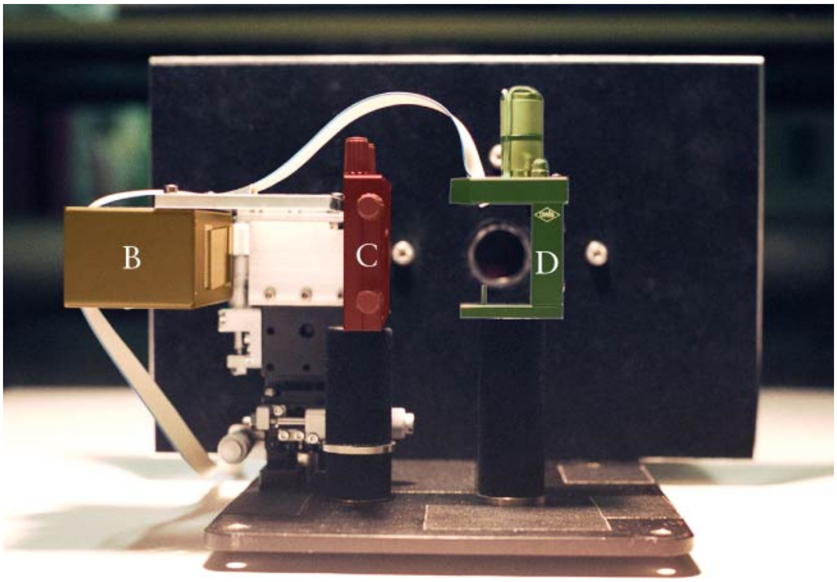

(b) Front view.

Figure 5.5.: Assembly of the detection box consisting of camera (A), photomultiplier (B), slit aperture (C), flip mirror (D), and entrance aperture (E). All parts have been highlighted with distinct colours. The photomultiplier is mounted on a linear translation stage for optimum positioning.

horizontal readout speed	5 MHz
vertical shift speed	0.4 µs
vertical shift amplitude	+2
EMCCD gain	650
pre-amplifier gain	2.4
frame transfer mode	*off*

Table 5.2.: Camera readout parameters used during experimentation.

5.3. CCD camera

Using the CCD camera as a detection instrument is a more sophisticated way of observing stored ions as it allows to distinguish single ions from each other. Our Andor iXon DV887DCS-UVB has a photoactive window of 8 × 8 mm which is very handy during the ion loading process and allows for judgements on imaging quality. The CCD is equipped with an on-chip electron multiplication facility (which is why the chip is also called an EMCCD chip) that can increase the signal generated by the released photoelectrons by a factor up to 850, depending on the actual readout settings. Relevant readout parameters that we normally use during experimentation are listed in tab. 5.2. With a nominal quantum efficiency of 34% at 280 nm the CCD is supposed to be more sensitive than the PMT. Tab. 5.3 gives an estimation of the expected camera count rate. In reality, the noise introduced by readout or thermal effects might limit the sensitivity of the CCD chip [39]. We thus measured the signal of a single fluorescing ion

count rate before the camera (tab. 5.1)	1.37 MHz
8% losses through uncoated entrance window	⇝ 1.26 MHz
quantum efficiency of 34%	⇝ 427 kHz
EMCCD gain of 650	⇝ 278 MHz
23 electrons per count (estimated)	⇝ 12.1 MHz
ion's image encompasses 20 pixels	⇝ 603 kHz/pixel

Table 5.3.: Camera count rate to be expected in theory for the parameters listed in tab. 5.2.

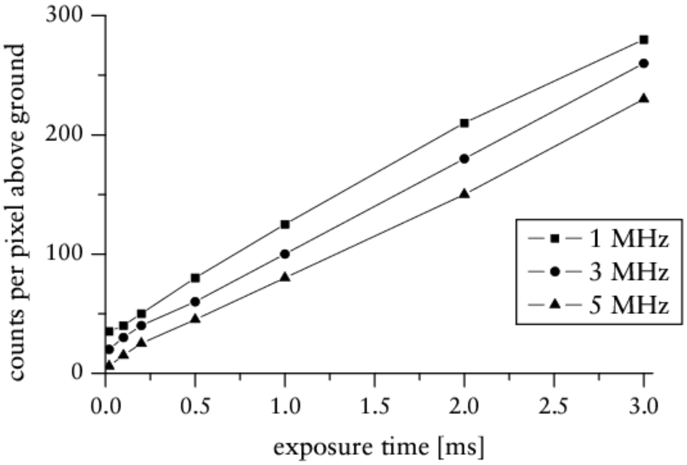

Figure 5.6.: Signal above ground of the CCD camera for different horizontal readout speeds and different exposure times. Intensity for the BD detection beam was adjusted at 2/3 of the saturation intensity. Note that there is no strict linear dependence for very short exposure times. We assume that even if the exposure time was set to zero, the CCD chip was exhibited to photons for a finite duration. This issue was still being investigated as of printing of this thesis.

using the parameters of tabs. 5.1 and 5.2 for different horizontal readout speeds. The result is illustrated in fig. 5.6. At 5 MHz horizontal readout speed the count rate per pixel above ground is about 75 kHz which differs by more than one order of magnitude from our expected results. At the time of printing of this thesis, we were trying to figure out what might cause such a low count rate in collaboration with the manufacturer. In terms of count rate (not normalized per pixel), the CCD still outperforms the PMT—even at very short exposure times.

One drawback of using the CCD camera is the inherent delay between subsequent acquisitions caused by the CCD readout process. Thus, detailed timing information on timescales of nanoseconds—needed for compensation of micromotion, chapter 8 for example—is only available using the PMT.

5.3.1. Noise and gain

In principle, a CCD chip has three sources of noise: thermal noise (thermal release of photoelectrons), clock-induced charge (resulting from shifting the electrons across the CCD chip too fast), and readout noise (caused by the electron-counting sensor). Thermal noise can be reduced very efficiently to values below 1e$^-$/pixel/second by

horizontal readout speed	max. gain at −50 ℃	max. gain at −80 ℃
1 MHz	155	410
3 MHz	195	422
5 MHz	173	647
10 MHz	225	842

Table 5.4.: Maximum EMCCD gains for different CCD chip temperatures. Vertical shift speed was set at 3.4 µs so as to avoid clock-induced charge noise.

cooling the CCD chip to temperatures below −25 ℃. Clock-induced charges may be avoided by lowering the shift speeds transferring the electrons across the CCD chip. However, this also lowers the achievable frame rate (images per unit time). Readout noise is an inherent property of the sensor and cannot be reduced.

We measured the EMCCD gain of our camera using the ion gauge inside our vacuum chamber as a constant light source. For each camera setting we acquired two images; one with the camera shutter opened and one with the shutter closed. The signal can then be defined as the difference in the count rates of the two images. Although EMCCD gain should depend only weakly on the CCD's temperature, we measured considerably distinct values for different temperatures, see tab. 5.4. Maximum gain values throughout improved with decreasing temperatures. Therefore we eventually water-cooled the camera's Peltier cooling element to 18° by connecting it to the chiller of our Verdi V10 laser. We achieved temperatures of down to −90 ℃, stable operation is however only possible above −85 ℃.

5.3.2. Optimisation of image quality

If the objective above the vacuum chamber is misaligned in any way (tilted or off-positioned), image quality and thus spatial resolution is decreased. We conducted the following procedure to optimise the imaging:

- Load one ion into the trap.
- Defocus the ion's image starting from optimum focusing by approaching the objective to the ion. This leads to a halo around the bright spot associated with the ion, see fig. 5.7a.

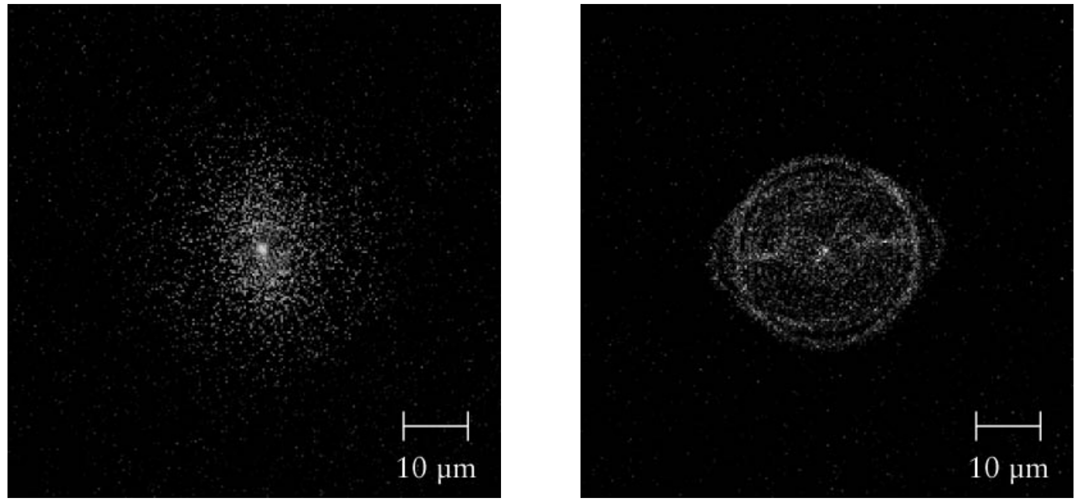

(a) Distance between objective and ion is too small.

(b) Distance between objective and ion is too great.

Figure 5.7.: Defocused images of ions as they appear using the CCD camera. Exposure time was 100 ms, the BD laser parameters were adjusted according to the figures of tab. 4.4.

- Centre the bright spot inside the halo by tilting the objective.
- Defocus the ion's image starting from optimum focusing by moving the objective away from the ion. For our objective this leads to a bright ring, see fig. 5.7b.
- Move the objective perpendicular to the focal plane in order to make the ring appear equally bright at all positions.

On fig. 5.7b, one can see an elliptical structure centred on the circular one. Depending on the amplitude of micromotion the intensity of the two structures changes: If micromotion is virtually zero, the ellipse appears darker than the circle. With increasing micromotion, the ellipse becomes lighter eventually outshining the circle. The reason for this structure is not completely understood. It might be related to polarisation of the scattered light where birefringence of the sapphire crystal window could play a role.

5.4. Auge software

For future experiments involving more than one ion it will be necessary to determine the state of each ion independently. Obviously, such a discrimination is not possible using the PMT—it does not deliver any spatial information. For the sake of spatially discriminating ions, we use the CCD camera.

Although Andor bundles its camera with a powerful software for image acquisition and analysis, this programme does not satisfy our requirements (sorted by decreasing importance):

- Results of image analysis cannot be transferred to our computer in charge of the experimental analysis in real-time.
- Regions of interest, i. e. image subregions that are to be analysed, are rectangular-shaped and can thus not be adapted to the shape of an ion. This restriction leads to a loss of contrast since pixels of the background signal will also be evaluated.
- Regions of interest do not automatically adapt to slightly changed image positions of the ions (which can be attributed to thermal effects of the involved optics).
- Performance of the Andor software is not suitable for the high acquisition rates (more than 100 images per second) needed for our experiments.

The author of this thesis has written a camera controlling and image processing software from scratch in order to overcome these limitations. This software, called *Auge* for simplicity, runs on an AMD Athlon 64 3400+ under Windows. It has been written in C++ using the standard Win32 API for maximum execution speed. For a schematic of the application's components and their cooperation refer to Appendix A.

We can identify two modes of operation. The first is an all-interactive mode actually displaying the camera image on screen. The user can adjust the camera parameters such as exposure time, electron multiplication or readout speeds. Furthermore, the software lets you define elliptical regions of interest that each enclose the image of one ion, see fig. 5.8. The second is a remote-controlled mode where our experimentation software *Flocke* (see section 6.4) takes over control and in turn receives count rates inside the previously defined regions of interest over the TCP/IP network.

Communication between *Flocke* and *Auge* follows a proprietary protocol called Auge Transfer Protocol (ATP). It is a client / server protocol where *Auge* acts as the server and *Flocke* as the client directing commands at *Auge*. See Appendix B for a detailed description.

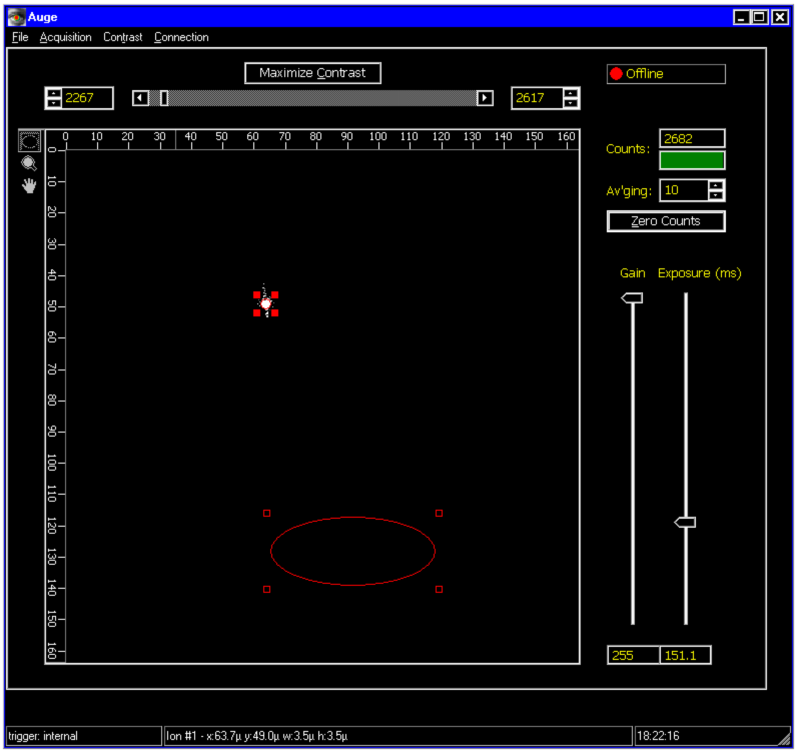
Auge
File
Acquisition
Contrast
Connection
Maximize Contrast
Zero Counts
0 10 20 30 40 50 60 70 80 90 100 110 120 130 140 150 160
0 10 20 30 40 50 60 70 80 90 100 110 120 130 140 150 160

2267

2617

Offline

Counts: 2682

Av'ging: 10

Gain: 255

Exposure (ms): 151.1

trigger: internal

Ion #1 - x:63.7µ y:49.0µ w:3.5µ h:3.5µ

18:22:16

Figure 5.8.: Screenshot of *Auge* in interactive mode.

As one particular quantum simulation experiment (including the process of state detection) has to be repeated several hundred times to acquire one data point, it is desirable to minimize the time elapsing between subsequent CCD readouts. In interactive visualisation mode where we read out the full CCD frame this is at least 57 ms or 17.5 frames per second (FPS) using the parameters of tab. 5.2. The camera offers two techniques to decrease readout times:

- Adjustment of the readout frame. Here, the camera will readout a small rectangular portion of the whole image frame. *Auge* automatically calculates the minimum image frame that still encompasses all the regions of interest. For a square of 5×5 pixels (encompassing one ion) we attain about 580 FPS. In first order, the duration for reading one frame scales linearly with its size.
- Row-wise acquisition. In this mode, the CCD chip is exposed several times before being read out, see fig. 5.9. This is only feasible if several image rows fit onto the

CCD chip concurrently. A rectangular frame of 512 × 5 pixels fits onto the chip 204 times and leads to a maximum frame rate of about 1700 FPS.

As *Flocke* takes over control, it transfers the desired frame rate to *Auge* which in turn switches to the most feasible camera readout mode that still fulfils the frame rate desires. Although row-wise acquisition allows for higher frame rates, it involves additional effort to coordinate subsequent acquisitions. As the CCD is not cleared after every exposure we have to make sure that we shift the CCD photoelectrons as soon as acquisition time is over. Let's refer to this acquisition as row no. 1. Subsequently, we will most probably perform operations involving fluorescence of the ions, e. g. a Doppler re-cooling process, which we do not need to acquire. Thus, the next row no. 2, can be ignored. Only the following row, no. 3, will again contain relevant data. This procedure effectively halves the frame rate.

As the CCD is not cleared after every exposure, any background signal that affects the entire CCD frame is accumulated *within every row acquired*. This effect might be reduced by properly positioning an aperture in front of the camera; this however limits the significance of full frame acquisitions (which are very handy during the ion loading process) .

Further problems arise due to the intermittent readout of the CCD. This readout takes about 120 ms. Consequently, we will have to suspend the experiment for at least 120 ms before we continue acquisition. Take the example given in fig. 5.9: We take seven exposures without any waiting times in between, then we will have to wait for the CCD to be read out and suspend experimentation for the meantime.

Due to the drawbacks involved with row-wise acquisition, it will be advantageous to use the method of adjusting the readout frame for realising our first experiments including [9]. This mode is easier to operate and synchronize with the actual experiment. However, it also shows some peculiarities. When the readout frame is reduced (this occurs when we switch from the all-interactive to Flocke-controlled mode), the CCD's dark count rate increases at timescales of minutes. This behaviour might be associated with heating effects inside the CCD. With smaller readout frames, i. e. higher frame rates, the chip temperature rises, eventually leading to an increased dark count rate. At the time of printing of this thesis, we were still investigating this issue in collaboration with the camera's manufacturer. This behaviour persisted even if we water-cooled the CCD to −80 ℃.

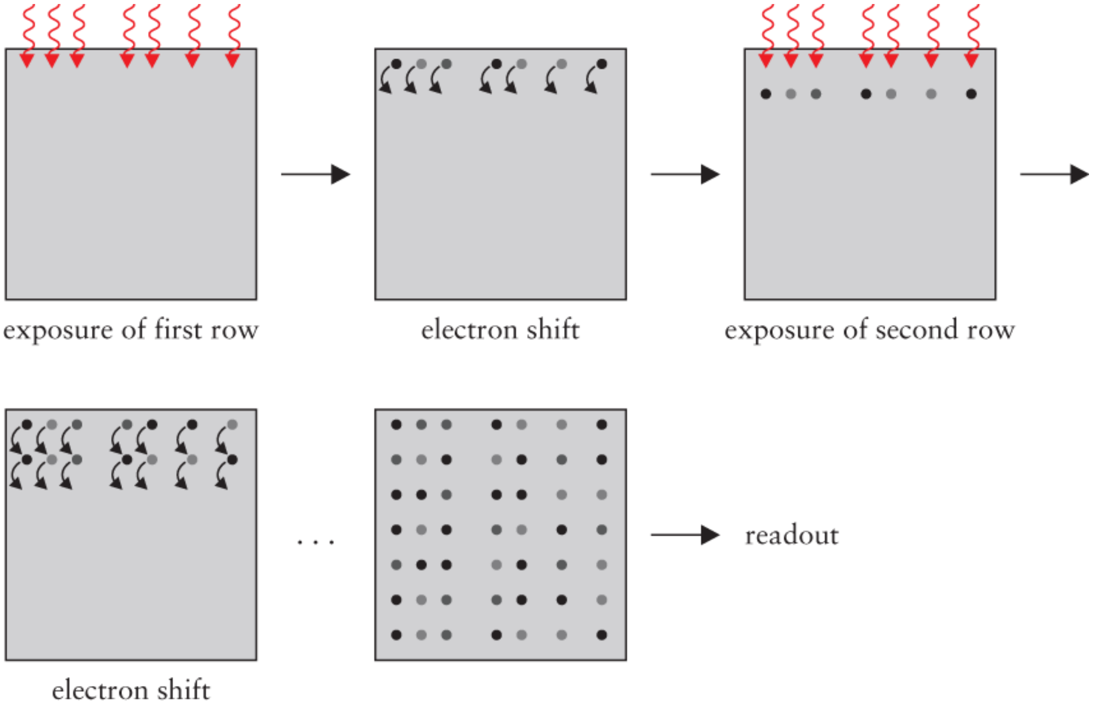
exposure of first row
electron shift
exposure of second row
electron shift
. . .
readout

Figure 5.9.: Row-wise acquisition mode. In the case illustrated seven acquisitions fit on the CCD chip at the same time.

6. Experimental control

An experimental control system used to conduct quantum simulation experiments must satisfy the following requirements:

- High repetition rates. Any experiment dealing with measurements of quantum states has to acquire considerable amounts of statistical data (by conducting the same experiment over and over again) in order to make statements on superposition states. Thus, the duration for the acquisition of one data set crucially depends on the repetition rate.
- Good time resolution. Typical pulse durations for the laser beams involved in a quantum simulation experiment are of the order of 10 µs. Therefore, an experimental control system must be able to control associated components with a time resolution of better than 100 ns.
- Precise adjustment of the frequencies, phases, and amplitudes of RF output. This output will be used to drive acousto-optical modulators (AOMs) that provide the required laser beam switching and frequency-shifting capabilities.

We meet these requirements using a home-built all-digital control box which is clocked at 100 MHz and communicates with a self-written computer programme. For simplicity, this box will be referred to as the *Paul box* [40, 41], according to its manufacturer. It controls particular AOMs and provides TTL outputs to trigger other devices in the laboratory. In addition, we use what we will call the *Jäger box*[*] which controls the DC voltages at the trap electrodes and provides certain measurement capabilities.

6.1. AOM control

During experimentation all of our Raman beams (see section 4.3.2) have to be controlled with respect to their amplitude, frequency, and mutual phase. As these parameters are subject to change during an experiment, we drive the respective AOMs using the Paul box frequency generation feature. Other beams (BD or RD beams) will retain their frequencies and amplitudes during an experiment, but will still have to be switched on and off. Driving signals for the AOMs of these beams can thus be generated externally by voltage-controlled oscillators (VCO, MiniCircuits ZX series), appropriately attenuated using manual variable or even fixed RF attenuators, and eventually switched on and off by RF switches (MiniCircuits ZASW series). It is thus sufficient to control these switches using the Paul box TTL output facility.

---

[*] Jäger Computergesteuerte Messtechnik, http://www.adwin.de/

Driving powers for the UV AOMs (IntraAction ASM series) are 2.0 W each, and 3.5 W for the deflector (Raman blueshifter). We use RF amplifiers (MiniCircuits ZHL series) with gains between 30 dB and 40 dB to achieve these powers.

6.2. Paul box

We use the Paul box primarily to control all relevant AOMs, some of which must only be switched on and off while the driving input of others must be controlled in amplitude, frequency, and phase. As the time resolution of Paul box commands and actions is 10 ns, we also use it for accurate triggering of other devices in the laboratory.

6.2.1. Assembly

An overview of the components included in the Paul box is given in fig. 6.1. An externally generated reference frequency of $f_0 = 1.2\,\mathrm{GHz} \pm 1\,\mathrm{Hz}$ (Hewlett-Packard HP8660C) is fed into four direct digital synthesisers (DDS) each of which can generate sinusoidal signals with an arbitrary frequency $f < f_0/2$ and an arbitrary phase. The output of each DDS board can be individually varied in amplitude using voltage variable RF attenuators. Each attenuator is connected to a digital-to-analog converter (DAC) which determines its attenuation factor; the dynamic range at 220 MHz is 26 dB, see fig. 6.2. Our box is equipped with four of these universal frequency generation units. All the DDS and DAC boards are in turn controlled by a microprocessor (field programmable gate array, FPGA) clocked at 100 MHz which receives its commands over an Ethernet network. The FPGA can also directly control sixteen TTL output signals and can be triggered by a total of eight TTL inputs, although the triggering feature has not been required for the experiments conducted within the scope of this thesis.

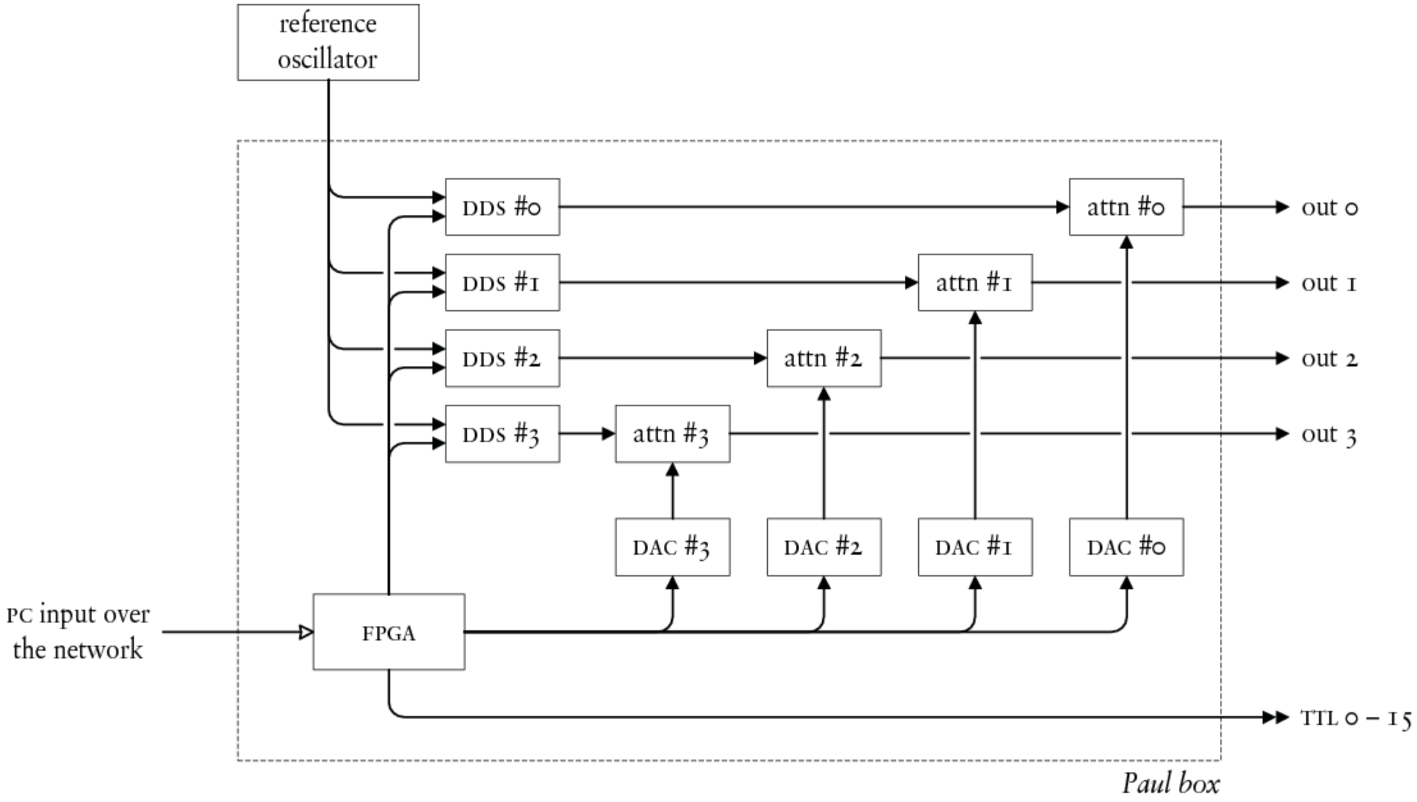
reference oscillator
DDS #0
DDS #1
DDS #2
DDS #3
attn #0
attn #1
attn #2
attn #3
out 0
out 1
out 2
out 3
DAC #3
DAC #2
DAC #1
DAC #0
PC input over the network
FPGA
TTL 0 – 15
Paul box

Figure 6.1.: Schematic of Paul box functionality. Legend: FPGA = field programmable gate array (programmable processor), DDS = direct digital synthesis board, DAC = digital-to-analog converter, attn = RF attenuator.

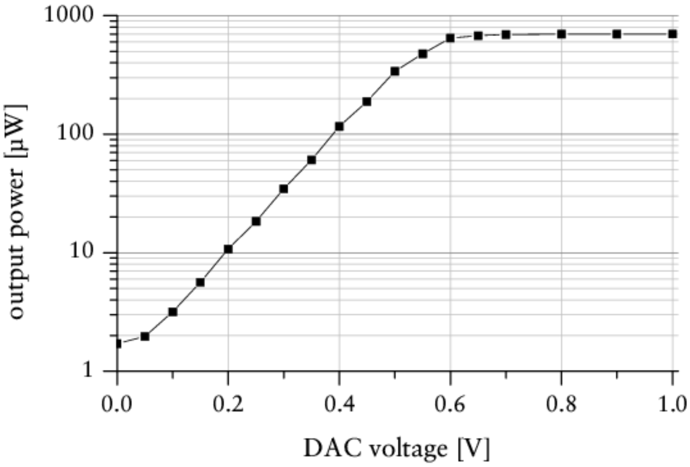

Figure 6.2.: Output RF power behind the Paul box's voltage-variable attenuators at 220 MHz. The remaining output power at a DAC setting of zero can be switched off completely by either switching off DDS output or by using RF switches.

The Paul box was designed by Paul T. Pham[†] who assembled all the hardware on site at Garching. He has also constructed similar boxes for the quantum simulation/computation groups at Innsbruck, Austria and the University of Washington, Seattle. Unfortunately, there was not enough time for Paul to thoroughly test and debug his box before he had to return to the US. As a consequence, we spent considerable time to eliminate particular bugs. Just a few examples: One of these bugs relates to the fact that our box contains four DDS boards instead of the two DDS boards included in all the boxes that had been built before. The different signal delays in the connecting cables of the DDS boards destroyed temporal synchronisation between the individual DDS boards. Shortening the cable lengths eventually solved this problem. Another bug was hidden on the commercially available DDS boards themselves. Their circuits contained an erroneous connector that we had to remove by soldering. Tedious work was also spent on debugging the DAC boards. Originally they were designed to operate with a differential EVENT input. As this proved no stable operation we re-soldered these boards to accept unipolar EVENTs. Anyway, after these repair works, the Paul box proves to be a very stable and reliable piece of hardware. We stress that we would not have been able to construct a similar box on our own.

[†] ppham@cs.washington.edu

6.2.2. FPGA software

The FPGA is responsible for the following tasks:

- Receiving input over the Ethernet network. The input is called a *pulse programme* containing directives for the DDS boards, DAC boards, and TTL outputs and is transferred to the box inside a proprietary wrapper protocol called Pulse Transfer Protocol (PTP).
- Executing the pulse programme. This part of the FPGA software is called Pulse Control Processor PCP. Apart from pulse commands it also handles `WAIT` instructions, `LOOP`s and subroutines. With the FPGA being clocked at 100 MHz the PCP will process simple commands (such as TTL switching) within 10 ns.

As the FPGA and the DDS boards are clocked by different frequency sources, i. e. they are not synchronised, we observe a max. 10 ns jitter between the execution of FPGA commands and DDS operation. For our experiments however, this jitter will not measurably decrease fidelities of quantum state manipulations.

The FPGA software may be regarded as beta software (work in progress), and as such it still contains a number of bugs. Thanks to Paul's assistance we corrected almost all of them—at least those whose presence avoided proper experimentation operation.

6.2.3. PCP compiler

Before being sent to the Paul box a pulse programme has to be translated into a binary that is understood by the PCP. Such a compilation is most conveniently done on the computer communicating with the box. While we were still testing and debugging the box hardware and software, we used an already existing Python interface for this purpose. Soon it became clear however that performance of the Python compiler would not suffice to conduct our experiments (probably due to heavy use of object allocation during the compilation process). We eventually developed our own PCP compiler written in C/C++ to speed operations up. That way, compilation times for a typical pulse programme with some 100 kB decreased by a factor of about 2000.

Although being developed in C/C++ we have designed our compiler as a Python module so that existing programmes—especially our graphical user interface (GUI) programme—could easily make use of it. The compiler accepts a very simple human-readable pulse description language (see Appendix C) that still encompasses all the PCP features.

6.3. Jäger box

The Jäger box—an ADwin-Gold system—features 8 DACs and 16 ADCs for analog applications (both offering full-range resolutions of 0.3 mV), and a total of 32 digital in-/outputs as well as 4 TTL counters with a time resolution of 50 ns for digital applications. In contrast to the Paul box it can handle several processes at the same time in a multitasking environment. The logic of these processes remains the same for every experiment, which is why they are loaded once and then run forever (well, at least until the box is switched off). Data exchange with a computer is then carried out via Ethernet/UDP.

The status quo of our experimental setup is to have three processes running on the Jäger box:

- A low-priority process controlling the DC voltages at the trap's sub-electrodes. By adjusting these voltages we can—by means of software implementation—shift ions from the loading section into the experimentation section of the trap and vice versa. Furthermore, the axial confinement can be varied this way.
- A high-priority process counting the pulses of a photomultiplier (PMT) and outputting the count value upon the arrival of an external trigger.
- Another externally triggered process that measures the voltage of a time-to-amplitude converter (TAC) used for compensation of micromotion (see chapter 8).

6.4. Interplay

The heart of our experimental control system is a piece of software called *Flocke*[‡]. It has been written using Python [42] and features a portable GTK user interface (see fig. 6.3), result displaying and saving capabilities. It runs under Linux on an AMD Athlon XP 2800+ machine connected to a 100 MBit network.

Fig. 6.4 illustrates the interplay between *Flocke* and the other components controlling and evaluating an experiment. On the input side we have a total of three tools at hand to investigate ions in the trap. The camera and PMT are primarily used to measure the fluorescence of an ion expressed in a count rate. Their detection processes thus have to be synchronised to the BD detection laser beam. The camera receives its acquisition triggers by the Paul box, respective count rates are transferred to *Flocke*

[‡] Obviously it had been snowing when the programme was given its name.

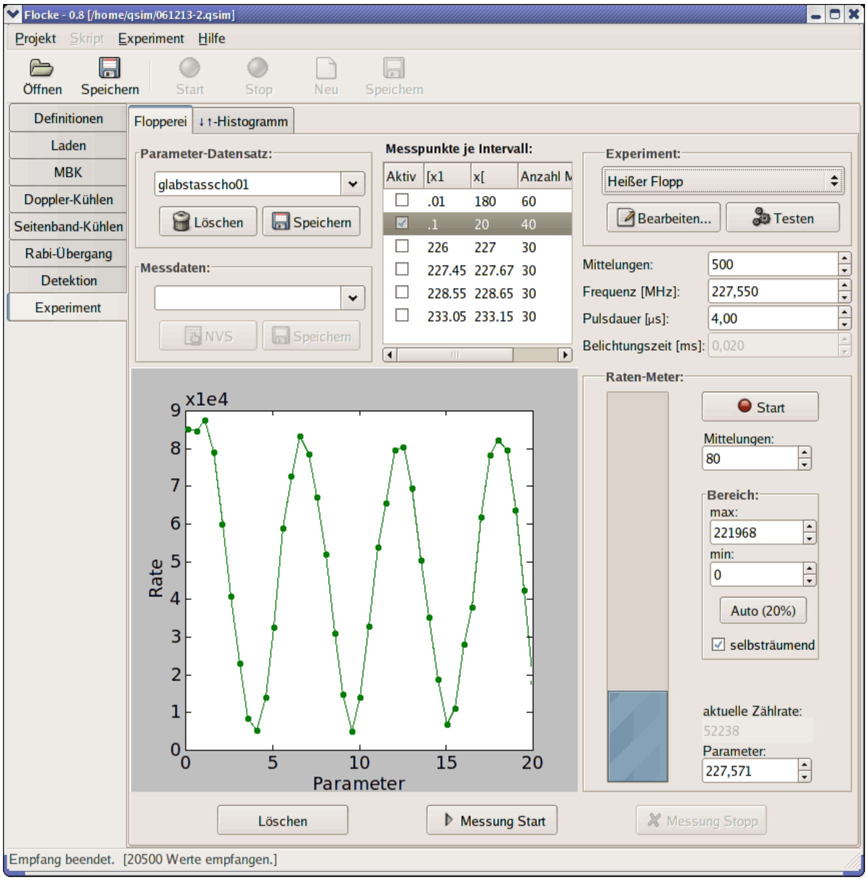
Projekt
Skript
Experiment
Hilfe
Öffnen
Speichern
Start
Stop
Neu
Speichern
Definitionen
Laden
MBK
Doppler-Kühlen
Seitenband-Kühlen
Rabi-Übergang
Detektion
Experiment
Flopperei
↓↑-Histogramm
Löschen
Speichern
NVS
Speichern
Bearbeiten...
Testen
Start
Auto (20%)
x1e4
9
8
7
6
5
4
3
2
1
0
Rate
0
5
10
15
20
Parameter
Löschen
Messung Start
Messung Stopp

Flocke - 0.8 [/home/qsim/061213-2.qsim]

Parameter-Datensatz: glabstascho01

Messdaten:

Messpunkte je Intervall:

Aktiv	[x1	x[	Anzahl M
☐	.01	180	60
☑	.1	20	40
☐	226	227	30
☐	227.45	227.67	30
☐	228.55	228.65	30
☐	233.05	233.15	30

Experiment: Heißer Flopp

Mittelungen: 500

Frequenz [MHz]: 227,550

Pulsdauer [μs]: 4,00

Belichtungszeit [ms]: 0,020

Raten-Meter:

Mittelungen: 80

Bereich:

max: 221968

min: 0

☑ selbsträumend

aktuelle Zählrate: 52238

Parameter: 227,571

Empfang beendet. [20500 Werte empfangen.]

Figure 6.3.: Screenshot of *Flocke* at work.

by the visualisation software *Auge*. In the case of PMT acquisition, the Paul box sends its triggers to the Jäger box which in turn returns the number of PMT clicks that have occurred between two subsequent trigger events. Both input devices (including the visualisation software *Auge*) are described in more detail in chapter 5.

The TAC—a stand-alone NIM component—is a special input device in the way that it is exclusively designated for compensation of micromotion (see chapter 8). Its start and stop triggers are supplied by the PMT on the one hand and a rising-edge zero-crossing of the radial confinement RF voltage on the other.

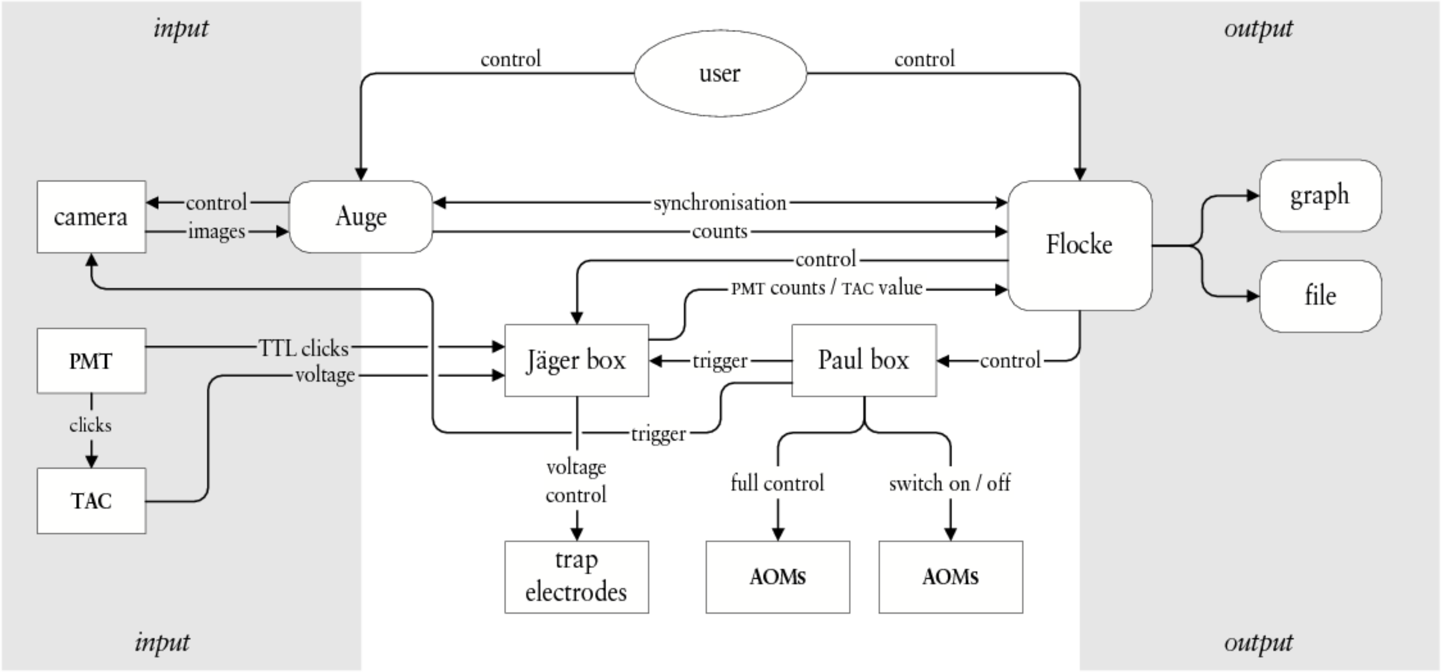
input
output
control
user
control
camera
control
images
Auge
synchronisation
counts
Flocke
graph
file
control
PMT counts / TAC value
PMT
TTL clicks
voltage
Jäger box
trigger
Paul box
control
clicks
TAC
trigger
voltage control
full control
switch on / off
trap electrodes
AOMs
AOMs
input
output

Figure 6.4.: Interplay of the components controlling operation of our experiments.

Part III.

Experimental issues

7. Simulating the Early Expanding Universe

The theory of quantum fields in curves space-times (see e. g. [10]) comprises many fascinating and striking phenomena—one of them being the amplification of quantum vacuum fluctuations due to the rapid expansion of space-time. According to our standard model of cosmology this effect has caused the generation of the seeds for cosmological structure formation during the very early moments of the universe. Although these effects are far removed from every-day experience, they are very important for the past and the future fate of our universe. Thus, it would be desirable to render these phenomena accessible to an experimental verification.

Ions confined in a Paul trap are particularly well suited as an analogue system which can reproduce the Hamiltonian of quantum fields. The analogue of an initially empty universe is achieved by cooling the ions to their motional ground state. Subsequent creation of particles is simulated by phonons which can be sensitively detected.

7.1. Theoretical considerations

The considerations presented in this section are part of [9] and were only possible due to the close and fruitful collaboration with Ralf Schützhold.

7.1.1. Original system

Consider a massless scalar field Φ in curved space-time coupled to the Ricci (curvature) scalar $\mathfrak{R}$ via a dimensionless parameter ζ [10]. Using the Friedmann-Robertson-Walker metric

$$\mathrm{d}s^2 = \mathfrak{a}^6(t)\mathrm{d}t^2 - \mathfrak{a}^2(t)\mathrm{d}\mathbf{r}^2 \tag{7.1}$$

where $\mathfrak{a}(t)$ denotes a time-dependent scale parameter (corresponding to cosmological expansion / contraction) we can derive the wave equation

$$\left(\frac{\partial^2}{\partial t^2} + \left[\mathfrak{a}^4(t)\mathbf{k}^2 + \zeta\mathfrak{a}^6(t)\mathfrak{R}(t)\right]\right)\Phi_{\mathbf{k}} = 0 \tag{7.2}$$

where each mode $\mathbf{k}$ represents a harmonic oscillator with a time-dependent potential $\mathfrak{a}^4(t)\mathbf{k}^2 + \zeta\mathfrak{a}^6(t)\mathfrak{R}(t)$. For a non-adiabatical time-dependence the initial vacuum state $|0\rangle$ containing no particles will evolve into a squeezed state

$$|\psi(t)\rangle = \exp\left\{\sum_{\mathbf{k}} \xi_{\mathbf{k}}\hat{a}_{\mathbf{k}}^2 - \text{h. c.}\right\}|0\rangle \tag{7.3}$$

where $\hat{a}_{\mathbf{k}}$ denotes the annihilation operator for mode $\mathbf{k}$ and $\xi_{\mathbf{k}}$ is the respective squeezing parameter which is determined by the solution of eq. (7.2).

7.1.2. Analogue system

The equations of motion for the axial positions q_i of ions crystallised and confined to a string along the axis of a linear trap are given by

$$\left(\frac{\partial^2}{\partial t^2} + \omega_z^2(t)\right) q_i = \frac{e^2}{4\pi\epsilon_0}\sum_{j\neq i}\frac{\text{sign}(i-j)}{(q_i - q_j)^2} \tag{7.4}$$

where $\omega_z(t)$ is a time-dependent axial oscillator frequency and the term on the right hand-side encodes the mutual repulsive Coulomb interaction of the ions, e is the electron charge and $epsilon_0$ is the vacuum permittivity.

The solution of eq. (7.4) is obtained via the scaling ansatz

$$q_i(t) = b(t)\cdot q_i^0 \tag{7.5}$$

where q_i^0 are the initial static equilibrium positions. We thus obtain an equation for the evolution of the scale parameter $b(t)$:

$$\left(\frac{\partial^2}{\partial t^2} + \omega_z^2(t)\right) b(t) = \frac{\omega_z^2(t=0)}{b^2(t)}. \tag{7.6}$$

Now we introduce quantum fluctuations by splitting the position operator $\hat{q}_i(t)$ for each ion into its classical trajectory $b(t)q_i^0$ and a fluctuation term $\delta\hat{q}_i(t)$:

$$\hat{q}_i(t) = b(t)q_i^0 + \delta\hat{q}_i(t). \tag{7.7}$$

Since the fluctuations $\delta\hat{q}_i(t)$ are very small for magnesium ions, we may linearise the full equation of motion (7.4). After a normal-mode expansion we get

$$\left(\frac{\partial^2}{\partial t^2} + \omega_z^2(t) + \frac{\omega_\kappa^2}{b^3(t)}\right)\delta\hat{q}_\kappa = 0 \tag{7.8}$$

for the phonon modes κ.

Comparing eqs. (7.2) and (7.8) we observe a strong similarity if we identify $\Phi_{\mathbf{k}}$ with $\delta\hat{q}_\kappa$. The wavenumber $\mathbf{k}^2$ from eq. (7.2) directly corresponds to the phononic eigenfrequency ω_κ^2 in eq. (7.8) and the scale factors $\mathfrak{a}(t)$ and $b(t)$ can be linked in a similar way.

In view of the formal equivalence of eqs. (7.2) and (7.8) we expect the system of ions to show the same effects as the original cosmological system. In particular, we will be interested in the analogue effect of eq. (7.3): Introducing a non-adiabatic time dependence of the axial oscillator frequency $\omega_z(t)$ should excite squeezed phonon modes of the trapped ions [43, 44]. It is important to note that a squeezed phonon state differs inherently from a classical oscillation and can only be explained by quantum effects, see fig. 7.1.

7.2. Experimental implementation

7.2.1. General setup

To perform a first experimental realisation of the proposed experiment we would confine one single magnesium-25 ion to the axis of our trap (see chapter 3). The simulation basis will be provided by the hyperfine ground-state level $3S_{1/2}\,|F=3, m_F=3\rangle \equiv |{\downarrow}\rangle$ and the harmonic oscillator levels arising from the axial confinement of the ion which can be characterised by its resonance frequency ω_{axial} (see chapter 2). The constant magnetic field of section 3.4 will define the quantisation axis for the laser fields and lift the degeneracy of the $3S_{1/2}$ hyperfine level manifold.

7.2.2. Protocol of the experiment

At the start of each experiment, the ion will be laser-cooled close to the ground state of the axial motion (see section 2.6) and optically pumped into the electronic $|{\downarrow}\rangle$ state. We will adiabatically decrease the axial confinement and subsequently reset it to its initial value on a non-adiabatic timescale, similar to a proposal in [45]. Since the width of the ground-state wave function of the ion cannot adiabatically adapt to the new confinement, it will breathe in the final trapping potential. This non-classical oscillation can be described via the squeezed state formalism mentioned in section 7.1.

The readout of the final motional state (which is the quantity of interest for this experiment) occurs via mapping the motional state onto an internal electronic state $|{\uparrow}\rangle \equiv 3S_{1/2}\,|F = 2, m_F = 2\rangle$ separated from the $|{\downarrow}\rangle$ state by the hyperfine splitting of $\omega_0 = 1789\,\mathrm{MHz}$ (see fig. 2.1). There are proposed [46] and already realised [45] methods to provide the mapping of motional states to internal electronic states. That way, we may take advantage of the high accuracies available for internal state detection.

We suggest two-photon stimulated Raman transitions near 280 nm for this purpose, see section 2.4.1. Their wavevector difference $\Delta\mathbf{k} = \mathbf{k}_2 - \mathbf{k}_1$ is aligned along the trap axis thus coupling to the axial motional states. Their frequency difference $\Delta\omega = \omega_2 - \omega_1$ can be precisely adjusted using acousto-optical modulators (AOMs). Transitions on the carrier ($|{\downarrow}, n\rangle \leftrightarrow |{\uparrow}, n\rangle$, $\Delta\omega = \omega_0$), first sidebands ($|{\downarrow}, n\rangle \leftrightarrow |{\uparrow}, n \pm 1\rangle$, $\Delta\omega = \omega_0 \pm \omega_{\text{axial}}$), and second sidebands ($|{\downarrow}, n\rangle \leftrightarrow |{\uparrow}, n \pm 2\rangle$, $\Delta\omega = \omega_0 \pm 2\omega_{\text{axial}}$) can be accomplished at high fidelities.

At the end of each simulation experiment, we will have to read out the motional state population. In our setup, state-sensitive detection is performed by the BD laser beam that resonantly couples the $|{\downarrow}\rangle$ state to the $3P_{3/2}$ level thereby scattering photons at 10 MHz rates, see section 2.3. This allows to distinguish the "bright" $|{\downarrow}\rangle$ state from the "dark" $|{\uparrow}\rangle$ state with high accuracy—even at low photon detection efficiencies.

For the special case of experiment considered here we suggest a method for reading out the most important motional state population of the squeezed state, $n = 2$, via a second red sideband transition followed by a carrier transition. The former transfers the motionally excited population $|{\downarrow}, n = 2\rangle$ into $|{\uparrow}, n = 0\rangle$ leaving $|{\downarrow}, n = 0\rangle$ untouched as there is no red sideband transition for that population. The latter transition will exchange the populations of the two electronic levels*. After this step, the population

---

*The attentive reader will have noticed that co-propagating Raman beams are required for this step, see section 2.4.1.

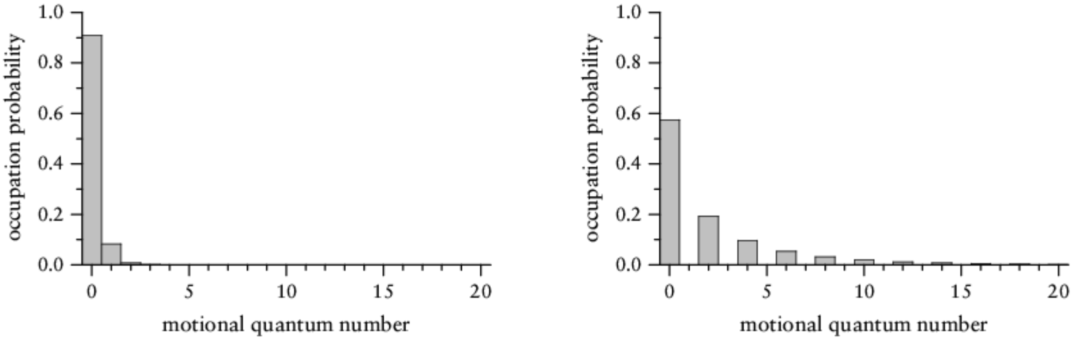

(a) Thermal distribution with $\overline{n} = 0.1$. (b) Squeezed distribution with $\overline{n} = 2$.

Figure 7.1.: Calculated occupation probabilities of motional states in our trap at the final axial confinement of $\omega_z = 2\pi \cdot 2\,\mathrm{MHz}$. The figures show the thermal spectrum after resolved-sideband cooling and the expected squeezed distribution both characterised by their mean motional quantum number $\overline{n}$.

initially in the $n = 2$ state will have been transferred into $n = 0$ whereas the population initially in the $n = 0$ state will reside in the electronic $|\uparrow\rangle$ state. State-sensitive detection will then provide the two-phonon ($n = 2$) generation probability (but see below for complications).

7.2.3. Expected results

Ramping the axial potential from 100 kHz up to 2 MHz in a non-adiabatical way, i. e. fast compared to the oscillation period of the lower frequency, requires a rise time of the order of 1 µs. For our trap geometry, the corresponding voltage range is several 10 V. We expect to observe considerable blind currents during the ramping process caused by the trap electrodes' low-pass filters (see section 3.1.2). We will also have to carefully balance the applied voltages as they are modified. Otherwise, the ion's axial motional mode could be excited classically; we might even lose the ion due to unsufficient confinement. The duration of the experiment ($\sim 3\,\mathrm{ms}$) should be kept short compared to the thermal heating times (estimated ~ 0.01 excited motional quanta per millisecond)—although the thermal and squeezed motional spectra should still be distinguishable for higher temperatures.

Our numerical simulations indicate that we should be able to "squeeze" more than 20% of the motional state population from the initial ground state $n = 0$ into $n = 2$, see fig. 7.1. Since the state-of-the-art fidelities for the carrier and sideband transitions as well as the state-sensitive detection exceed 99% we expect the creation and the parameters of the squeezed state to be measurable with high accuracy, especially in comparison with a purely thermal state.

Relying on driving the second red sideband transition, the suggested readout scheme will also transfer population from motional states $n > 2$ into their respective lower states. Thus, a heated thermal population might lead to the same signal as a squeezed one. We will discriminate these two distributions by an additional signal acquired using a first red sideband – carrier sequence (analogous to the second red sideband – carrier sequence mentioned above) thereby detecting the population in $n \geq 1$. The ratio of the two signals will then provide us with the precise occupation probabilites of the motional state $n = 1$.

7.2.4. Further applications

The investigation of non-adiabatic switching of trapping potentials and the influence on the quantum state of motion might shed light on possible problems with fast-shuttling schemes for ions in multiplex trap architectures. These are required for scaling the ion trap approach towards a universal quantum computer.

8. Compensation of micromotion

As introduced in section 3.1.1 any radial motion in our linear Paul trap is associated with micromotion. We shall call this type of micromotion *natural micromotion* as it is an inherent part of motion in a Paul trap. In contrast we will speak of *excess micromotion* when it comes to micromotion caused by external imperfections such as external electric fields displacing the ions from the trap axis.

For our quantum simulation experiments it is crucial that excess micromotion is reduced to a minimum. Uncompensated excess micromotion will be responsible for the appearance of sidebands. This in turn will have negative effects on any experiment including

- heating the ions with the BD beam (which is actually intended for cooling them) due to a possible blue-detuning with respect to red sidebands,
- reduced Doppler cooling rates as some fraction of the cooling transition line will be distributed to sidebands and thus be "lost",
- the possibility to drive unwanted transitions due to the coupling to sidebands,
- a higher probability for ion loss due to high-energetic collisions with particles from the residual gas,
- longer Doppler-cooling durations before the ion(s) form(s) a proper ion crystal.

8.1. Theoretical background

8.1.1. Sources of micromotion

We will consider three sources of excess micromotion:

- External electric DC fields in the radial directions. These displace the ions from their centred positions on the trap axis defined by the RF quadrupole potential. With one RF electrode being closer to the ion than the opposing one, the ions will be exerted to a force oscillating with the RF frequency.

- Phase difference of the driving RF voltage at opposing electrodes. This will cause the extremum of the quadrupole potential to shift spatially during an oscillation period of the driving RF voltage.
- Disadvantageous axial position of the ion. The DC subelectrodes are separated by slits whereas the RF electrodes aren't. An axial off-position from the centre between two opposing DC electrodes will thus induce a net oscillating force on the ion.

8.1.2. Modulated Bloch equations

The following derivation of why and how sidebands emerge in the case of excess micromotion largely follows [47]. Assuming for simplicity that both sources of micromotion only have an effect in the trap $\hat{x}$ direction, it will be sufficient to modify the respective equation (3.1) as follows:

$$x(t) = (x_{\mathrm{DC}} + x_0 \cos(\omega_x t + \phi_x)) \left(1 + \frac{q}{2} \cos \Omega_{\mathrm{RF}} t\right) - \frac{1}{4} q R \alpha \phi_{\mathrm{RF}} \sin \Omega_{\mathrm{RF}} t, \tag{8.1}$$

where x_{DC} describes the offset due to external DC fields and the last term takes care of a phase difference ϕ_{RF} at the RF electrodes. α is a geometrical factor which quantifies how the opposing RF electrodes differ from an ideal capacitor. Using the software package SIMION we estimate $\alpha \approx 1.4$ for our trap geometry.

An ion oscillating according to eq. (8.1) will—in its rest frame—perceive a different electric field than an ion at rest. Assuming that excess micromotion outperforms secular motion as well as natural micromotion in terms of amplitude, we have

$$\begin{aligned} \mathbf{E}(t) &= \mathbf{E}_0 \exp\left[i\left(kx(t) - \omega t\right)\right] \\ &\doteq \mathbf{E}_0 \exp\left[ik\left(x_{\mathrm{DC}} + \tilde{x}(t)\right) - \omega t)\right], \end{aligned} \tag{8.2}$$

where k is the modulus of the wavevector in the $\hat{x}$ direction and

$$k\tilde{x}(t) = \beta \cos(\Omega_{\mathrm{RF}} t + \delta) \tag{8.3}$$

"combines" the contributions of both sources of excess micromotion and β and δ defined by

$$\begin{aligned} \beta &= \sqrt{\left(\frac{1}{2}kqx_{\mathrm{DC}}\right)^2 + \left(\frac{1}{4}kqR\alpha\phi_{\mathrm{RF}}\right)^2}, \\ \delta &= \arctan\left(-R\alpha\phi_{\mathrm{RF}}, 2x_{\mathrm{DC}}\right) \end{aligned} \tag{8.4}$$

represent the strength and phase of excess micromotion respectively.

The optical Bloch equations for a two-level system interacting with the modulated electric field (8.2) are similar to the unmodulated case; we will merely have to carry out the substitution

$$e^{i\omega t} \longrightarrow e^{i\omega t - i\beta\cos(\Omega_{\mathrm{RF}}t+\delta)} \tag{8.5}$$

resulting in the following set of modulated Bloch equations (don't confuse the Rabi frequency Ω and the driving RF trap frequency Ω_{RF}!):

$$\begin{aligned} \dot{\rho}_{bb} &= -\frac{i\Omega}{2}\left(\rho_{ab}e^{i\Delta t + i\beta\cos(\Omega_{\mathrm{RF}}t+\delta)} - \text{c. c.}\right) - \Gamma\rho_{bb}, \\ \dot{\rho}_{ab} &= \frac{i\Omega}{2}e^{-i\Delta t - i\beta\cos(\Omega_{\mathrm{RF}}t+\delta)}\left(1 - 2\rho_{bb}\right) + (i\Delta - \frac{\Gamma}{2})\rho_{ab}, \\ \dot{\rho}_{ba} &= \dot{\rho}_{ab}^{*}, \\ \dot{\rho}_{aa} &= -\dot{\rho}_{bb}. \end{aligned} \tag{8.6}$$

Fig. 8.1 shows the time-resolved upper-level population of a magnesium ion stored in our trap. There is no steady state any more, rather does the upper-state population—and thus also the fluorescent scattered intensity—oscillate with the driving frequency Ω_{RF}.

8.1.3. Sidebands

During normal, non-time-resolved detection we will not be able to detect oscillations in the population of the upper state but instead observe the mean population (dashed line in fig. 8.1). We can derive an analytical expression for the mean upper-state population by utilising the expansion

$$\exp\left[i\beta\cos(\Omega_{\mathrm{RF}}t+\delta)\right] = \sum_{n=-\infty}^{\infty} J_n(\beta)\exp\left[in(\Omega_{\mathrm{RF}}t+\delta+\pi/2)\right] \tag{8.7}$$

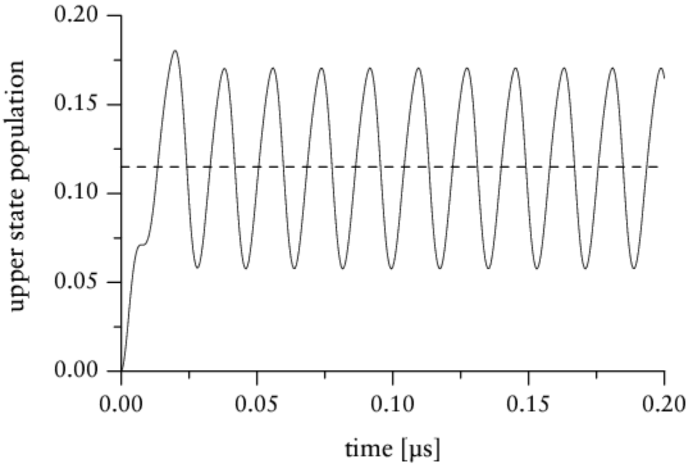

Figure 8.1.: Excess micromotion of a $^{25}\mathrm{Mg}^{+}$ ion stored in our trap at an RF voltage of magnitude 1000 V. This graph was calculated for a moderate excess micromotion amplitude $\beta = 0.7$ resulting from an offset $x_{\mathrm{DC}} = 0.16\,\mu\mathrm{m}$ caused by an external electric field $E_{\mathrm{ext}} = 100\,\mathrm{V/m}$. Parameters of the detection BD laser were taken from tab. 4.4.

where $J_n(\beta)$ signify the Bessel functions of the first kind. This yields [47]

$$\langle \rho_{bb} \rangle = \Omega^2 \sum_{n=-\infty}^{\infty} \frac{J_n^2(\beta)}{(\Delta + n\Omega_{\mathrm{RF}})^2 + (\Gamma/2)^2}. \tag{8.8}$$

Fig. 8.2 illustrates how the associated mean fluorescent scattering rate $r = \rho_{bb}\Gamma$ varies with the detuning Δ of the laser with respect to the actual transition frequency. In addition to the *carrier* peak at $\Delta = 0$ there are peaks at $\Delta = \pm i \cdot \Omega_{\mathrm{RF}}, i \in \mathbb{N}$. We call these patterns *sidebands*—in particular, the peaks where $\Delta < 0$ are referred to as the red sideband while the peaks where $\Delta > 0$ are called the blue sideband. As the micromotion amplitude β increases, more and more contribution is shifted into the sidebands. At the same time the carrier is decreased (the area under the curves of fig. 8.2 is the same for all β).

8.2. Methods for compensation of micromotion

In principle, it is easy to compensate the sources of micromotion. A phase difference of the RF voltage at opposing electrodes as the other source of micromotion is compen-

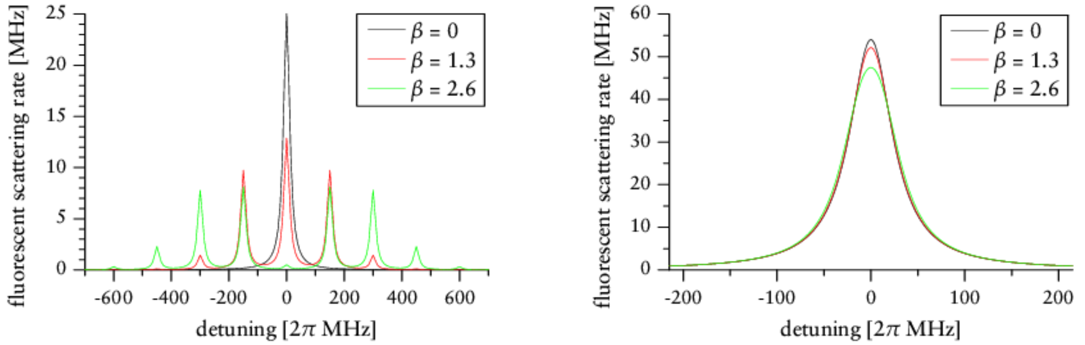

(a) Resolved-sideband case calculated for parameters achieved in the NIST group: $\Omega_{\mathrm{RF}} = 2\pi \cdot 150\,\mathrm{MHz}$, $\Gamma = 2\pi \cdot 20\,\mathrm{MHz}$.

(b) Nonresolved-sideband case calculated for parameters used in [48]: $\Omega_{\mathrm{RF}} = 2\pi \cdot 6\,\mathrm{MHz}$, $\Gamma = 2\pi \cdot 43\,\mathrm{MHz}$.

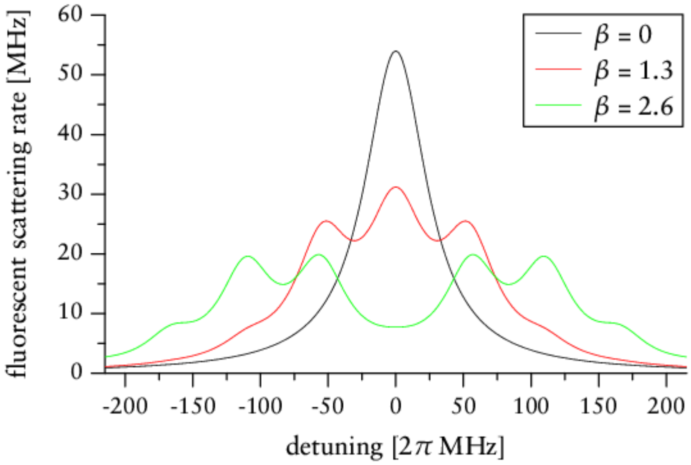

(c) Intermediate case for magnesium ions in our trap: $\Omega_{\mathrm{RF}} = 2\pi \cdot 56\,\mathrm{MHz}$, $\Gamma = 2\pi \cdot 43\,\mathrm{MHz}$.

Figure 8.2.: Sideband structure in dependence of the amount β of micromotion for different ratios of the driving RF frequency Ω_{RF} and the linewidth Γ. All plots were calculated for a laser beam intensity $I = (2/3)I_{\mathrm{sat}}$.

sated by appropriately adjusting the length of the connecting wires. External electric DC fields in the radial directions can be compensated by an antiparallel counteracting field effectively reducing the relevant DC electric field at the trap centre to zero. In our trap apparatus (see fig. 3.1) we can apply compensation fields in the $\hat{y}$ direction and in the $\hat{x}_{\text{ext}}$ direction. The former is achieved by applying differential voltages to the DC sub-electrodes, the latter by applying an appropriate voltage to the compensation electrode located beneath the trap, see fig. 3.1.

In reality, things are a bit more complicated due to the interaction of the radial and axial confinements. As described in section 3.1.3 an axial displacement of the ion will also give rise to micromotion. The reason are the slits between the DC subelectrodes which are not present at the RF electrodes thus introducing an asymmetry of the trap. In order to suppress this source of micromotion we have to adjust the axial position of the ion to match the centre of an opposing electrode pair. That way, we have to take care of three degrees of freedom (differential voltage, compensation electrode, and axial position), which is not really surprising for an ion confined in three dimensions.

For a three-dimensional detection and compensation of micromotion we would need three laser sources shining onto the ions from different (linearly independent) directions. This is because the ion's motion will only modulate the electric field if it has a component parallel to the laser beam wavevector; motion perpendicular to the wavevector does not alter the fluorescent scattering rate. In fact, two laser beams will suffice for our applications.

8.2.1. Minimising ion displacement

Assumed that we can rule out an RF phase difference as the source of micromotion, we have to determine is the compensating electric field. As it compensates external fields that are not related to the trap operation in any way, it should be the same no matter what RF confinement we choose for the ions.

Based on this consideration, we come up with a method that is very easy to implement: As long as external fields are not ideally compensated, ions in the trap will be displaced in the direction of the residual electric field when their RF confinement is reduced. We adjust the compensation field such that varying the radial confinement by tuning the RF voltage magnitude does not displace the ions any more.

We use the CCD camera to determine the position of an ion inside the trap. Whereas it is easy to visualise a displacement in the $\hat{y}_{\text{ext}}$ and $\hat{z}_{\text{ext}}$ directions, changes in the

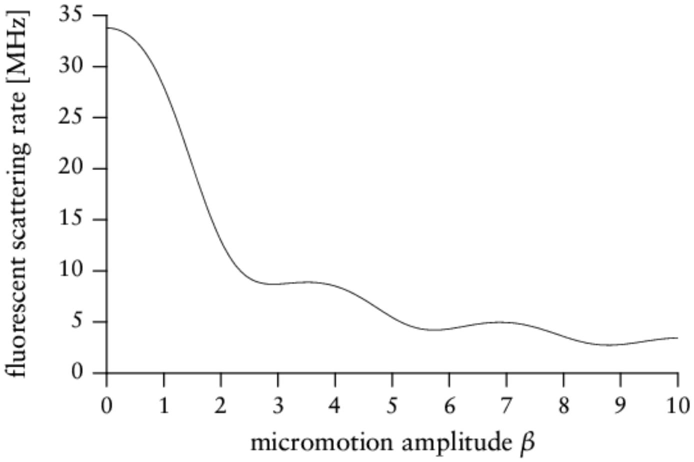

Figure 8.3.: Fluorescent scattering rate for different amounts of micromotion. For this curve a detuning of $\Delta = \Gamma/2$ was chosen. Other laser parameters were taken from tab. 4.4.

$\hat{x}_{\text{ext}}$ position (perpendicular to the focal plane of our objective) can only be detected by different defocusings of the image. As these changes are relatively small when the objective is focused, we initially defocus the objective so that the focal point lies above the ion, $x_{\text{ext}}(\text{focal point}) > x_{\text{ext}}(\text{ion})$. This defocusing setting leads to a circular structured image, fig. 5.7b, whose radius can be associated with the ion position in the x_{ext} direction. The optimum compensation settings are found if the defocused image remains unchanged upon changes in the radial confinement.

Although this method provides an easy way to compensate micromotion, it is not suitable for strong axial confinements. In order to detect displacement of a stored ion, the radial confinement would have to be lowered below a value that still guarantees a stable confinement.

8.2.2. Maximising the fluorescent scattering rate

Fig. 8.2 implies that the fluorescent scattering rate at zero detuning is maximised when there is no micromotion. This is also true for a detuning of $\Delta = \Gamma/2$, which we normally use for optimum Doppler cooling, see fig. 8.3.

Using the photomultiplier or the CCD camera, we can try to maximise an ion's brightness by properly adjusting the differential voltage, compensation electrode, and axial position. As the fluorescent scattering rate rises almost monotonously with decreasing

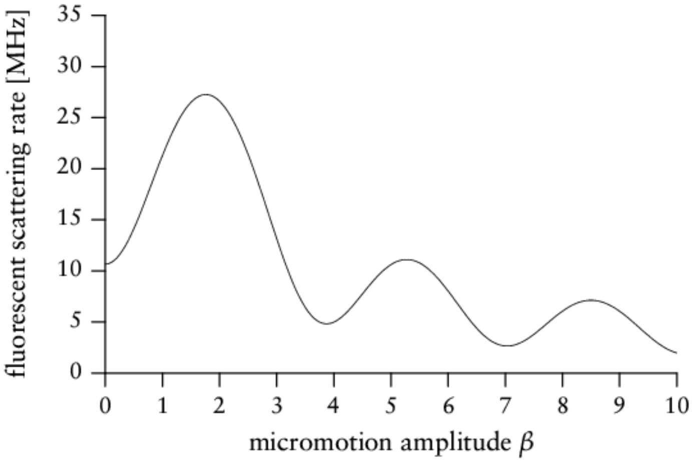

Figure 8.4.: Fluorescent scattering rate for different amounts of micromotion. For this curve a detuning of $\Delta = \Omega_{\mathrm{RF}}$ (the first sideband line) was chosen. Other laser parameters were taken from tab. 4.4. Note that the local minimum at $\beta = 0$ is not the global minimum of the scattering rate.

β, this seems to be feasible at first sight. However, during the adjustment process an ion in the trap will be displaced (basically in any of the three spatial directions), which means that the detection device (PMT or CCD) also has to be readjusted. And adjusting three compensation knobs plus a detection device at the same time can be quite tedious.

One could also try to minimise the fluorescent scattering rate on one of the sidebands' transition lines, for example on the first line where $\Delta = \Omega_{\mathrm{RF}}$. This technique works well for the resolved-sideband case ($\Omega_{\mathrm{RF}} \gg \Gamma$). As can be seen from fig. 8.4 the aspired minimum in our intermediate case (sidebands are resolved only partially) is not a global minimum though. We were thus unable to successfully compensate micromotion using this technique.

8.2.3. Minimising the correlation of photons and RF

This is the preferred method for compensating micromotion. It however involves some additional effort in terms of electronic signal processing. In principle, this method measures the time-resolved fluorescent scattering signal plotted in fig. 8.1: As long as an ion undergoes micromotion, the fluorescent scattering rate will be modulated with the driving RF frequency Ω_{RF}. Thus, the two signals "fluorescent scattering rate" and

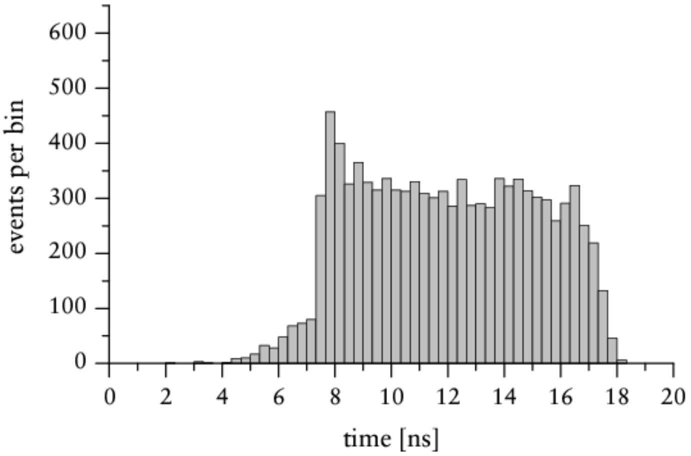

(a) Uncorrelated photon emission (stray light).

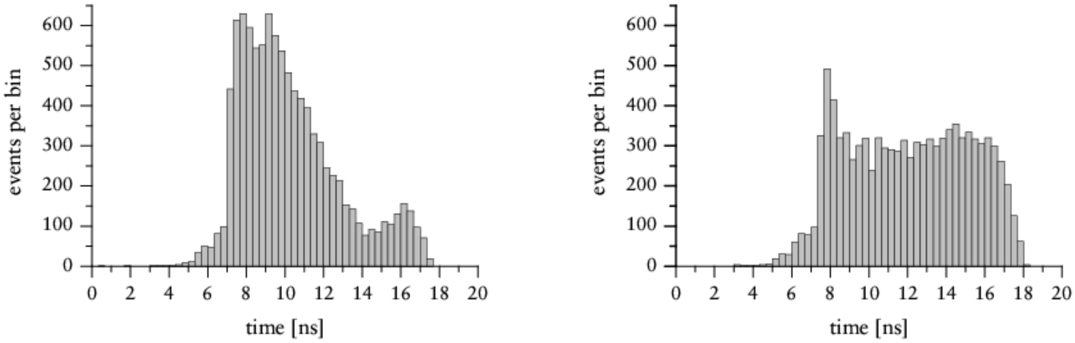

(b) Correlated photon emission (ion undergoing micromotion).

(c) Uncorrelated photon emission (micromotion has been compensated).

Figure 8.5.: Correlation histograms for different amounts of micromotion. The "teapot curve" 8.5a serves as a calibration standard. The deviation from a perfectly flat-shaped histrogram is caused by a technical inadequacy of the TAC module (see main text).

"driving RF frequency" will be correlated. If micromotion has vanished, the fluorescent scattering rate is constant over time and will not be correlated to the driving RF frequency.

Every time our PMT registers a photon, we measure the time it takes till the next rising edge zero-crossing of the RF voltage. The timespans will be in the range $0 < t 2\pi/\Omega_{\mathrm{RF}} = 17.9\,\mathrm{ns}$ for our trap. We use a time-to-amplitude converter (TAC, Ortec model 437A) to convert these short spans into a voltage that can be measured using the Jäger box. After some $10,000$ of these measurements, our control and analysis software *Flocke* draws a histogram of the acquired timespan values.

We expect the histogram to be flat for uncorrelated photon emission and to show a peak somewhere for correlated photon emission (more photons are emitted at a particular phase of the RF voltage than at other times). Results are shown in fig. 8.5. The histogram is not perfectly flat for uncorrelated photon emission because our TAC cannot properly convert timespan values below $7\,\mathrm{ns}$. Apparently, most of the timespan values $t < 7\,\mathrm{ns}$ are not converted at all while values $t \approx 7\,\mathrm{ns}$ are all converted to the same output voltage (corresponding to a timespan of $t = 7\,\mathrm{ns}$). Due to its shape we call the histogram a "teapot curve".

8.3. Experimental results

Although our compensation electrode is located just beneath the trap axis, it only has a small penetration factor of about .... For proper compensation of micromotion we thus have to apply voltages of the order of $10^2\,\mathrm{V}$. The differential voltage applied to opposing DC subelectrodes can be considerably smaller; we would usually operate with voltages of $10^{-1}\,\mathrm{V}$.

If we shine onto the ion using only one laser beam, there are a number of compensation settings that produce flat teapot curves, see fig. 8.6. The optimum compensation setting is the one that also produces a flat teapot curve for a different laser beam (propagating in a different direction). For $^{25}\mathrm{Mg}^+$ this easier said than done as not all laser beams will be able to efficiently cool the ions at the same time. Actually, only the σ^+ polarised BD beam propagating parallel to the magnetic quantisation axis will optimally Doppler-cool the ions and excite them to emit fluorescent light. Laser beams from different directions, e. g. the BD beam entering the chamber via port J (see fig. 3.5), are unable to drive the cycling BD transition and thus unable to cool the ions

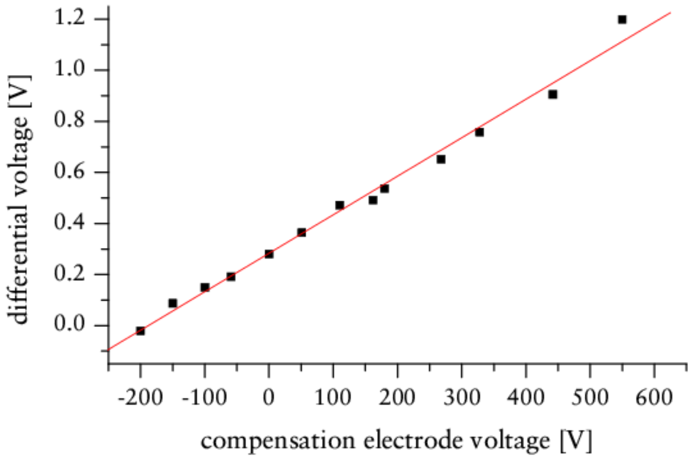

Figure 8.6.: Micromotion compensation settings that produce a flat “tea pot curve”. These data were measured using a single ion in the trap illuminated by the σ^+ polarised BD laser. The optimum compensation settings within the data are those which also produce a flat tea pot curve for a second laser beam propagating in a different direction.

efficiently. Eventually, we would lose an ion that is not illuminated by the σ^+ polarised BD laser.

We overcome this problem by shining onto the ions using two laser beams at the same time; we attenuate the σ^+ polarised BD beam to a minimum that still cools the ions and use the BD beam from chamber port J as a second laser source. That way we can determine an optimum set of compensation settings. These settings were not constant over time however. In particular, we always had to re-adjust the compensation settings after having loaded new ions into the trap. Variances of up to 100% in both the compensation voltage and the differential voltage settings are not unusual.

9. Experiments on coherent transitions

Rabi flopping experiments investigate the Rabi oscillations between the electronic states $|\downarrow\rangle$ and $|\uparrow\rangle$. All these experiments can be characterised by some common parameters: the intensity I_1, I_2 of the two Raman beams, their mutual frequency difference ω_R, their detuning Δ_R with respect to the $3P_{3/2}$ level and the pulse duration (duration that both Raman beams shine onto the ion) τ. For each set of parameters, we repeat $100-1000$ identical experiments to acquire statistics on superposition states. As described in [23], two kinds of acquisition are of special interest:

- Increasing the pulse duration τ after one set of repeated identical experiments while leaving all other parameters unchanged. With this setup we measure the Rabi flopping in dependence of time, see fig. 9.1a.
- Scanning the frequency difference ω_R where all other parameters are kept fixed. If we adjust τ to be the π pulse duration for distinct carrier or sideband transitions, we will observe dips in the lower-state population. Their abscissa (frequency difference ω_R) will provide us with the frequency of the transitions, see fig. 9.1b.

Depending on the geometric configuration of the laser beams we will be able to measure different Raman Rabi frequencies corresponding to different transitions.

For all experiments we will have to consider the frequency resolution of the two-photon stimulated Raman transitions. A quick estimation (properties of the Fourier transformation) yields

$$\Delta\omega_R \approx 1/\tau. \tag{9.1}$$

Now assume that we want to drive a Rabi flopping until a particular oscillation phase $\theta \in [0, \inf)$ has been reached. The duration τ it takes to do this can be modified by appropriately adjusting the Raman Rabi frequency $\Omega_R \to \theta/\tau$ which in turn is determined by the intensities of the two Raman beams, see eq. (2.3). That way, the frequency resolution can be adapted to the experimental requirements even for a constant phase θ.

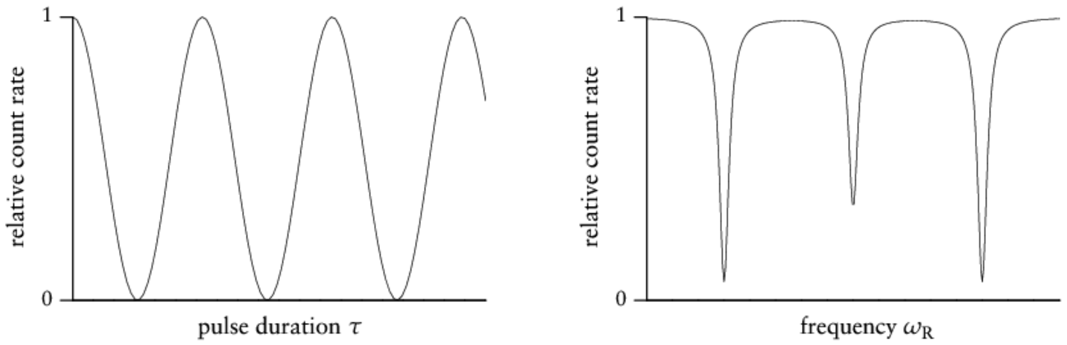

(a) Rabi flopping in dependence of the pulse duration.

(b) Rabi flopping in dependence of the frequency difference between the two Raman laser beams.

Figure 9.1.: Sample plots of ideal Rabi flopping curves.

9.1. Common steps of a flopping experiment

We prepared a single ion in the experimentation region of the trap confined in a radial potential of $\omega_{\text{radial}} \approx 2\pi \cdot 6\,\text{MHz}$ and an axial potential of $\omega_{\text{axial}} \approx 2\pi \cdot 2\,\text{MHz}$. The magnetic quantisation field of about 5.6 G was aligned to the propagation direction of the BD beam (maximising the fluorescent scattering rate by adjusting the respective currents flowing through the two spatial compensation coils). This allows for optimising the σ^+ polarisation of the BD beam by turning and tilting the $\lambda/4$ waveplate in front of port H (see fig. 4.2). Micromotion was compensated using a correlation method (section 8.2.3). At the usual operating characteristics for the BD beam (tab. 4.4) we observed a PMT count rate of around 210 kHz.

For each set of parameters $(\Delta\omega, \tau)$ we ran a pulse programme consisting of

1. Doppler cooling. Both the BD and the BD detuned beams were enabled during a period of 2 ms.
2. Two-photon stimulated Raman pulse. The frequency difference $\Delta\omega$ or the pulse duration τ of the two Raman beams could be varied. The detuning Δ_R of the virtual Raman level with respect to the $3P_{3/2}$ level was 80 GHz.
3. Detection pulse. With the BD detuned beam switched off, the BD beam was engaged for 20 µs. The resulting fluorescent scattering rate was measured using the PMT.

The detection step of the pulse programme will either yield “bright” (scattering photons) or “dark” (scattering no photons) depending on whether the qubit state eventually collapses to $|{\downarrow}\rangle$ or $|{\uparrow}\rangle$. We will have to conduct a statistical analysis in order to be able to make a statement on superposition states. Repeating the pulse programme 100 to 1000 times for each set of parameters $(\Delta\omega, \tau)$ provides sufficient data for this purpose.

9.2. “Hot” flopping using co-propagating Raman beams

As we saw in section 2.4.1, the easiest way to observe Rabi oscillations induced by a two-photon stimulated Raman transition is to use parallel laser beams. For this geometry the Raman Rabi frequency does not depend on the motional state number n, i. e. the transfer of electronic population between $|{\downarrow}\rangle$ and $|{\uparrow}\rangle$ occurs with equal speeds for all motional states. We thus expect to completely deplete the $|{\downarrow}\rangle$ state for an ion initially in the $|{\downarrow}\rangle$ state if we apply an adequate π-pulse. Subsequent state detection using the BD laser should not scatter any photons. As the experimental result does not depend on the particular occupation of the motional states, this type of experiments is ideally suited to conduct first flopping experiments after Doppler precooling (section 2.6.1). We use the B1 and R1 beams (see fig. 4.2 for the beam nomenclature) for the co-propagating geometry. For the experiments described below we worked with the following beam parameters: $I_{\mathrm{B1}} = 2.9 \cdot 10^5\,\mathrm{mW} \cdot \mathrm{cm}^{-2}$, $I_{\mathrm{R1}} = 6.0 \cdot 10^5\,\mathrm{mW} \cdot \mathrm{cm}^{-2}$, $\Delta_R = 2\pi \cdot 80\,\mathrm{GHz}$.

9.2.1. Frequency scan

For a fixed pulse time $\tau_\pi = 5.8\,\mu\mathrm{s}$ we scanned the frequency difference ω_R of the two Raman beams, see fig. 9.2. We can clearly identify the dip in the fluorescence rate at $\omega_R = 1775.28\,\mathrm{MHz}$ which represents the carrier flopping frequency for the transition $|{\downarrow}, n\rangle \to |{\uparrow}, n\rangle$. The width $\Delta\omega_R \approx 0.14\,\mathrm{MHz}$ fits our expectations from eq. (9.1) within an uncertainty of 5%. For the detection period of $20\,\mu\mathrm{s}$ the contrast (= depth of the dip in relation to the overall signal height) exceeds 93%. The fitted curve of fig. 9.2 should have a Lorentzian shape arising from the fact that the pulse time is limited. We however found that a Gaussian fitted the data better than a Lorentzian. One possible reason might be modulations of the Raman Rabi frequency Ω_R during the experimentation (see also the next section). These cause an actually Lorentzian-shaped line to broaden to a Gaussian shape.

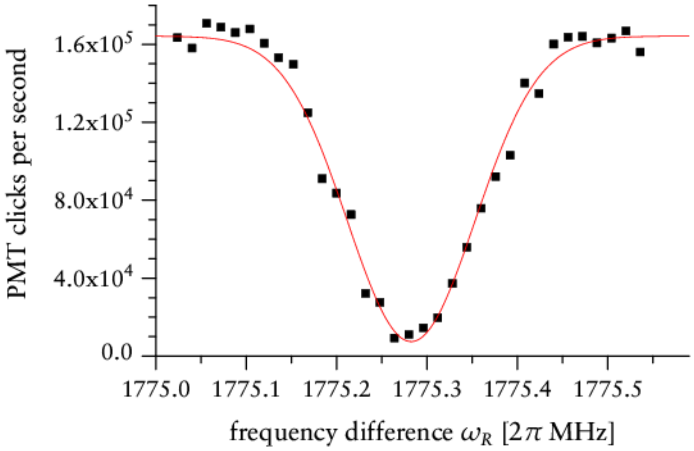

Figure 9.2.: Frequency scan for a co-propagating geometry. Note that the fitted curve is not Lorentzian but Gaussian (see main text for possible reasons).

9.2.2. Duration scan

For the two-photon stimulated Raman pulse (step 2 of our pulse programme) we used the co-propagating B1 and R1 beams (see fig. 4.2 for the beam nomenclature). The carrier Rabi flopping data are plotted in fig. 9.3. Note that the actual flopping begins at $\tau = 1.2\,\mu\text{s}$, which can be attributed to an imperfect synchronisation of the B1 and R1 beams. Apparently, the two beams do not overlap temporally for $\tau < 1.2\,\mu\text{s}$. (This effect will be suppressed in future experiments by appropriately adjusting the pulse control output.) Therefore, the actual π pulse duration τ_π is not given by the τ coordinate where the flopping curve passes its first minimum. A better method is to measure the duration between two subsequent flopping curve minima and divide the difference by two. We thus estimate $\tau_\pi = 2.47\,\mu\text{s}$.

The flopping contrast continuously decreases, but eventually experiences a revival after $\tau = 70\,\mu\text{s}$. We explain this beating signal as follows: Each data point in the plot is the average of 500 identical experiments. Assume that the Raman Rabi frequency Ω_R is not absolutely constant over time, but fluctuates slightly from experiment to experiment with ϵ being the maximum deviation from Ω_R. Further assume that these deviations are all equally probable. As the Rabi flopping for the $|{\downarrow}\rangle$ population ρ_{aa} at a constant Raman Rabi frequency is described by

$$\rho_{aa,\Omega_R}(t) = \frac{1}{2}\,(1 + \cos\Omega_R t) \tag{9.2}$$

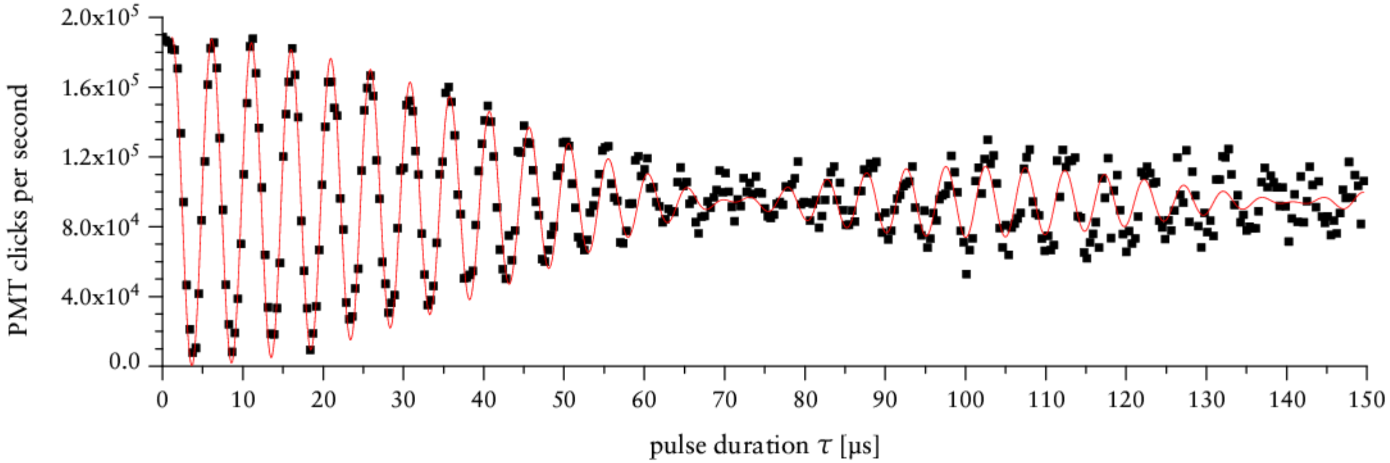

Figure 9.3.: Flopping curve for the co-propagating Raman beam geometry. Due to imperfect temporal overlap of the two Raman beams the flopping begins at $\tau = 1.2\,\mu\mathrm{s}$ instead of zero. The beating structure can be attributed to an unstable Raman Rabi frequency that shows a maximum deviation of $\pm 2\pi \cdot 7\,\mathrm{kHz}$ from the central Raman Rabi frequency $\Omega_R = 2\pi \cdot 202\,\mathrm{kHz}$. See the main text for possible reasons and remedies to this unstability.

we expect the averaged curve fitted to the acquired data to satisfy

$$\begin{aligned}\rho_{aa}(t) &= \frac{1}{2\epsilon}\int\limits_{-\epsilon}^{\epsilon} \rho_{aa,\Omega_R+\xi}(t)\mathrm{d}\xi \\ &= \frac{1}{2}\left(1+\frac{\sin\epsilon t}{\epsilon t}\cos\Omega_R t\right).\end{aligned} \tag{9.3}$$

Fig. 9.3 shows the fit of this function to our data for a time offset of $\tau = 1.2\,\mu\mathrm{s}$ (for the same reasons noted above). According to eq. (9.3) we can identify the envelope frequency with the maximum deviation of the Raman Rabi frequency. From the fit parameters we deduce $\Omega_R \in [2\pi \cdot 195\,\mathrm{kHz} \mid 2\pi \cdot 209\,\mathrm{kHz}]$.

The fluctuations of the Raman Rabi frequency can most probably be attributed to two culprits introducing noise into our system:

- Raman beam intensity. The complex beam generation process (section 4.2) causes fluctuations of the beam intensity on the microsecond timescale by as much as 4% [16]. The Raman Rabi frequency fluctuations introduced hereby, see eq. (2.2), fit our measurements quite well. In the final experimental setup, we will use “noise eaters” in the Raman beamline that stabilise their intensity to ±1% at the cost of reducing overall beam power.
- Magnetic quantisation field. Due to various line-powered electric devices in the vicinity of our trap the strength of the magnetic field at the trap centre will probably oscillate with the line frequency (50 Hz). Perturbations might also be caused by external electromagnetic fields at higher frequencies. The effects are different Zeeman shifts on the one hand and a tilt of the quantisation axis on the other. The former will effectively detune the two-photon stimulated Raman process from the $|\downarrow\rangle \leftrightarrow |\uparrow\rangle$ transition thereby altering the Raman Rabi frequency, see eq. (1.4). The latter in contrast causes imperfect polarisations of the Raman beams (a second order effect). Thus, only a fraction of their overall intensity will contribute to driving the two-photon stimulated Raman transition—with the same consequences as outlined above. We expect to considerably decrease the magnetic field noise by putting into operation the temporal compensation coil together with its associated electronics, see section 3.4.3.

9.3. “Hot” flopping using perpendicular Raman beams

For two Raman beams propagating perpendicularly to each other all Raman Rabi frequencies depend on the motional state number n. This is even true for the carrier pulse $|\downarrow, n\rangle \leftrightarrow |\uparrow, n\rangle$. Observation of flopping for the population not residing in the motional ground state will thus not be as clear as in the co-propagating case. As an additional feature of the perpendicular geometry however we will be able to drive sideband transitions $|\downarrow, n\rangle \leftrightarrow |\uparrow, n \pm 1\rangle$. This is the most important ingredient for resolved-sideband cooling, see section 2.6.2. In our setup, the orthogonal Raman beams are B1 and R2 (see fig. 4.2 for the beam nomenclature). For the experiments described in the following sections, we used the following laser beam parameters: $I_{\mathrm{B1}} = 2.9 \cdot 10^5\,\mathrm{mW} \cdot \mathrm{cm}^{-2}$, $I_{\mathrm{R2}} = 6.0 \cdot 10^5\,\mathrm{mW} \cdot \mathrm{cm}^{-2}$, $\Delta_R = 2\pi \cdot 80\,\mathrm{GHz}$.

9.3.1. Frequency scan

At π pulse duration that was 5 times as long as in the co-propagating case we could clearly resolve the carrier as well as the first red and the first blue sideband in a frequency scan, see fig. 9.4. For our Lamb-Dicke parameter of $\eta \approx 0.3$ eq. (2.7) suggests a π pulse duration of only 3.5 times the co-propagating π pulse duration. This mismatch was probably caused by a reduced R2 laser beam intensity due to a non-optimal overlap with the ion.

We can estimate the temperature of our ion from the relative contrast of the sideband dips (= difference of the fluorescence rates) in the frequency scan. Due to the fact that we cannot drive a first red sideband transition of the motional level $n = 0$ (there is no lower motional level), the contrast for the red sideband dip will be smaller than for the blue sideband dip (where we can drive transitions for any motional level). The mean motional quantum number can be estimated by comparing the depths of the first red and the blue sideband dips A_{rsb}, A_{bsb}. According to [49] we have

$$\overline{n} = \frac{r}{1 - r} \tag{9.4}$$

where $r = A_{\mathrm{rsb}}/A_{\mathrm{bsb}}$. Although the fits of fig. 9.4 could be improved by measuring the dips in more dense intervals, there is evidence that $\overline{n} \approx 15$. Assumed that the motional spectrum is thermal, we deduce $T \approx 1.5\,\mathrm{mK}$.

The spacing between the carrier frequency and the sideband frequencies is determined by the frequency of the motional quanta coupled to the electronic qubit states.

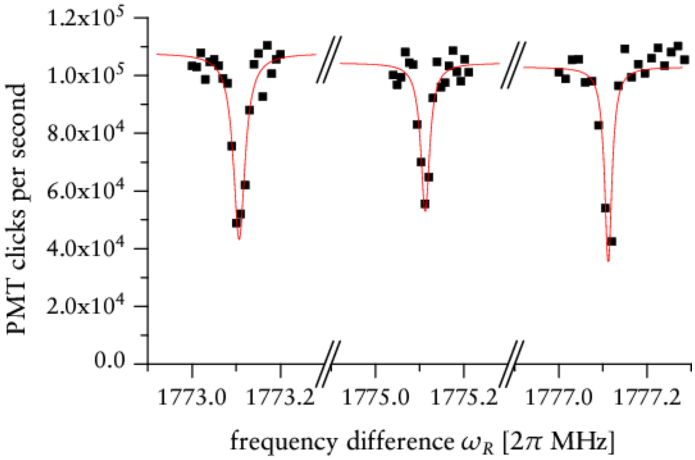

Figure 9.4.: Frequency scan for perpendicular Raman beams. The π pulse duration τ_π was adjusted at 5 times the π pulse duration of the co-propagating case. Note that the abscissa is segmented into three regions each displaying (from left to right): first red sideband transition, carrier transition, and first blue sideband transition. The contrast of the blue sideband dip is increased compared to the red sideband dip as the red sideband transition cannot be driven for the motional state $n = 0$. The carrier dip appears suppressed; a different pulse duration is necessary to drive the associated transition at a higher fidelity.

From fig. 9.4 we evaluate $\omega_z = 2\pi \cdot 2.00\,\mathrm{MHz}$. The voltages of the experimentation region subelectrodes D, E, and F were 10 V, −30 V, and 10 V each. For these values, the axial frequency estimated using eq. (3.4) matches our measurement within a tolerance of 0.1%.

9.3.2. Duration scan

Unless the ion's motion has been cooled to its ground state, flopping curves for an orthogonal geometry will quickly "wash out" due to the superposition of the different Raman Rabi frequencies involved. We calculated the expected flopping curves of the carrier and the first red sideband for an ion in our trap Doppler-cooled to different temperatures T_D, see fig. 9.5.

Experimental data of our measurements is plotted in fig. 9.6. The pulse durations of the calculated and experimental data differ by a factor of about 4. This is possibly caused by a misaligned R2 beam, but was still under investigation at the printing time

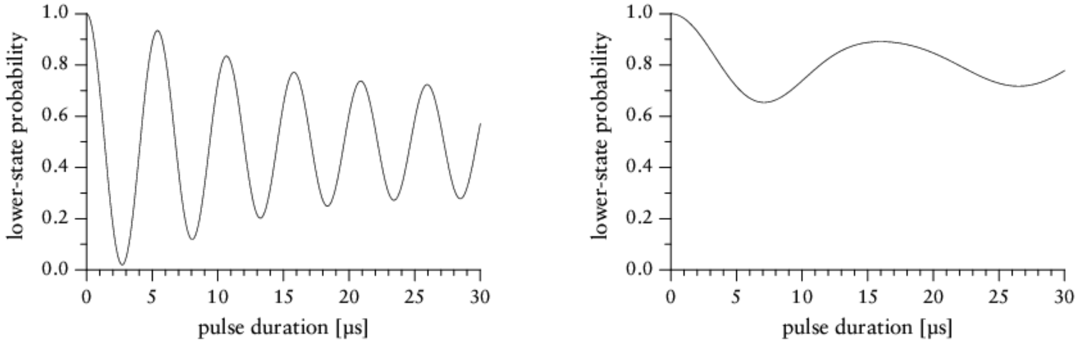

(a) Carrier flopping curve for $T = 0.1\,\mathrm{mK}$.

(b) First red sideband flopping curve for $T = 0.1\,\mathrm{mK}$.

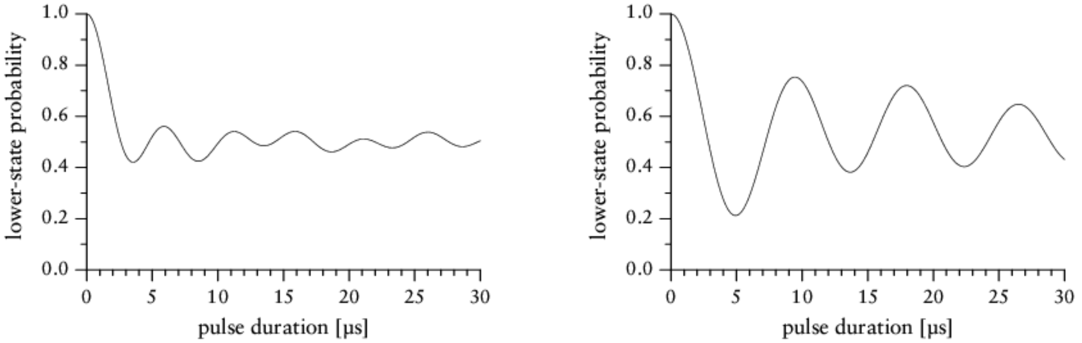

(c) Carrier flopping curve for $T = 1\,\mathrm{mK}$.

(d) First red sideband flopping curve for $T = 1\,\mathrm{mK}$.

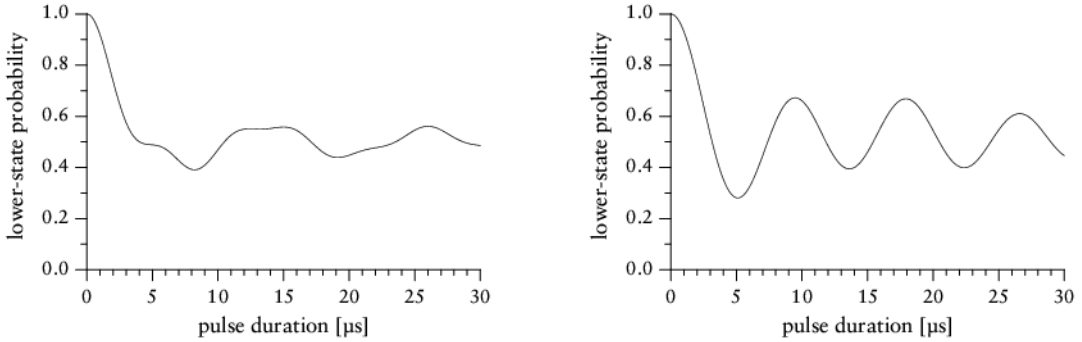

(e) Carrier flopping curve for $T = 2\,\mathrm{mK}$.

(f) First red sideband flopping curve for $T = 2\,\mathrm{mK}$.

Figure 9.5.: Simulated flopping curves for the electronic population in the $|\downarrow\rangle$ state using perpendicular Raman beams for the two-photon stimulated Raman transitions at an axial confinement of $\omega_{\mathrm{axial}} = 2\pi \cdot 2\,\mathrm{MHz}$ ($\eta = 0.3$), a "base" Raman Rabi frequency of $\Omega_R = 2\pi \cdot 202\,\mathrm{kHz}$, and an ion temperature of $T_D = 1\,\mathrm{mK}$.

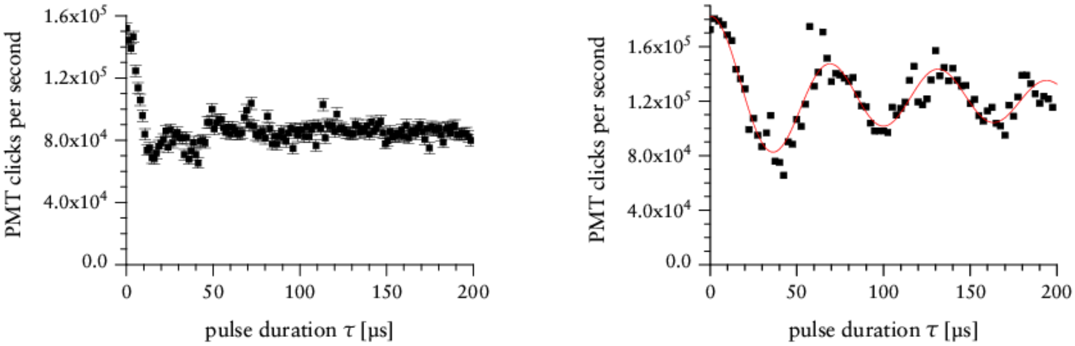

(a) Carrier flopping curve.

(b) First red sideband flopping curve.

Figure 9.6.: Actually measured flopping curves using perpendicular Raman beams for the two-photon stimulated Raman transitions at an axial confinement of $\omega_{\text{axial}} = 2\pi \cdot 2\,\text{MHz}$ ($\eta = 0.3$). The "base" Raman Rabi frequency had been measured in a prior co-propagating Rabi flopping timescan to be $\Omega_R = 2\pi \cdot 202\,\text{kHz}$ (see section 2.5 for further explanations on the "base" frequency). We were unable to provide a good fit to the carrier flopping data. Still, we can see that the pulse durations of the calculated (fig. 9.5) and experimental data are rather different. Possibly, the redder Raman beam R2 was not properly aligned thus providing less intensity and decreasing the Raman Rabi frequency.

of this thesis. Even so, we can see that the characteristics of the curves closely resemble the calculated curves for $T = 1\,\text{mK}$.

9.4. Shelving

As noted in section 2.3 we might off-resonantly scatter photons from the $|\uparrow\rangle$ state when the BD detection beam is engaged. This process eventually pumps $|\uparrow\rangle$ into the $|\downarrow\rangle$ state thereby unwantedly scattering many photons within the cycling transition. We suppose to weaken this effect by applying additional shelving pulses before actual readout occurs. The shelving pulses are two-photon stimulated Raman transitions which will transfer population from $|\uparrow\rangle$ into states of the $3S_{1/2}$ manifold with a smaller m_F value, see fig. 9.7.

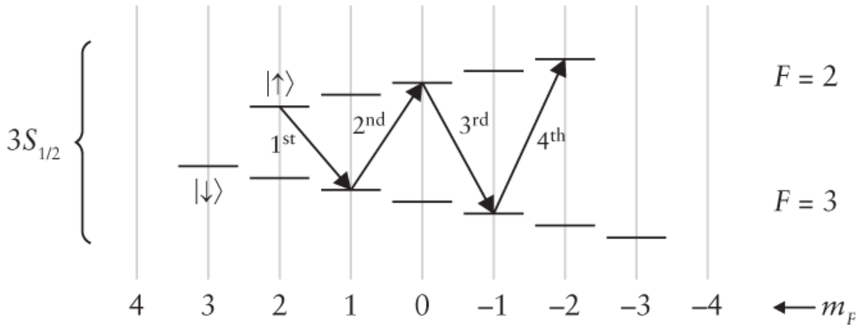

Figure 9.7.: Shelving pulses inside the $3S_{1/2}$ manifold. Each shelving transition is provided via a two-photon stimulated Raman pulse. As the two Raman beams are polarised π (bluer beam) and σ^+ (redder beam), the population will be shifted by $\Delta m_F = -1$ with each pulse.

We may also use this technique to determine the actual magnetic field strength at the trap centre by measuring the Zeeman shifts of the involved states. The Zeeman shifts can be calculated as follows:

$$\Delta\omega = m_F g_F \mu_B B \,/\, \hbar \tag{9.5}$$

where g_F is the Landé factor ($+1/3$ for $3S_{1/2}\,|F=3\rangle$, $-1/3$ for $3S_{1/2}\,|F=2\rangle$), μ_B is the Bohr magneton and B is the strength of the magnetic field. Thus, the ith shelving pulse frequency ω_i, i. e. the frequency difference of the two Raman beams providing the ith shelving pulse, is determined by

$$\omega_i = \omega_0 + \frac{2i-5}{3}\mu_B B \,/\, \hbar \tag{9.6}$$

where ω_0 indicates the hyperfine splitting of the $3S_{1/2}$ manifold. With a current of $I = 6.000\,\mathrm{A}$ flowing through the field-generating coils of section 3.4 we measured $\omega_1 = 1781.02\,\mathrm{MHz}$, $\omega_2 = 1786.24\,\mathrm{GHz}$, which yields $B = 5.589(15)\,\mathrm{G}$ and $\omega_0 = 1788.850(15)\,\mathrm{MHz}$. This result differs from the calculated field strength by about 44% (see section 3.4).

9.5. Cooling to the motional ground state

We extended the pulse programme to include a step of resolved-sideband cooling right after having Doppler-cooled the ion. It consisted of sideband-cooling and repumping

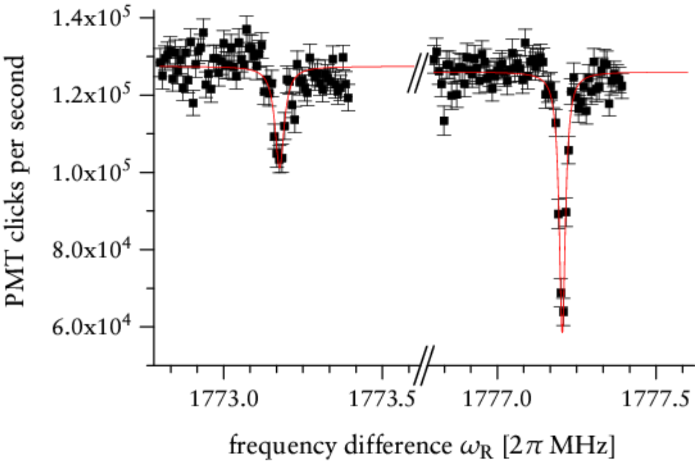

Figure 9.8.: Sideband dips of a frequency scan using an orthogonal Raman beam geometry at a π pulse duration of $\tau_\pi = 40\,\mu\text{s}$. Compared to fig. 9.4 we included an additional step of resolved-sideband cooling in the pulse programme. This reduced the contrast of the first red sideband dip. From the ratio of the dip depths we estimate $\overline{n} = 0.65$.

cycles $|{\downarrow}, n\rangle \rightarrow |{\downarrow}, n-1\rangle$ for $n = 30 \ldots 1$ where each cooling cycle was run twice in succession.

At a π pulse duration of $\tau_\pi = 40\,\mu\text{s}$ we observed a substantial decrease in contrast of the first red sideband, see fig. 9.8. The mean motional quantum number calculated according to eq. (9.4) is $\overline{n} = 0.65$. Assumed that the occupation of motional states resembles a thermal distribution, this corresponds to a sideband-cooled temperature of $T_{\text{SB}} = 0.1\,\text{mK}$ which means that more than 60% of the population are in the motional ground state $n = 0$.

Note that this estimation is not valid for the entire population. Part of the population was "lost" in the $3S_{1/2}\,|F = 3, m_F = 2\rangle$ state (see fig. 9.9) due to an unreliable repumper beam during the cooling process (RD was present though!). It is however correct for the portion of the population that was successfully transferred into the $|{\downarrow}\rangle$ state.

In the case of ground-state cooled ions, we have a predominant contribution of the motional state $n = 0$ to the overall distribution of motional levels. Thus, flopping curves will not wash out even if we use an orthogonal Raman beam geometry. See fig. 9.9 for the graphs of a carrier and a first blue sideband flopping curve. As flopping

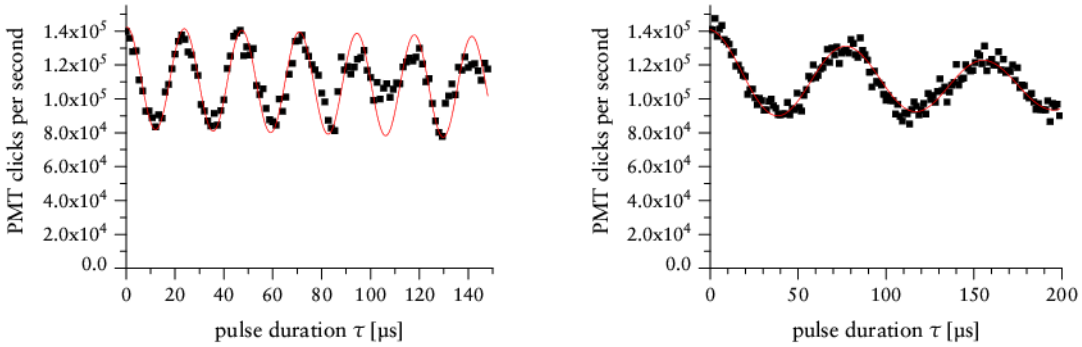

(a) Carrier flopping curve. (b) First blue sideband flopping curve.

Figure 9.9.: Flopping curves for a ground-state cooled ion using an orthogonal Raman beam geometry. Although the fit for the carrier flopping curve might be too optimistic, there is a clear difference to the curves of fig. 9.6. The ratio of the two Raman Rabi frequencies (determined from the respective π pulse durations) is 0.3 in good accordance with the expected ratio of η. See the main text for reasons on the low contrast.

of the post-selected population in the $|\downarrow\rangle$ is now mainly determined by the $n = 0$ state, we expect from eq. (2.7) that the ratio of the respective π pulse durations is given by

$$\frac{\tau_{\pi,\text{carrier}}}{\tau_{\pi,\text{bsb}}} \approx \eta \tag{9.7}$$

in very good accordance with the ratio determined from the graphs. The flopping curves have a maximum contrast of 40% which differs substantially from the expected near-100%. As mentioned before, the reason is an unreliably applied repumper beam. A considerable amount of population will not have been shifted into the $|\downarrow\rangle$ state after resolved-sideband cooling thus causing a loss of contrast. We expect to attain a contrast close to 100% for future measurements involving a reliable repumper beam.

Appendix

A. Auge visualisation and data acquisition software

The *Auge* software has been written in C++ in order to facilitate inspection and maintenance and at the same time maximise the programme's execution speed. As we are dealing with large amounts of data (up to 9 MB/s) efficient data handling becomes important. Fig. A.1 summarises the interaction and data flow between the particular objects.

We may assign each object to one of the three application layers. These are: background logic (= business logic), user interface logic, and network logic. The background logic layer deals with the acquisition, storage, processing, accession, and analysis of data, the user interface layer presents these data on screen and provides user feedback, while the network layer provides a bidirectional communication facility with our control software *Flocke*.

As a Windows (Win32) application *Auge* continously runs an event loop thus polling and reacting on Windows or user events. In parallel, it runs an infinitely looping thread that unintermittently reads out newly available camera data. These two threads have to be synchronised on the following occasions:

- When readout parameters are changed. This ensures that possible memory allocation / deallocation processes are carried out properly.
- When camera acquisition is started / stopped. This ensures that an acquisition in progress is not cancelled.

DataController as the main object for data accession and processing is used as a synchronising mutex object.

Where function user interface objects call of methods of background logic objects, these calls occur directly. The other way round, function calls occur indirectly: User interface objects have to register themselves as listeners for events originating from background logic objects. The philosophy behind this approach is to anchor a scheme within the design of the software that reflects the user's control.

Ownership of the involved objects is arranged in a somewhat simpler way, see fig. A.2. Eventually, all objects are owned by the *MainWindow*. If the *MainWindow* is destroyed, i. e. when the application quits, all other objects will thus be disposed of automatically.

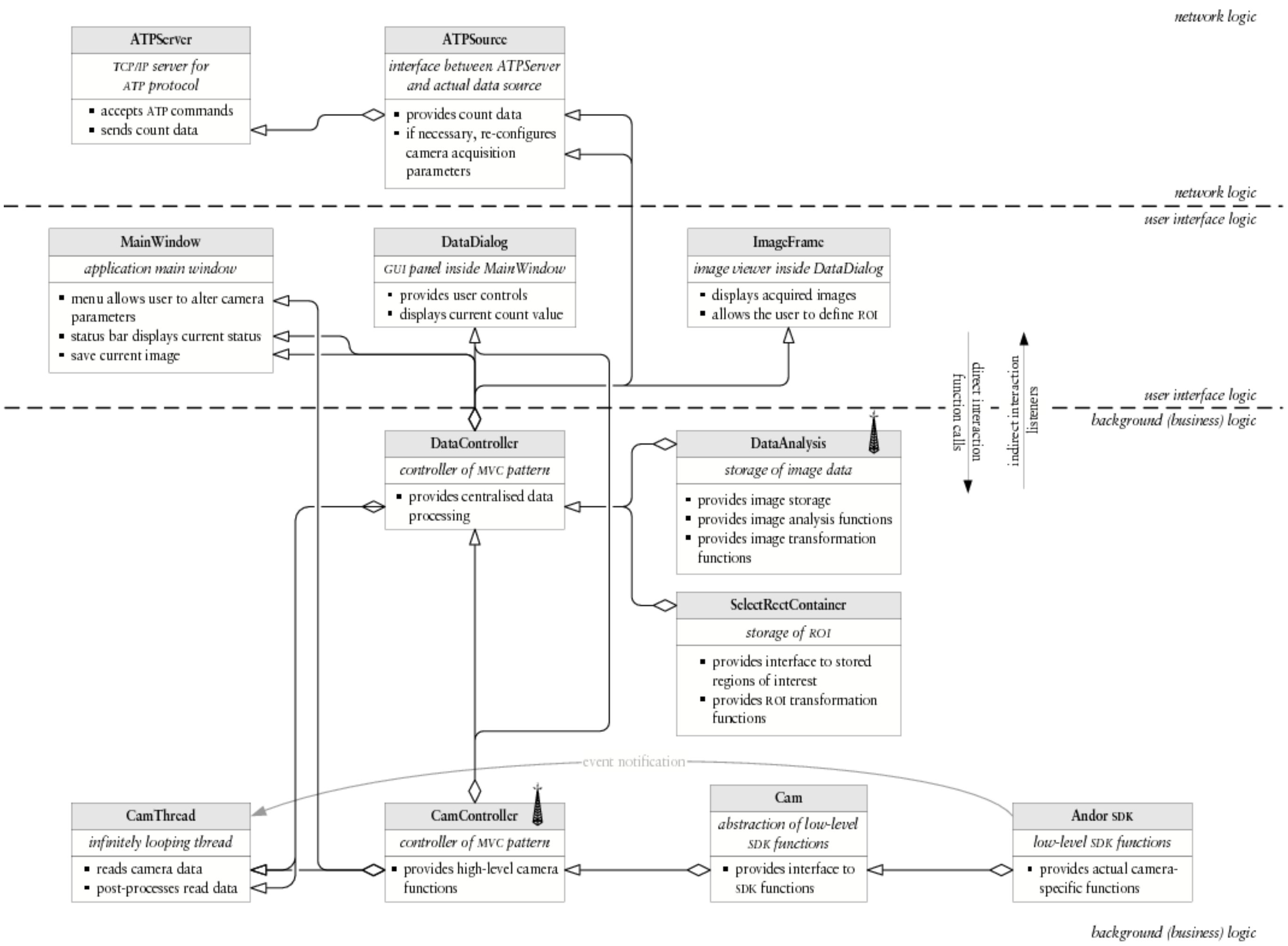
network logic
ATPServer
TCP/IP server for ATP protocol
accepts ATP commands
sends count data
ATPSource
interface between ATPServer and actual data source
provides count data
if necessary, re-configures camera acquisition parameters
network logic
user interface logic
MainWindow
application main window
menu allows user to alter camera parameters
status bar displays current status
save current image
DataDialog
GUI panel inside MainWindow
provides user controls
displays current count value
ImageFrame
image viewer inside DataDialog
displays acquired images
allows the user to define ROI
direct interaction
function calls
indirect interaction
listeners
user interface logic
background (business) logic
DataController
controller of MVC pattern
provides centralised data processing
DataAnalysis
storage of image data
provides image storage
provides image analysis functions
provides image transformation functions
SelectRectContainer
storage of ROI
provides interface to stored regions of interest
provides ROI transformation functions
event notification
CamThread
infinitely looping thread
reads camera data
post-processes read data
CamController
controller of MVC pattern
provides high-level camera functions
Cam
abstraction of low-level SDK functions
provides interface to SDK functions
Andor SDK
low-level SDK functions
provides actual camera-specific functions
background (business) logic

Figure A.1.: Interaction between the particular objects of *Auge*. Arrows with transparent heads indicate the direction of data flow. The radio masts indicate event sources that user interface logic objects can register with.

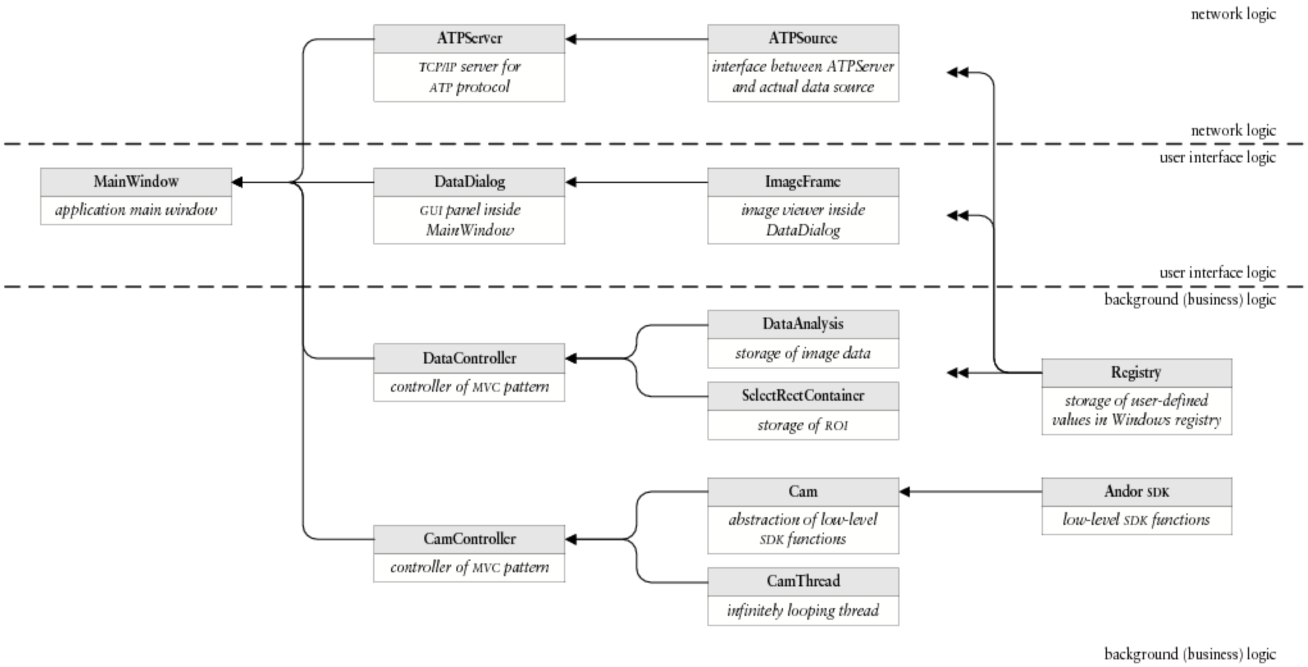
network logic
ATPServer
TCP/IP server for ATP protocol
ATPSource
interface between ATPServer and actual data source
network logic
user interface logic
MainWindow
application main window
DataDialog
GUI panel inside MainWindow
ImageFrame
image viewer inside DataDialog
user interface logic
background (business) logic
DataAnalysis
storage of image data
DataController
controller of MVC pattern
SelectRectContainer
storage of ROI
Registry
storage of user-defined values in Windows registry
Cam
abstraction of low-level SDK functions
Andor SDK
low-level SDK functions
CamController
controller of MVC pattern
CamThread
infinitely looping thread
background (business) logic

Figure A.2.: Ownership of the particular objects of *Auge*. The *Registry* object follows the Singleton pattern and can as such not be assigned to a particular owner.

B. Auge Transfer Protocol (ATP)

The Auge Transfer Protocol (ATP) defines a communication interface between our visualisation and data acquisition software *Auge* and an analysis software (which can be arbitrary as long as it keeps to the rules defined in this section). In the framework of this protocol *Auge* provides count rates (confined to previously defined elliptically shaped regions of interest, ROI) which can in turn be read by the analysis software.

Auge provides the data as a TCP/IP server. Normally, the server will run on port 1899. The analysis software connects to *Auge* as required and directs commands to *Auge*. These commands will instantaneously be processed and replied to where the replies follow an HTTP-like scheme[*].

B.1. Typical course of an ATP connection

	Client		Server
0.		⟵	Status
1.	command `CT`	⟶	
		⟵	reply `CT`
2.	command `START`	⟶	
		⟵	reply `START`
3.	command `STOP`	⟶	
		⟵	reply `STOP`
4.	command `QUIT`	⟶	
		⟵	reply `QUIT`

---

[*] http://www.faqs.org/rfcs/rfc2616.html

reply code	description
100 – 199	status notifications
200 – 299	replies containing numerical values
300 – 399	replies containing binary data in their data block
400 – 499	error messages

Table B.1.: Reply code families.

B.2. Reply and status codes

A reply consists of a header and a data block where the header is compulsory. The data block may be omitted depending on the type of reply. Header and data block are separated from each other by CRLF. The syntax of the header is

```
nnn xxxxx
```

where `nnn` is the answer code expressed as a three-digit decimal integer number and `xxxx` contains a textual representation of the reply. Each reply code can be assigned to a family, see tab. B.1. The reply data block may contain arbitrary data and does not follow a predefined formatting scheme.

B.3. Commands and their replies

B.3.1. Error replies

Error replies can be sent any time during an ATP connection. Two error codes are defined:

`400` `syntax error`

The command directed at the server contains a syntax error.

`401` `unknown error`

An unknown error has occurred.

B.3.2. Start of an ATP connection

Upon the start of an ATP connection the ATP server will provide the client with a status code that signifies the current status of the server. Possible status codes are:

`100` `ready`

Auge is ready to accept commands.

`101` `busy`

Auge cannot process and commands. The ATP connection is closed immediately after this message.

`102` `no data available`

Auge cannot provide any data. The ATP connection is closed immediately after this message.

B.3.3. The `CT` command (Cycle Time)

With the `CT` command the client tells *Auge* what maximum timespan it expects between subsequent acquisitions of the CCD camera. This *must* be the first command of any ATP connection. The syntax is

```
CT f
```

where `f` is the duration between subsequent acquisitions in seconds. It must be formatted as a decimal number with the period (`.`) as a decimal separator.
Possible reply codes:

`200` `n`

`n` is the number of acquisitions per readout process. The client must ensure that the total number of acquisitions equals an integer multiple of `n`.

`402` `desired cycle time cannot be achieved`

The camera cannot deliver data with the desired speed.

B.3.4. The `ET` command (Exposure Time)

With the `ET` command the client tells *Auge* to determine and return the current exposure time of the CCD camera. This command is *always* valid. The syntax is

```
ET
```

Possible reply codes:

`201 f`

`f` is the exposure time of the CCD camera in seconds. It is formatted as a decimal number with the period (`.`) as a decimal separator.

B.3.5. The `TM` command (Trigger Mode)

With the `TM` command the client tells *Auge* to open or close the camera shutter. This command cannot be executed prior to a successfully executed `CT` command. The syntax is

```
TM n
```

where `n` is `1` if the shutter should be opened and `0` otherwise.
Possible reply codes:

`100 okay`

The shutter state has been set successfully.

B.3.6. The `START` command

With the `START` command the client tells *Auge* to transmit measurement data. This command cannot be executed prior to a successfully executed `CT` command. The syntax is

```
START
```

Possible reply codes:

`300 here we go`

The data block of this reply contains the count rates within the regions of interest defined by the experimentator. See below for the formatting of the data.

B.3.7. The `STOP` command

With the `STOP` command the client tells *Auge* to cancel the transmission of measurement data. This command cannot be executed prior to a `START` command. The syntax is

```
STOP
```

Possible reply codes:

`100 ready`

The transmission has been cancelled.

B.3.8. The `QUIT` command

With the `QUIT` command the client tells *Auge* to close the ATP connection. This command is *always* valid. The syntax is

```
QUIT
```

Possible reply codes:

`199 bye`

The ATP connection is being closed.

B.3.9. Formatting of the transferred count rate data

The count rate values for the defined regions of interest (ROI) are transmitted sequentially. The data for each ROI encompasses five bytes $b_1 \cdots b_5$. The first byte b_1 contains the ROI index. If the ROI is focused during readout, the highest (most significant) bit of b_1 will be set. The following bytes $b_2 \cdots b_5$ contain the respective count rate as a 32-bit long integer in network byte order (Big Endian).

C. Paulbox C compiler

The Paulbox compiler translates a pulse programme written in a human-readable language into binary code which can subsequently be sent to the Paul box. A pulse programme consists of lines separated by a CRLF character sequence. Each line contains tokens which may be separated by whitespace characters (spaces and tabs).

C.1. General notes

C.1.1. Arithmetics

Integer numbers can be specified using either an octal (prefix `0`), decimal, or hexadecimal (prefix `0x`) notation. Rational numbers must be specified using the decimal notation with the period (`.`) as a decimal separator. An integer part of zero may be omitted.

The compiler supports simple arithmetic operations: summation (`+`), subtraction (`-`), multiplication (`*`), division (`/`), and association using parentheses. `pi` (the circle number) is recognised as a special constant.

C.1.2. Comments

Comments begin with the number sign (`#`) and reach to the end of line.

C.2. Syntax

C.2.1. TTL control

```
ttlX = Y
```

where `X` is the index of the TTL output expressed as a decimal number between 0 and 15 without leading zeroes and `Y` is the desired TTL value—`0` encodes LO and `1` encodes HI.

C.2.2. DAC control

```
dacX = Y
```

where `X` is the index of the DAC expressed as a decimal number between 0 and 3 and `Y` is a rational number between 0 and 1.

C.2.3. DDS control

The four DDS boards each use four internal profiles which can be independently written. Each profile contains a frequency register and a phase register. Note that a call to `ddsX.update()` is needed to force the DDS boards to output the currently set register values.

Writing frequency registers

```
ddsX.profileY.frequency = Z
```

where `X` is the index of the DDS board expressed as a decimal number between 0 and 3, `Y` is the profile index expressed as a decimal number between 0 and 3, and `Z` is the desired frequency in megahertz expressed as a rational number.

It is also possible to use the shortcut

```
ddsX.frequency = Z
```

as an equivalent to `ddsX.profile0.frequency = Z`.

Writing phase registers

```
ddsX.profileY.phase = Z
```

where `X` is the index of the DDS board expressed as a decimal number between 0 and 3, `Y` is the profile index expressed as a decimal number between 0 and 3, and `Z` is the desired phase in rad expressed as a rational number.

It is also possible to use the shortcut

```
ddsX.phase = Z
```

as an equivalent to `ddsX.profile0.phase = Z`.

Setting the active profile

```
ddsX.profile = Y
```

where `X` is the index of the DDS board expressed as a decimal number between 0 and 3 and `Y` is the index of the profile to be activated expressed as an integer number between 0 and 3.

Outputting the current register values

```
ddsX.update()
```

where `X` is the index of the DDS board expressed as a decimal number between 0 and 3 or “X”, in which case all four DDS boards are updated at the same time. *Note:* The parentheses *must* be supplied.

C.2.4. Pausing

```
wait X
```

where `X` is the duration that the Paul box should pause. It is either specified as the integer number of processor cycles (one cycle is 10 ns) or as a value in seconds. The latter specification consists of a number (integer or rational) followed by a time unit (`s`, `ms`, `us`, or `ns`). The unit specification may be separated from the value by one (1) space.

C.2.5. Triggering

```
wait triggerX
```

where `X` is the index of the TTL input that—if set to HI—will cause the program to continue. It must be a decimal number between 0 and 7 or “X”, in which case any set input TTL will cause the program to continue.

C.2.6. Looping

Infinite loops

```
loop { ··· }
```

The commands to be repeated are enclosed in curly brackets.

Finite loops

```
loop (X) { ··· }
```

where `X` is the number of iterations expressed as an integer number.

C.2.7. Subroutines

Subroutines are code blocks labelled with a unique identifier. They can be called from within the main programme using their identifier.

Definition of subroutines

```
sub X { ··· }
```

where `X` is the case-sensitive identifier of the subroutine. It must start with a letter (A – Z, a – z); the use of reserved words (`dds_update`) is forbidden.

Calling subroutines

```
X()
```

where `X` is the case-sensitive identifier of the subroutine to be called. The parentheses *must* be supplied. Note that a subroutine must be defined prior to calling it.

Bibliography

[1] Richard P. Feynman, *Simulating physics with computers*, International Journal of Theoretical Physics **21** (1982), 467.

[2] P. W. Shor, *Algorithms for quantum computation: Discrete logarithms and factoring*, Proceedings of the 35th Annual Symposium on the Foundations of Computer Science (S. Goldwasser, ed.), vol. 35, IEEE Computer Society, Los Alamitos, CA, 1994, p. 124.

[3] M. A. Nielsen and I. L. Chuang, *Quantum computation and quantum information*, 1st ed., Cambridge University Press, 2000.

[4] *ARDA roadmap*, 2004, http://qist.lanl.gov/.

[5] D. Porras and J. I. Cirac, *Effective quantum spin systems with trapped ions*, Physical Review Letters **92** (2004), 207901.

[6] L. J. Garay et al., *Sonic analog of gravitational black holes in Bose-Einstein condensates*, Physical Review Letters **85** (2000), 4643.

[7] L. Lamata et al., *Dirac equation and quantum relativistic effects in a single trapped ion*, 2007, arXiv:quant-ph/0701208.

[8] A. Bermudez, M. A. Martin-Delgado, and E. Solano, *Exact mapping of the 2+1 Dirac oscillator onto the Jaynes-Cummings model*, 2007, arXiv:0704.2315 [quant-ph].

[9] Ralf Schützhold et al., *Analogue of cosmological particle creation in an ion trap*, to be submitted, 2007.

[10] N. D. Birrell and P. C. W. Davies, *Quantum fields in curved space*, Cambridge University Press, 1986.

[11] Paul M. Alsing, Jonathan P. Dowling, and G. J. Milburn, *Ion trap simulations of quantum fields in an expanding universe*, Physical Review Letters **94** (2005), 220401.

[12] D. F. Walls, *Squeezed states of light*, Nature **306** (1983), 141.

[13] W. Schleich and J. A. Wheeler, *Oscillations in photon distribution of squeezed states*, Journal of the Optical Society of America B **4** (1987), 1715.

[14] J. I. Cirac and P. Zoller, *Quantum computations with cold trapped ions*, Physical Review Letters **74** (1995), 4091.

[15] D. J. Wineland et al., *Experimental issues in coherent quantum-state manipulation of trapped atomic ions*, Journal of Research of the National Institute of Standards and Technology **103** (1998), 259.

[16] A. Friedenauer et al., *High power all solid state laser system near 280 nm* , Applied Physics B **84** (2006), 371.

[17] Rodney Loudon, *The quantum theory of light*, 3rd ed., Oxford University Press, 2000.

[18] Marlan O. Scully and M. Suhail Zubairy, *Quantum Optics*, 1st ed., Cambridge University Press, 1997.

[19] Elizabeth Anne Curtis, *Quenched narrow-line laser cooling of* ^{40}Ca *with application to an optical clock based on ultracold neutral Ca atoms*, Ph.D. thesis, University of Colorado, 2003.

[20] Volker Hans Ludsteck, *Experimente mit einer linearen Ionenkette zur Realisierung eines Quantencomputers*, Ph.D. thesis, Ludwig-Maximilians-Universität München, 2004.

[21] T. W. Hänsch and A. L. Schawlow, *Cooling of gases by laser radiation*, Optics Communications **13** (1975), 68.

[22] D. J. Heinzen and D. J. Wineland, *Quantum-limited cooling and detection of radio-frequency oscillations by laser-cooled ions*, Physical Review A **42** (1990), 2977.

[23] David Kielpinski, *Entanglement and decoherence in a trapped-ion quantum register*, Ph.D. thesis, University of Colorado, 2001.

[24] Brian E. King, *Quantum state engineering and information processing with trapped ions*, Ph.D. thesis, University of Colorado, 1999.

[25] Bruce W. Shore and Peter L. Knight, *Topical review: The Jaynes-Cummings model*, Journal of Modern Optics **40** (1993), 1195.

[26] D. J. Wineland and Wayne M. Itano, *Laser cooling of atoms*, Physical Review A **20** (1979), 1521.

[27] F. Diedrich et al., *Laser cooling to the zero-point energy of motion*, Physical Review Letters **62** (1989), 403.

[28] C. Monroe et al., *Resolved-sideband raman cooling of a bound atom to the 3D zero-point energy*, Physical Review Letters **75** (1995), 4011.

[29] Wolfgang Paul, *Electromagnetic traps for charged and neutral particles*, Reviews of Modern Physics **62** (1990), 531.

[30] F. G. Major, V. N. Gheorghe, and G. Werth, *Charged particle traps*, Springer, 2005.

[31] S. Seidelin et al., *A microfabricated surface-electrode ion trap for scalable quantum information processing*, Physical Review Letters **96** (2006), 253003.

[32] N. Kjærgaard et al., *Isotope selective loading of an ion trap using resonance-enhanced two-photon ionization*, Applied Physics B **71** (2000), 207.

[33] D. N. Madsen and J. W. Thomsen, *Measurement of absolute photo-ionization cross sections using magnesium magneto-optical traps*, Journal of Physics B **35** (2002), 2173.

[34] T. W. Hänsch and B. Couillaud, *Laser frequency stabilization by polarization spectroscopy of a reflecting reference cavity*, Optics Communications **35** (1980), 441.

[35] S. Gerstenkorn and P. Luc, *Atlas du spectre d'absorption de la molécule d'iode entre 17 500 cm^{-1} – 20 000 cm^{-1}*, Centre National de la Recherche Scientifique, 1977.

[36] T. W. Hänsch, M. D. Levenson, and A. L. Schawlow, *Complete hyperfine structure of a molecular iodine line*, Physical Review Letters **26** (1971), 946.

[37] C. Wieman and T. W. Hänsch, *Doppler-free laser polarization spectroscopy*, Physical Review Letters **36** (1976), 1170.

[38] C. P. Pearman et al., *Polarization spectroscopy of a closed atomic transition: applications to laser frequency locking*, Journal of Physics B **35** (2002), 5141.

[39] Andor Technology plc, *Digital camera fundamentals*, March 2006.

[40] Paul Tan The Pham, *A general-purpose pulse sequencer for quantum computing*, Master's thesis, Massachusetts Institute of Technology, February 2005, http://downloads.sourceforge.net/pulse-sequencer/ppham-sequencer-thesis.pdf.

[41] Paul T. Pham, *Quantum computing pulse programmer – Technical manual*, MIT center for Bits and Atoms, June 2006, Version 0.30, http://downloads.sourceforge.net/pulse-sequencer/pulse-manual-0.30-a4.pdf.

[42] Python Software Foundation, *Python 2.5 documentation*, September 2006, http://docs.python.org/.

[43] J. Janszky and Y. Y. Yushin, *Squeezing via frequency jump*, Optics Communications **59** (1986), 151.

[44] Fan Hong-Yi and H. R. Zaidi, *Squeezing and frequency jump of a harmonic oscillator*, Physical Review A **37** (1988), 2985.

[45] D. M. Meekhof et al., *Generation of nonclassical motional states of a trapped atom*, Physical Review Letters **76** (1996), 1796.

[46] Enrique Solano, priv. comm.

[47] D. J. Berkeland et al., *Minimization of ion micromotion in a Paul trap*, Journal of Applied Physics **83** (1998), 5025.

[48] Tobias Schätz, *Kristalline Ionenstrahlen*, Ph.D. thesis, Ludwig-Maximilians-Universität München, 2001.

[49] D. Leibfried et al., *Quantum dynamics of single trapped ions*, Reviews of Modern Physics **75** (2003), 281.

Index

acousto-optical deflector, 52
acousto-optical modulator, 77
  driving power, 78
acquisition
  row-wise, 73
  statistics, 77, 105
adiabatic elimination, 17
ATP, *see* Auge Transfer Protocol
Auge software, **72**, 121
  thread, 121
Auge Transfer Protocol, 125
axial confinement, 32

beam steering, 51
Bloch equations, 3
  modulated, 94
Blue Doppler detuned, 54
  intensity, 54
Blue Doppler laser, 13
  intensity, 21
Blue Doppler transition, 14

CCD camera, 68
  interplay, 82
  signal-to-background, 69
compensation electrode, 34
confinement strength, 106
contrast, 107
count rate
  Auge, 125
  PMT, 106
cycling transition, 14

DDS, *see* Paul box direct digital synthesisers
detection switch box, 63
dispersive signal, 59
duration scan, 105
  ground-state cooled, 117
  orthogonal geometry, 112
  parallel geometry, 108
dye laser, 45

Einstein coefficients, 7
emission characteristics, 63

Flocke software, 82
fluxgate sensor, 42
frequency scan, 105
  ground-state cooled, 116
  orthogonal geometry, 111
  parallel geometry, 107

heating rate, 33
hyperfine levels, 11

ion gauge, 34

Jäger box, 82

Lamb-Dicke factor, 19
lock-in amplifier, 59
low-pass filter, 32

magnetic field
  fluctuation, 110
  strength, 106, **115**
micromotion, 30, **93**
motional quantum number, 12
  mean, 111, **116**

Nirvana photodiode, 59

objective, 63
  image optimisation, 70
optical bleaching, 9

Paul box
  compiler, 81
  direct digital synthesisers, 78
  jitter, 81
  time resolution, 78
PCP compiler, *see* Paul box compiler
photo-ionisation, **38**, 45
photomultiplier, 66
  interplay, 82
PMT, *see* photomultiplier
  signal-to-background, 66
polarisation drift, 47
pulse programme, 106

quantum fluctuations, 89

Raman beam
  intensity, 107
  intensity fluctuation, 110
Raman Rabi frequency
  orthogonal geometry, 18
  parallel geometry, 17
Red Doppler laser, 13
RF power, 30

saturation intensity, 6
second harmonic generation, 47
secular frequency, 30
shelving, 114
SHG, *see* second harmonic generation
sideband
  micromotion, 95
  second red, 90
  transition, 19, 111
spontaneous emission, 16
squeezed state, 88
Stark shift, 17

TAC, *see* time-to-amplitude converter
teapot curve, 102
temperature
  atomic oven, 38
  CCD camera, 70
  crystal, 47–48
  Doppler cooling, 20
  fibre laser, 46
  ion, 111
  magnetic field coil, 40
time-to-amplitude converter, 83
two-photon stimulated Raman transition, 15

vacuum, 34
virtual Raman level, 15

Zeeman energy shift, 11